ULTRAFAST QUANTUM CONTROL OF EXCITON DYNAMICS IN SEMICONDUCTOR QUANTUM DOTS

by

Angela Gamouras

Submitted in partial fulfillment of the requirements
for the degree of Doctor of Philosophy

at

Dalhousie University
Halifax, Nova Scotia
September 2013

"If you have an opportunity, you must take it!" - M. Senba, 2006

TABLE OF CONTENTS

LIST OF TABLES

LIST OF FIGURES

ABSTRACT

Controlling the quantum states of charge (excitons) or spin-polarized carriers in semiconductor quantum dots (QDs) has been the focus of a considerable research effort in recent years due to the strong promise of using this approach to develop solid state quantum computing hardware. The long-term scalability of this type of quantum computing architecture is enhanced by the use of QDs emitting in the telecom band, which would exploit the established photonic infrastructure. This thesis reports the use of all optical infrared experimental techniques to control exciton dynamics in two different QD samples consisting of InAs/GaAs QDs and InAs/InP QDs within a planar microcavity.

An infrared quantum control apparatus was developed and used to apply optimized shaping masks to ultrafast pulses from an optical parametric oscillator. Pulse shaping protocols designed to execute a two-qubit controlled-rotation operation on an individual semiconductor QD were demonstrated and characterized. The quantum control apparatus was then implemented in simultaneous single qubit rotations using two uncoupled, distant InAs/GaAs QDs. These optimal control experiments demonstrated high fidelity optical manipulation of exciton states in the two QDs using a single broadband laser pulse, representing a step forward on the path to a scalable QD architecture and showcasing the power of pulse shaping techniques for quantum control on solid state qubits.

As an alternative to single QDs, which have very low optical signals, subsets of QDs within an ensemble can be used in quantum computing applications. To investigate the mediation of inhomogeneities in a QD ensemble, pump-probe experiments were performed on InAs/InP QDs within a dielectric Bragg stack microcavity. Two different excitation geometries showed that the angle dependence of the microcavity transmission allowed for the spectral selection of QD subsets with transition energies resonant with the cavity mode. The microcavity mitigated inhomogeneities in the ensemble while providing a basis for addressing QD subsets which could be used as distinguishable quantum bits. This thesis work shows significant advances towards an optical computing architecture using quantum states in semiconductor QDs.

LIST OF ABBREVIATIONS AND SYMBOLS USED

α	Amplitude of Cosine Function
Å	Angstrom (Unit of Length)
A	Transfer Matrix
$A_M(\omega)$	Amplitude Pulse Shaping Mask
A_0	Amplitude Factor
a_{xy}	Elements of Transfer Matrix
AC	Alternating Current
AFM	Atomic Force Microscope
AlGaAs	Aluminum Gallium Arsenide
ARP	Adiabatic Rapid Passage
BBO	Beta Barium Borate
BS	Beam Splitter
C	Conduction Band
CdSe	Cadmium Selenide
c	Speed of Light in Vacuum
c_n	Complex Time-Dependent Coefficient
CCD	Charged Coupled Device
CISC QC	Complex Instruction Set Quantum Computing
C-ROT	Controlled Rotation Operation
CWPL	Continuous Wave Photoluminescence
Δ	Laser Detuning
Δ_0	Spin-Orbit Splitting Energy
ΔT	Pump Induced Change in Transmission
δ	Multiphoton Intrapulse Interference Phase Scan Scanning Parameter
δ_{p}	Phase Accumulation
D	Detector
d	Dielectric Layer Thickness

$\frac{\partial}{\partial t}$	Partial Derivative With Respect to Time
E	Electric Field
$\widetilde{E}$	Fourier Transform of Electric Field
e	Proton Charge
E_c	Conduction Energy Band
E_g	Band Gap Energy
E_n	Energy of State n
ES	Excited State
E_v	Valence Energy Band
eV	Electron Volt (Unit of Energy)
exp	Exponential with Base e≡2.7182818...
ϵ_0	Permittivity of Free Space
$\Phi_M(\omega)$	Phase Pulse Shaping Mask
ϕ	Phase of Ultrafast Pulse
φ	Phase Shift of Cosine Function
F	Fidelity
γ	Spectral Frequency of Cosine Function
GaAs	Gallium Arsenide
GT	Gate Time
$\hbar$	Reduced Plancks Constant
$\hat{H}$	Hamiltonian
HH	Heavy Hole Valence Band
i	Unit Imaginary Number $\equiv \sqrt{-1}$
IFQD	Interface Fluctuation Quantum Dot
InAs	Indium Arsenide
InGaAs	Indium Gallium Arsenide
InP	Indium Phosphide
IR	Infrared
ITO	Indium Tin Oxide
J	Joule (Unit of Energy)
J	Total Angular Momentum
K	Degrees Kelvin (Unit of Temperature)
$\vec{k}$	Wave Vector

ξ	Multiphoton Intrapulse Interference Phase Scan Phase Function
λ	Wavelength of Light
L	Width of Infinite Square Well
l	Thickness of Liquid Crystal Layer
LC	Liquid Crystal
LH	Light Hole Valence Band
ln	Natural Logarithm
M	Mirror
$M(\omega)$	Pulse Shaping Mask Function
m_j	Spin Projection Quantum Number
MIIPS	Multiphoton Intrapulse Interference Phase Scan
$\vec{\mu}$	Electric-dipole Operator
μ_0	Permeability of Free Space
ν	Semiconductor Energy Band Index
n	Principle Quantum Number
n_x	Index of Refraction of Material x
NA	Numerical Aperture
NIR	Near Infrared
$\vec{\Omega}$	Field Vector
Ω	Integration Variable
Ω_R	Complex Rabi Frequency
ω	Frequency of Monochromatic Plane Wave
OPA	Optical Parametric Amplifier
OPO	Optical Parametric Oscillator
OQC	Optimal Quantum Control
π	3.14159...
PC	Polarized Beam Splitter Cube
PL	Photoluminescence
PLE	Photoluminescence Excitation
ψ	Electronic Wavefunction
$\vec{q_i}$	Vector with Components Describing the Pulse Shaping Function
QD	Quantum Dot
QWP	Quarter Wave Plate

$\vec{r}$	Vector Which Describes Spatial Separation of Charge
ρ	Density Matrix
rad	Radians
RISC QC	Reduced Instruction Set Quantum Computing
σ+	Right Circular Polarization
σ-	Left Circular Polarization
$\vec{S}$	Optical Bloch Vector
SAQD	Self-Assembled Quantum Dot
SH	Second Harmonic
Si	Silicon
SiO_2	Silicon Dioxide
SLM	Spatial Light Modulator
SO	Spin-Orbit Split-off Valence Band
STM	Scanning Tunneling Microscope
$\Theta(t)$	Pulse Area
τ	Pulse Duration
T	Transmission of Probe Pulse in the Presence of the Pump Pulse
T_0	Transmission of Probe Pulse in the Absence of the Pump Pulse
t	Time
T_1	Occupation Decay Time
T_2	Coherence Decay Time
Ta_2O_5	Tantalum Pentoxide
TE	Transverse Electric Polarization
TL	Transform-Limited
TM	Transverse Magnetic Polarization
TPA	Two Photon Absorption
Tr	Trace of a Matrix
$u_{\nu\vec{k}}(\vec{r})$	Cell Function Containing Lattice Periodicity
V	Applied Voltage
χ_R	Rabi Frequency
z	Growth Direction
$\updownarrow$	Linear Polarization
*	Denotes Complex Conjugate

ACKNOWLEDGEMENTS

I will always appreciate the diverse range of experience I have gained at Dalhousie University. I am grateful to have had Dr. Kimberley Hall as my supervisor during my graduate studies. Through her guidance, I was given invaluable opportunities including attending numerous international conferences, visiting other research groups, participating in many types of experiments, and most significantly, establishing a new ultrafast laser laboratory. These experiences, along with countless more, have shaped me into the person I am today and will bring me inspiration in the future.

I wish to thank my colleagues in Team Ultrafast, whose membership has changed over the years. Specifically, I would like to acknowledge Reuble (Captain) Mathew who was my consistent go-to labmate, Tristan (T-Bone) de Boer, Sam March, Dan Webber, Mat Britton, and Aaron Maszko.

I would also like to thank the support staff in the Department, who were always able to help me out: Kevin Borgel and John Noddin in the Machine Shop, Barbara Gauvin, Tanya Timmins, Jenn Currie, Krista Cullymore, Anne Murphy and Anne-Marie Jeffery in the Main Office, and Joe, Karen and Steve from Facilities. Additionally, before my return to Physics, Stephen Whitefield and Kazue Semba provided me with another perspective on research within the Faculty of Medicine.

Most of all, I will always be grateful to Kyle who has given me constant support and encouragement throughout my studies.

CHAPTER 1

INTRODUCTION

1.1 Overview

Our world is becoming increasingly dependent on computers for the storage, processing and transfer of information. This ongoing accumulation of data and need for faster processing has motivated the progressive miniaturization of traditional computing hardware components, an approach that has worked very well up to the present. Despite these advances, there are certain computational problems that remain intractable on todays computers because of the way the computational time scales with the size of the problem. For example, the time taken to factor an integer scales exponentially with the number of digits in the integer. The simulation of quantum systems is also very time intensive because the resources required scale exponentially with the number of particles in the system.

Quantum computing emerged as an alternative to the usual approach to the manipulation, transmission and storage of data with the development of quantum algorithms for the factorization of integer numbers into prime factors (developed by Shor [1]) as well as searching an unsorted database (developed by Grover [2]). In such algorithms, the computation time would only scale as a polynomial in the problem size. The traditional storage of information in bits that are in one of two states (0 or 1) is replaced with a quantum bit, often called a qubit, corresponding to a coherent superposition of two quantum states ($|\psi\rangle = c_0 |0\rangle + c_1 |1\rangle$). A qubit is commonly depicted in a Bloch sphere representation, as shown in Fig. 1.1. In this case, $|c_0|^2$ and $|c_1|^2$ are the occupations of the states $|0\rangle$ and $|1\rangle$, respectively. In contrast to a classical bit, the phase of the quantum state is also utilized. This phase arises from the fact that c_0 and c_1 are complex coefficients. The computing resources scale very differently in quantum computing compared to classical computing.

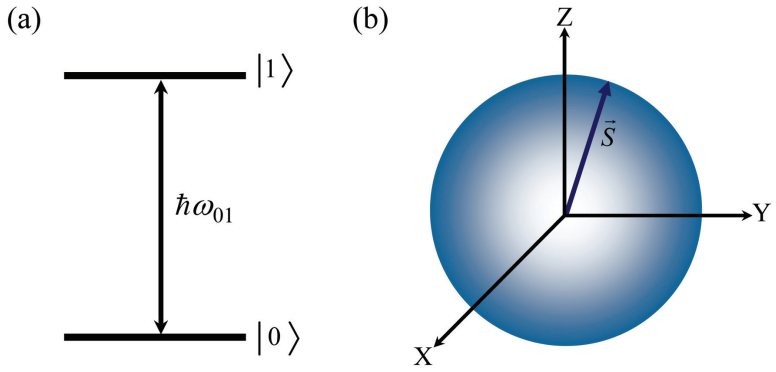

Figure 1.1: (a) Energy level diagram of two-level system with ground state $|0\rangle$ and excited state $|1\rangle$. (b) Bloch sphere representation of occupation and coherence in the two-level system. The components of the Bloch vector $\vec{S}$ are given by $S_x = 2\mathrm{Re}\{c_1 c_0^*\}$, $S_y = -2\mathrm{Im}\{c_1 c_0^*\}$, and $S_z = |c_1|^2 - |c_0|^2$ which describe the real and imaginary components of the ensemble average coherence and state occupation respectively.

One qubit can be in both states $|0\rangle$ and $|1\rangle$ at once, and similarly a system of *n* qubits can be in an arbitrary superposition of all possible 2^n classical states simultaneously.

Quantum computation is carried out by evolving the wavefunction describing the entire system of qubits in time. An implemented algorithm would correspond to a series of gates that may include the controlled modification of the quantum states of individual qubits, called single qubit gates, and the introduction of controlled interactions between qubits that cause their quantum states to be entangled (two-qubit gates). At the end of the computation, a measurement of the state of the system of qubits, which collapses the wavefunction into one of the 2^n states, yields the answer to the problem being solved. The technique used to measure the final quantum state of the system depends on the physical system used to encode the qubits. For example, the simplest instance of Shor's factoring algorithm (factoring 15 into prime factors three and five) was realized using nuclear magnetic resonance techniques, in which seven qubits involved in the computation were represented using the states of various spin-$\frac{1}{2}$ nuclei within a molecule [3]. The solution to the problem in this case was determined by the final spin configuration of the nuclei, which is measured through phase sensitive detection of oscillating voltages in radiofrequency coils placed near the sample. A multiple-input AND gate has also been carried out using six qubits encoded in the rovibrational states of a lithium molecule [4]. In this case, different sets of input values of the qubits were encoded by exciting with a

shaped optical pulse, and the answer was determined by photoionizing the molecule at a particular time delay relative to the encoding pulse, which has the effect of projecting the superposition of possible system states into a single ionic final state. The Deutsh-Jozsa algorithm, corresponding to testing whether a function is balanced or constant, was also experimentally demonstrated using a single qubit encoded in an exciton (*i.e.*, a bound state of an electron-hole pair) in a semiconductor quantum dot [5]. In this case, the final quantum state was measured through the intensity of photoluminescence indicating the presence or absence of an exciton at the end of the calculation.

Since the phase of the qubit is utilized in quantum computing, decoherence processes that randomize the phase are detrimental. Decoherence is caused by either relaxation of the system from $|1\rangle$ to $|0\rangle$ (changing the occupations $|c_0|^2$ and $|c_1|^2$) or by a scattering interaction that only changes the phase of the qubit. For a two-level system such as that shown in Fig. 1.1(a), the time scale associated with the former process is called the T_1 or longitudinal relaxation time. The decay of coherence is characterized by the T_2 time. In quantum computing, all relevant quantum gates must be completed within the T_2 time, including possible error correction routines which require additional gates. This represents one of the challenging constraints in the development of quantum computing systems.

DiVincenzo proposed a set of requirements for the physical implementation of quantum computation [6]. A physical system must be chosen that allows quantum states forming qubits to be identified and characterized. Experimental methods for initializing the qubits must be developed, as well as approaches for reading out the state of each qubit at the end of the computation. As discussed above, decoherence times in the chosen physical system must be longer than the gate operation time. Finally, a *universal* set of quantum gates must be identified. The word universal in this context refers to the fact that this set allows one to construct any other gate and thereby carry out any quantum algorithm using this minimal set of gates. This is analogous to classical computing where a NAND gate, which produces a negative output only if all inputs are positive, is called a universal gate as a combination of NAND gates can be used to implement any boolean function. Satisfying all of DiVincenzo's criteria in a single physical system represents a formidable technical challenge. The investigation of various candidate systems has been the subject of a worldwide research effort spanning more than a decade.

DiVincenzo also showed that a combination of single qubit and controlled NOT (C-NOT)

two-qubit gates, which invert the second qubit only if the control qubit is present, can be used to implement arbitrary unitary operations, creating a set of universal quantum gates [7, 8]. This approach is often referred to as reduced instruction set quantum computing (RISC QC). An alternative approach was suggested by Sanders *et. al.* [9] in which a single unitary matrix that encodes the overall computation replaces series of gates with a single complex instruction. This approach is called complex instruction set quantum computing (CISC QC). For example, such an approach was demonstrated by Amitay *et. al.* [4] in molecular qubit systems. In CISC QC, the requirement of long decoherence times is alleviated by the ability to apply a single complex instruction using a customized pulse shape, instead of a pulse sequence. This benefit comes at the expense of the need to generate complex pulse shapes.

The realization of a universal quantum computer is the central objective of quantum information science, which encompasses the development of quantum algorithms for computation, cryptography, and the development of quantum computing hardware. Several choices of qubits within different quantum computing architectures have been proposed and experimentally realized, including ion traps, superconducting circuits, the rovibrational states or nuclear spin states in molecules, N-V centers in diamond, and semiconductor quantum dots. The electronic states of confined ions act as qubits in trapped ion systems. Superconducting qubits are based on current loops containing Josephson junctions, where the qubit is stored in the quantized flux in these current loops. In nuclear magnetic resonance systems, the spin states of nuclei in molecules act as qubits, or one can use the rovibrational states in molecules detected by selective optically-induced ionization. The spin state of an electron on the N-V^- point defect can be used as a fundamental qubit in diamond. In semiconductor quantum dots, qubits are realized using discrete energy states resulting from quantum confinement. The focus of this thesis work is to further the long-term prospect of a scalable quantum computer based on semiconductor quantum dots.

1.2 Semiconductor Quantum Dots

Semiconductor quantum dots (QDs) are nanoscale structures that exhibit three-dimensional quantum confinement through the introduction of a local potential well with finite barriers. This confinement transforms the energy bands in bulk semiconductors into discrete levels, as illustrated schematically in Fig. 1.2(a). By controlling the QD size or the material

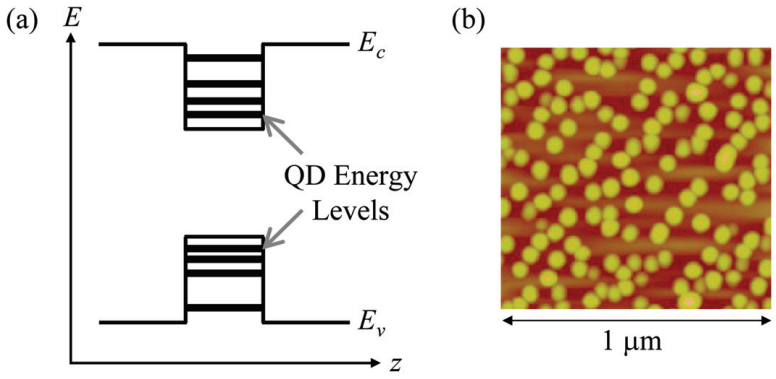

Figure 1.2: (a) Schematic diagram of the discrete energy band structure resulting from three-dimensional quantum confinement, where E_v and E_c are the valence and conduction bands respectively, and z indicates the growth direction of the structure. (b) AFM image of uncapped InAs SAQDs grown on GaAs. Image courtesy of D. G. Deppe.

composition, the spacing between the energetic states can be adjusted. The confinement energy is the energy separation between the lowest conduction level (or highest valence level) and the associated barrier. Due to their discrete density of states, QDs act as artificial atoms. The dipole moment of a QD, which is the matrix element of the dipole operator $-e\vec{r}$ and reflects the strength of coupling to a light field, is much larger than the dipole moment of atoms. These unique features make QDs attractive for a variety of applications including QD lasers [10, 11], all-optical switches [12], and cellular imaging [13]. For example, the discrete energy level structure reduces the threshold current density relative to similar quantum well structures in QD laser applications [10], and the large dipole moment leads to a large optical response in all-optical switching applications [12].

There are several types of semiconductor QDs: (*i*) lateral; (*ii*) colloidal; (*iii*) interface fluctuation; and (*iv*) self-assembled QDs. In lateral QDs, confinement is achieved through electrical gating in patterned two-dimensional electron gas structures. Colloidal QDs are synthesized from the nanocrystal growth of compounds dissolved in solution. Interface fluctuation quantum dots (IFQDs) and self-assembled quantum dots (SAQDs) are both fabricated using epitaxial growth techniques, which involve the deposition of one material onto another bulk material. Epitaxial growth can occur in one of three main growth modes: monolayer growth, the Volmer-Weber growth mode, and the Stranski-Krastanow growth mode [14]. In monolayer growth, the atoms of the deposited material are more strongly attracted to the bulk material substrate than to each other. The deposited atoms form

monolayer high islands which expand and fuse together, forming the first monolayer. This growth mode is used for IFQDs, which consist of randomly-formed monolayer-high islands of a semiconductor material at an interface (*e.g.* GaAs on an AlGaAs interface). Overgrowth with additional AlGaAs leads to random monolayer-high regions that act as QDs. In Volmer-Weber mode, the deposited atoms are more strongly attracted to each other than to the substrate material. The atoms will initially aggregate to form islands and ongoing deposition will result in the formation of a continuous film. SAQDs are fabricated using the Stranski-Krastanow growth mode, in which the self-assembly process exploits the natural lattice mismatch between two semiconductors. The Stranski-Krastanow growth mode starts with the monolayer growth of either a single or small number of monolayers of deposited atoms forming a thin film. As deposition continues, strain build-up leads to spontaneous reorganization into three-dimensional islands. Since this self-assembly process is strain driven, the number of monolayers that can be deposited before the strain in the system induces break-up of the layer into islands depends on the material system considered. For InAs QDs in GaAs, island formation occurs after about three monolayers. An atomic force microscope (AFM) image of self-assembled InAs QDs is shown in Fig. 1.2(b). The yellow areas are the islands of InAs on top of a monolayer flat surface of GaAs. More GaAs is grown on top of the InAs islands, leading to three-dimensionally confined QDs. The lateral dimensions of SAQDs are $\sim$5 times smaller than IFQDs which can be $\sim$100 nm in diameter [15]. This size difference leads to a $\sim$5 times larger optical dipole moment for IFQDs [16]. However, the development of a scalable architecture for quantum computing is a challenge for IFQDs due to the random nature of their formation. In contrast, advanced epitaxial growth techniques may be used to grow patterned arrays of SAQDs [17].

The many advantages of semiconductor QDs (discrete energy states, large dipole moments, and ease of fabrication) come with the challenges associated with understanding and mitigating decoherence and determining how to control fundamental quantum states in the complex solid state environment (considering phonons, defects, many body effects, *etc*.). For these reasons, implementations of qubits in other systems such as ion traps and superconducting circuits are presently more advanced than qubit systems in semiconductor QDs. Nonetheless, QDs offer the promise of long-term scalability through exploitation of state-of-the-art semiconductor fabrication and processing. Together with progress in

the integration of III-V semiconductors with Si-based systems [18], this also suggests the feasibility of integration of a QD based quantum computing platform with existing computing technology. Such integration would be much more challenging in non-solid state qubit realizations such as in ion traps and molecular qubit systems. As a result, advances in the implementation of QDs as a quantum computing platform are of relevant interest.

1.3 Qubit Encoding and Control in Quantum Dots

Various schemes for the implementation of elementary single- and two-qubit quantum gates using semiconductor quantum dots have been proposed [19, 20, 21, 22, 23, 24, 25, 26]. The choice of a two-level quantum system to use as the fundamental qubit varies from proposal to proposal. For example, the presence or absence of an exciton [21, 22, 23] or the spin-up and spin-down states of a single electron [19, 20, 24, 25, 26] have been put forward as candidate physical qubits (*i.e.*, the $|0\rangle$ and $|1\rangle$ states in Fig. 1.1). In addition, the combination of both exciton and spin qubits could be utilized, where exciton states could be implemented for computation and spins for the storage of information [27]. Single-qubit gates correspond to an arbitrary manipulation (both occupation and phase) of the quantum state of a single qubit, and two-qubit gates involve the generation of controlled entanglement between two quantum bits. The methods of control used to carry out these operations vary considerably from one proposed quantum computing scheme to another.

There are several approaches that involve the optical control of qubit states in SAQDs [20, 21, 22, 23, 24, 25, 26]. A few schemes in which exciton qubits are utilized are shown in Fig. 1.3(a) and (b). Single qubit gates involving excitons may be carried out using a resonant Rabi rotation (which changes the state occupations) and the AC Stark effect (which changes the phase of the qubit). In the former case, a coherent optical field resonant with the exciton transition leads to oscillations of the state occupations in time, a process that is described in more detail in Sec. 2.3. The final quantum state is determined by the total area of the laser pulse, defined as $\Theta(t) = \int_0^t dt' \, \mu \frac{E_0(t')}{\hbar}$ where μ is the dipole moment, and $E_0(t)$ is the time-dependent electric field of the laser pulse. The notation Θ used for the pulse area captures the motion of the Bloch vector during a Rabi oscillation; it is the total angle (in radians) that the Bloch vector rotates about the X axis (see Fig. 1.1) as a result of coherent driving by the optical pulse. For example, a pulse that rotates the

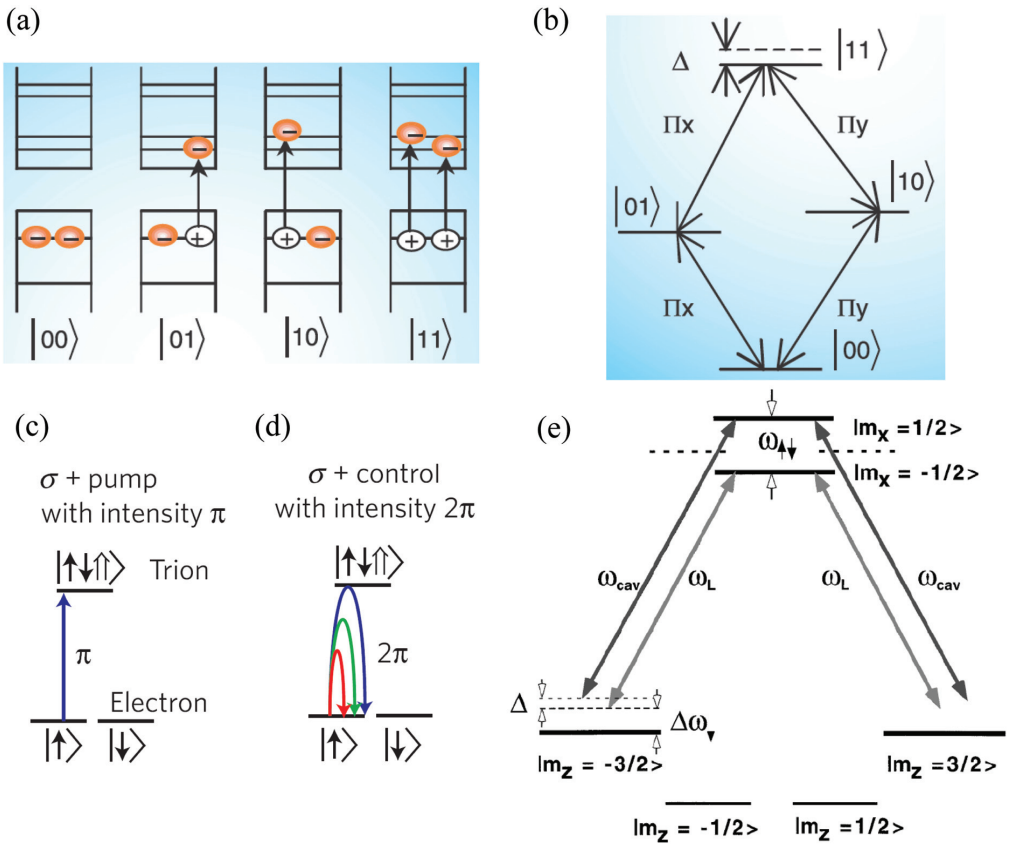

Figure 1.3: Examples of qubit states in semiconductor quantum dots: (a) Two-qubit excitonic transitions in an individual QD. Adapted from Ref. [28]. (b) C-ROT energy level diagram, where $|00\rangle$, $|01\rangle$, $|10\rangle$ and $|11\rangle$ are the ground state, oppositely polarized exciton states, and the biexciton respectively. The biexciton binding energy is given by Δ. Adapted from Ref. [28]. (c) π-pulse excitation populating trion spin state. Adapted from Ref. [29]. (d) A 2π-pulse in this level scheme does not change the state occupation, but results in a rotation of electron spin [29]. (e) Electron qubit level scheme indicating transitions between valence-band states $|\mathrm{m}_z = \pm 3/2\rangle$ and conduction band states $|\mathrm{m}_x = \pm 1/2\rangle$ in the presence of a magnetic field [20].

Bloch vector by π radians is called a π-pulse. The optical Stark effect corresponds to a similar coherent interaction, except that the center frequency of the pulse is detuned from resonance (*i.e.*, the center frequency of the laser pulse ω is not equal to ω_{01} in Fig. 1.1(a)). The resulting dynamics may be understood in terms of a transient shift of the transition energy of the exciton that results in an accumulated phase of the exciton qubit. This phase depends sensitively on the size of the detuning and the pulse area.

Another method used to control an exciton qubit is adiabatic rapid passage (ARP), and

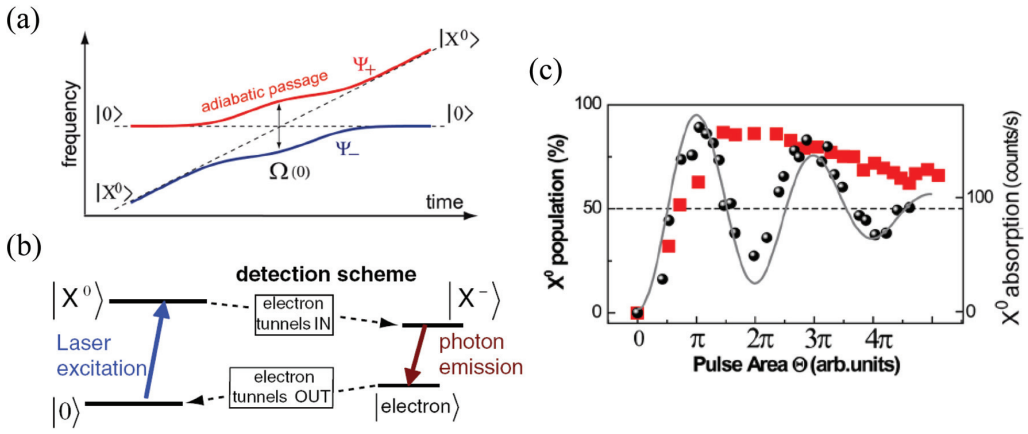

Figure 1.4: (a) Dressed state representation of population transfer between the ground state and X^0. (b) Energy level diagram showing neutral exciton (X^0) excitation and negatively charged exciton emission (X^-). (c) Measured (circles) and modeled (solid curve) Rabi oscillations using TL pulse excitation. Squares denote population of X^0 with strongly chirped pulse excitation. Adapted from Ref. [30].

is illustrated in Fig. 1.4(a). In ARP, the optical control pulse is characterized by a time-dependent instantaneous frequency, called chirp, which is used to control the population transfer between the two quantum states representing the qubit. Such a chirped control pulse is distinct from the usual case of a pulse with a constant frequency and phase, called a transform-limited (TL) pulse. (In Fig. 1.4, $|0\rangle$ and $|1\rangle$ are represented as $|0\rangle$ and $|X^0\rangle$, reflecting the exciton.) The time-dependent frequency leads to a slow evolution of the ground state of the system taking the light field into account. The population transfer results from the evolution of the two quantum states through an anti-crossing, where the frequency of the control pulse is swept through the transition resonance. In a Bloch sphere representation, the Bloch vector adiabatically follows the torque vector associated with the laser field and stays in the upper state when the pulse over. Unlike Rabi rotations, ARP is robust against system variations (*e.g.*, laser power); however, the magnitude of linear chirp required for qubit control can result in longer (∼picosecond) optical pulses, extending the operation time.

An example of an exciton based two-qubit gate is the controlled-rotation gate, or C-ROT gate involving excitons in the same QD, and is presented in Fig. 1.3(a) and (b). This scheme was first proposed by Troiani *et. al.* [21]. The two-exciton basis states are depicted in Fig. 1.3(a), and consist of the presence or absence of excitons with opposite spin

orientations. The spin state of an exciton is determined by the spin states of the constituent electron and hole. The associated optical transition is described by selection rules, as discussed further in Sec. 2.2, through which the polarization of the light field can be used to select the spin of the optically injected exciton. In Fig. 1.3(a), $|00\rangle$ is the vacuum ground state (no exciton), $|01\rangle$ and $|10\rangle$ correspond to the occupation of one of each of the two oppositely spin polarized exciton states, and $|11\rangle$ is the bound biexciton state. Figure 1.3(b) depicts the level scheme for this system. The C-ROT operation implements a π rotation on the second qubit if and only if the control qubit is present. It can be achieved in this system by exploiting the optical selection rules, together with spectral selection afforded by the non-zero biexciton binding energy (Δ in Fig. 1.3(b)). In particular, a Π_x polarized laser pulse resonant with the $|00\rangle$ to $|01\rangle$ transition would be off-resonant with the $|01\rangle$ to $|11\rangle$ transition by an amount equal to Δ as the resonant energy from the exciton-to-biexciton transition is lower than that required to take the system from the ground state to one of the single exciton transitions. For example, Li *et. al.* [28] used a two-colour excitation scheme to demonstrate a C-ROT gate. A pre-pulse tuned to an exciton transition (*e.g.* the $|00\rangle$ to $|01\rangle$ transition) prepared the control qubit to be present for this conditional gate. A second laser pulse, tuned to the exciton-to-biexciton transition, was used to manipulate the state of the second qubit.

Loss and DiVincenzo [19] were the first to devise a computational architecture using the spin state of a single electron in a negatively charged quantum dot as the fundamental qubit. In this approach, single qubit gates are carried out through controlled evolution of the spin state of each QD in an external magnetic field, and two-qubit gates are achieved through electrical gating of a tunneling barrier between two adjacent lateral QDs. The disadvantage of lateral gate patterned QDs is that spin control is relatively slow ($\geq$ ns). It is possible to control spin qubits optically on much shorter time scales in SAQDs. Schemes for optically-mediated single qubit gates involving electron spin are shown in Fig. 1.3(c) and (d). In this case, the relevant optical transition connects a single electron spin state to a spin-polarized charged exciton state, called a trion (represented by $|\uparrow\downarrow\Uparrow\rangle$ in Fig. 1.3(c)). The transitions between the single electron spin states and the trion states are subject to optical selection rules, as in the case of exciton transitions in neutral QDs. Spin initialization and control in this system is carried out using stimulated Raman transitions, in which the spin-up and spin-down states of the electron with respect to an external

magnetic field and the trion state form a three-level Λ system, and the electron spin states are coupled using circularly polarized light. Excitation of this transition with a π-pulse can be used for spin initialization, while a 2π pulse can be used to change the phase of the qubit. In the later case, the phase change is proportional to the dipole moment and laser detuning from the optical transition. A similar stimulated Raman transition can also be used to realize a two-qubit gate involving spins in different QDs when this transition is assisted by an optical microcavity mode, as depicted in Fig. 1.3(e). An optical microcavity is a micron-scale structure used to confine light. The modes of the microcavity describe the allowed standing waves that can exist in such a structure.

The possibility of exploiting optical microcavities as a means of tailoring the light-matter interaction for a QD inside of the cavity is another advantage of implementing SAQDs as a quantum computing architecture. There are several types of optical microcavities distinguished by the approach used to confine light (*e.g.* planar mirrors, photonic bandgap structures, *etc.*), and the dimensionality (1D, 2D or 3D). A one-dimensional microcavity is formed using two mirrors. These mirrors are typically realized using alternating high- and low-refractive index layers, forming what is called a Bragg stack. In this case, the QDs would be contained in a spacer layer between the mirrors [31]. Coupling of the QD with the dominant Fabry-Pérot cavity mode can be used to enhance the probability of spontaneous emission into the growth direction of the Bragg stack and QD structure, where spontaneous emission corresponds to the decay of the exciton to the ground state with the emission of a photon [32]. In this case, the enhanced spontaneous emission rate results from the larger optical density of states corresponding to emission in the vertical direction [33]. A two-dimensional microcavity can be formed by etching a periodic array of nanoscale holes in a semiconductor wafer. This periodic structure forms an effective mirror at light frequencies within the so-called photonic bandgap. In this case, the QDs would be located where one or more holes is missing, as such a location represents a cavity [34]. A whispering gallery mode microcavity [35] is another example of a 2D microcavity, in which a two-dimensional structure is etched into a pillar shape, resulting in circularly orbiting confined modes. A 3D optical microcavity can be realized by incorporating a Bragg stack 1D cavity with either of the above two approaches for introducing in-plane optical confinement. Microcavities play a central role in several quantum computing proposals involving the optical control of charge or spin qubits in SAQDs [20, 26]. The rapidly advancing progress in the fabrication

of microcavities, which now allows a single QD to be placed in a well-defined spatial location relative to the peak of the light intensity within the microcavity mode [34], will further the long-term goal of realizing these proposals. The ability to exploit established photonic and telecommunication infrastructure further enhances the prospect of scaling such an architecture to a large number of qubits.

Among quantum computing proposals, schemes for controlling the qubit state using femtosecond optical pulses are favorable as the quantum operations can take place on the time scale of the optical pulse. Decoherence in quantum computation is detrimental as it destroys the phase of the qubit and therefore destroys the stored information. A typical requirement for quantum error corrections schemes, proposed by Preskill [36], is that the decoherence time must be at least 10^4 times greater than the operation time. This condition makes long decoherence times especially attractive since sufficient time is required to operate on the qubit as well as impose fault tolerant quantum error correction. It also points to the need for developing fast approaches to manipulating the qubit state. Decoherence times (T_2) for exciton states of approximately a nanosecond have been reported [37]. The spin state of a single electron in a semiconductor QD has an even longer decoherence time, in the range of milliseconds [38]. Incorporating femtosecond optical control schemes would permit the use of either exciton or spin states as the fundamental qubit in a fault-tolerant computational platform due to the high speed of the elementary gates.

1.4 Experimental Approaches for Characterization and Optical Control

In order to carry out optically-mediated fundamental quantum gates in QDs, one needs to first characterize the QD electronic structure. The energies of the optical transitions (*e.g.* ground state transition and first excited state transition) are determined using continuous-wave photoluminescence (CWPL). This type of experiment involves the use of continuous-wave laser excitation to optically inject electron-hole pairs into the barrier semiconductor layer surrounding the QDs. These injected carriers will relax into the discrete QD energy states before recombining and emitting photons with frequencies associated with the allowed optical transitions. An energy level diagram of a CWPL experiment is illustrated in Fig. 1.5(a).

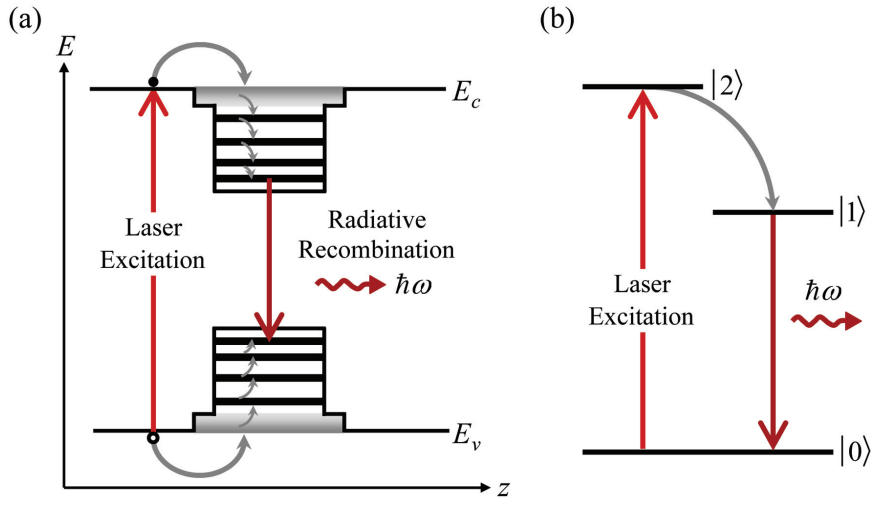

Figure 1.5: (a) Single electron energy-level diagram depicting a CWPL experiment. Injected carriers (*i.e.*, electron-hole pairs) radiatively relax and emit photons from the QD energy states. The downward arrow indicates emission on the ground state optical transition. (b) Example PLE energy diagram, shown in a two-particle picture, in which $|1\rangle$ and $|2\rangle$ are excitons excited on the ground and first excited state transitions, respectively. Laser excitation populates state $|2\rangle$ which decays non-radiatively to state $|1\rangle$. The radiative PL emission from state $|1\rangle$ is detected.

A combination of CWPL and photoluminescence excitation (PLE) spectroscopy can be used to investigate the electronic states of SAQDs in greater detail. PLE measurements also utilize the radiative recombination of carriers; however, in this case, the laser is used to excite electron-hole pairs directly into the excited state transitions within the QDs. The excitation laser is tuned throughout a range of energies while detecting the PL from the ground state transition. In this way, the energy separation between the ground state and excited state optical transitions can be determined. A sample PLE energy-level diagram is shown in Fig. 1.5(b). The results of these electronic structure characterization measurements can then be incorporated into the design of optical control experiments.

There are several experimental approaches to demonstrating ultrafast optical manipulation of fundamental qubits in QDs [39, 40, 41]. Quantum state read-out can be monitored using time-averaged PL measurements. In this type of experiment, a control pulse is used to excite the chosen quantum state transition. The state occupation is then observed by the PL emission. The detected PL signal results from excitation by a number of optical pulses, dictated by the repetition rate of the excitation laser, and so this is a time-averaged technique. Time-resolved pump-probe experiments can also be used to implement optical

control schemes on spin and exciton based qubits. In a pump-probe experiment, one excites the sample using an intense pump pulse and measures the change in the optical properties of the system detected by a weaker probe pulse at some later time. The probe pulse can be used to investigate a variety of dynamics depending on the property of the probe pulse that is measured. For example, the change in the probe transmission indicates a change in absorption, referred to as a bleaching signal. Such a signal can be used to detect the occupation of the upper level of the qubit. In addition, spin-dependent measurements are performed by monitoring the change in the linear polarization of the probe pulse, which exploits the optical selection rules of the QDs. These optical selection rules are described in more detail in Sec. 2.2.

1.5 Experimental Demonstrations of Optical Control: Previous Work

This section contains a review of the relevant body of literature for this thesis. This review includes an overview of quantum control experiments involving individual and ensembles of semiconductor quantum dots. The literature relevant for coherent control in single QDs (Sec. 1.5.1) sets the stage for the projects described in Chapters 4 and 5. The previous work on optical control in QD ensembles (Sec. 1.5.2) provides appropriate context for the experiments described in Chapter 6.

1.5.1 Coherent Control in Single Quantum Dots

1.5.1.1 Rabi Rotations of Excitons Qubits

The first demonstrations of coherent control of fundamental electronic excitations in single semiconductor QDs involved Rabi rotations of exciton qubits [42, 43, 44, 45, 46, 47]. As discussed in Sec. 1.3, a Rabi rotation corresponds to the rotation of the Bloch vector describing an exciton induced by excitation using a coherent optical pulse resonant with the associated optical transition. This was first demonstrated by Stievater *et. al.* [42] in IFQDs using differential transmission techniques, in which the pump-induced change in the transmission of the probe pulse is detected. The signal in such an experiment indicates the instantaneous occupation of the exciton. In the experiments of Stievater *et. al.*, the near-infrared transition energy of the QDs permitted the use of Si-based detectors, which have low dark current compared to InGaAs detectors operating in the infrared.

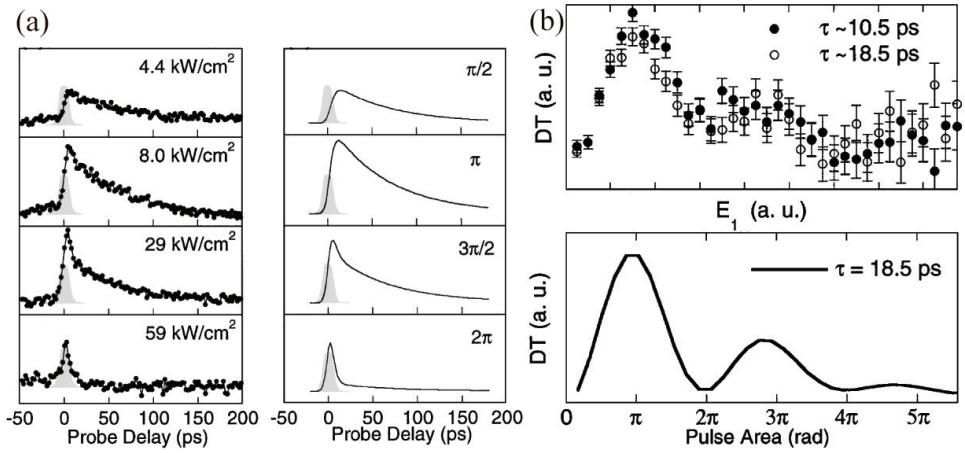

Figure 1.6: Differential transmission data collected by Stievater *et al.* demonstrating Rabi oscillations in a single quantum dot. (a) Measured and calculated differential transmission signals for various pump powers and pulse areas. (b) Differential transmission data versus pump power with associated calculated pump-probe signal versus pulse area at a fixed delay. Adapted from Ref. [42].

Together with the relatively large dipole moment of an IFQD, this enabled the differential transmission signal from an individual QD to be large enough to be detected. The results of these experiments are shown in Fig. 1.6. The pump and probe pulses were tuned to the ground state optical transition in these experiments. Changing the pump pulse area resulted in variation in the magnitude of the differential transmission signal. The strongest signal was detected when pulses that correspond to an area of π radians were used. The authors were able to observe a full 2π Rabi rotation (Fig. 1.6(b)).

Rabi rotations have also been achieved in In(Ga)As SAQDs [43, 45, 46, 47]. The weaker dipole moment in SAQDs compared to IFQDs required an alternative approach to the resonant non-linear spectroscopy technique used by Stievater *et. al.* for quantum state read-out. Kamada *et. al.* [43] and later Htoon *et. al.* [45] demonstrated that one can detect the steady-state PL from the ground state optical transition (often called the s-shell transition) while carrying out coherent optical control on the first excited state transition (often called the p-shell transition). This approach allows one to spectrally reject the strong scattered laser light from the control pulse, permitting the weak PL emission from the ground state of a single QD to be detected. This approach also exploits the rapid decay of the carriers in the excited QD energy levels to the ground energy levels, which occurs on the timescale of a few picoseconds and conserves the carrier spin [48]. Wang *et. al.* [47]

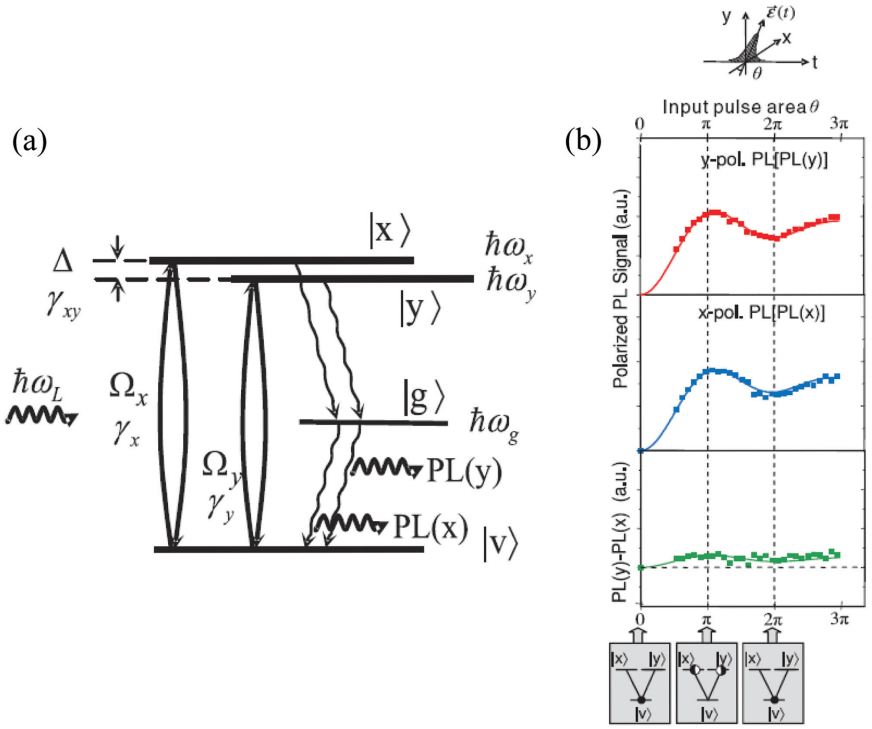

Figure 1.7: (a) Energy level diagram indicating the optical control scheme used by Wang *et al.* [46], involving excitation of the first excited state transition and detection of PL from the ground state transition. (b) Results of Rabi rotation experiments by Wang *et al.* on oppositely polarized exciton transitions in a singe InGaAs QD. Adapted from Ref. [46].

later showed that the optical selection rules can be exploited to achieve tailored excitation of oppositely-spin-polarized excitons with appropriate choice of polarization of the control laser pulse (Fig. 1.7). In these experiments, the single QD PL was collected using a high resolution monochromator and two-dimensional Si CCD array detector, capable of imaging the location of individual QDs. In all of the above experiments, the QDs were subject to tailored growth conditions and/or post-growth processing (*e.g.* annealing) to ensure that the first excited state transition was within the tuning range of a standard Ti:Sapphire laser system (corresponding to near-infrared (NIR) wavelengths) and the ground state PL emission was in the range of highly efficient Si detectors, greatly aiding in the successful execution of these difficult experiments. These experiments were also carried out using relatively long ($\sim$ several ps) optical control pulses.

Another approach was taken by Zrenner *et. al.* [44], who realized single qubit rotations in an individual InGaAs/GaAs QD using a photocurrent detection scheme, as illustrated in

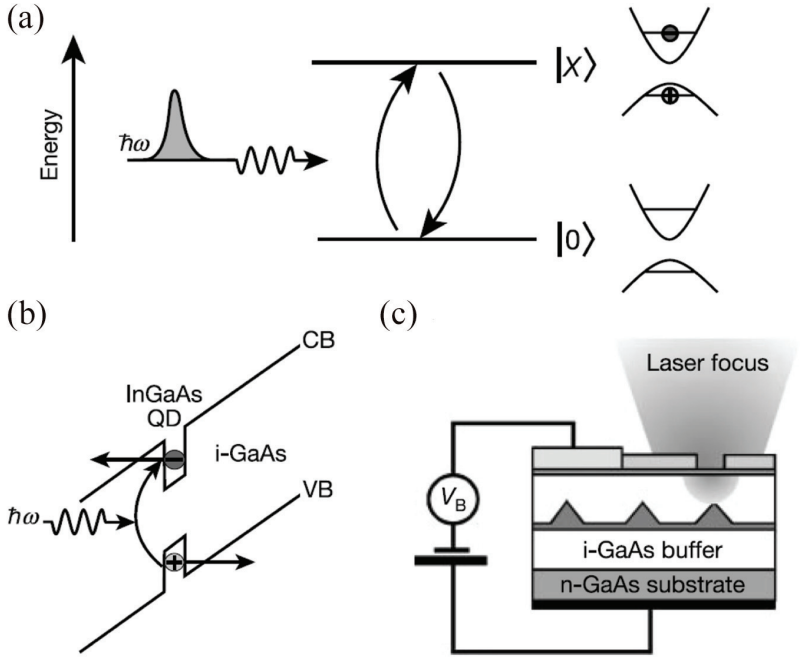

Figure 1.8: (a) Exciton level scheme used by Zrenner *et. al.* (b) Optically generated electron-hole pair within the intrinsic region of the photodiode structure. Tunneling of the electron and hole from the dot results in the change of the photocurrent signal. (c) Sketch of QDs embedded within GaAs n-i-Schotty diode structure with optical excitation restricted to a single QD. Adapted from Ref. [44].

Fig. 1.8. A layer of QDs was embedded within the intrinsic region of a GaAs n-i-Schottky diode structure (Fig. 1.8(c)). The applied laser excitation was resonant with the ground state optical transition in a single QD, which was selectively excited by depositing a shadow mask of apertures (100-500 nm diameter) on the sample surface. The Schottky diode structure was used to apply a bias along the growth direction, creating an internal electric field. This electric field causes the excited exciton to dissociate into its constituent electron and hole, which are then detected as photocurrent. This non-optical detection scheme eliminates the challenge associated with detecting the low optical response of a single QD, but relies on a fast carrier tunneling time for quantum state read-out, which must be shorter than the radiative lifetime (*i.e.*, recombination time T_1) within the QD. This reduces the coherence decay time for exciton qubits, which is a drawback of this approach. Along with all of the other experiments described in this section, the QD structure was tailored to allow optical control to be carried out using a standard Ti:Sapphire laser system producing relatively long ($\sim$ several ps) NIR optical control pulses.

1.5.1.2 Other Quantum Gates Involving Exciton Qubits

Rabi oscillations have also been carried out on the optical transition from the ground state to the biexciton using a coherent two-photon process involving CdSe SAQDs [49] and in InGaAs SAQDs [50]. By tuning the excitation laser to half of the biexciton creation energy, two-photon absorption is induced on the biexciton transition, resulting in controlled Rabi oscillations similar to the above experiments on excitons. Li *et al.* [28] also demonstrated a C-ROT gate using the scheme described in Sec. 1.3 on optical transitions within a single GaAs/AlGaAs IFQD. These experiments were carried out using 5 ps long pulses from a Ti:Sapphire laser system using a similar experimental technique as in Ref. [42]. The gate fidelity, which characterizes the quality of the quantum gate, achieved in these experiments was 0.7, which was limited by the long optical pulses used, together with the short exciton coherence decay time in IFQDs. The fidelity is defined as $F = \mathrm{Tr}[\rho_{\mathrm{ph}}\rho_{\mathrm{id}}]$ where ρ_{ph} and ρ_{id} are the physical (*i.e.*, actual) and ideal density matrices at the end of the laser pulse. As described in Sec. 2.3, the density matrix at a given time *t* describes the ensemble average quantum state, including information about the occupations of the levels involved as well as the presence (or absence) of coherence between these levels. The fidelity describes the performance of the unitary transformation induced by the laser pulse (*i.e.*, the extent to which the transformation brings the state of the system to the intended one). The authors of Ref. [28] pointed to the possibility of using shorter control pulses subject to pulse shaping in experiments on InGaAs SAQDs, which have longer coherence times than IFQDs due to the larger confinement energies, as a direction for improving the fidelity.

Demonstrations of quantum gates based on adiabatic passage [30, 51], where the population transfer between two states is controllable by the second order phase of the optical pulse (*i.e.*, linear chirp), also emphasizes the potential for applications of pulse shaping techniques in quantum computing applications. As described in Sec. 1.3, the coherent control of excitons via adiabatic passage results from the evolution of the quantum state through an anti-crossing arising from chirped pulse excitation (Fig. 1.4(a)). ARP was only very recently demonstrated experimentally by Simon *et al.* [30] and Wu *et al.* [51]. In both cases, optical control was carried out on the ground state optical transition using a Ti:Sapphire laser source and a standard grating stretcher was used to introduce chirp. Unlike a spatial light modulator (SLM) based pulse shaper such as the one used in this thesis work (described in Chapters 2 and 3), which permits the application of an

arbitrary phase profile, a grating stretcher can only be used to apply a linear chirp. The chirped optical control pulses in both the experiments of Wu and Simon were also quite long (15 ps and 40 ps, respectively). A sample of the experimental results of Simon *et al.* are shown in Fig. 1.4(c). In these experiments, a Schotty diode structure was used that allowed for controllable charging of an exciton in a QD through tunneling of excess carriers from a back gate. By optically exciting the X^0 state and detecting the emitted photons from X^-, experimental complications arising from resonant optical excitation, such as scattered laser light, were avoided. Figure 1.4(c) shows the population of the X^0 state using optical pulses of increasing pulse areas. Rabi oscillations are clearly shown in the case of TL pulse excitation, while the chirped pulse excitation shows no oscillation of the populated X^0 state.

1.5.1.3 Optical Control of Spin Qubits

Ultrafast optical control experiments have been carried out on qubits encoded in the spin state of a single electron in a charged QD [40, 52, 53, 54, 55]. For exciton qubits, no initialization is necessary since an exciton always starts off in the vacuum ground state. In contrast, for spin qubits, an extra initialization step is required in order to ensure that an electron spin state is well-defined prior to optical control. Spin initialization has been demonstrated for electron spins [53] and makes use of a weak relaxation of the usual optical selection rules associated with the single electron to trion transitions due to mixing between the heavy-hole and light-hole valence states. Continuous driving of one spin-polarized trion transition leads to a shelving of the spin of the excess electron in the opposite spin state. Partial spin initialization has also been achieved by pumping spin-polarized carriers into the bulk semiconductor barrier layer surrounding the QDs followed by capture of a single spin polarized electron in the QD [40]. This latter approach has a low fidelity because the statistical capture process only happens for a small fraction of the excitation pulses in the pulse train from the laser, but may still be used for demonstrations of optical control. Ultrafast optical manipulation of initialized electron spins has been demonstrated by several groups [40, 54, 55]. As described in Sec. 1.3, optical control is carried out by pumping the trion transition (single electron to positively charged exciton) using circularly-polarized light, which induces a stimulated Raman transition. Using off-resonant pulses, this approach was used by Berezovsky *et al.* [40] and Press *et al.* [54] to perform Rabi rotations of the spin state of a single electron. Kim *et al.* [55] also showed that pure phase

rotations are possible by using a 2π rotation on the trion transition, where the amount of phase shift is determined by the detuning between the laser pulse and the trion transition. The focus of the single QD control experiments in this thesis work is on exciton qubits.

1.5.2 Coherent Control Experiments in Quantum Dot Ensembles

Ensembles of QDs in optical quantum control experiments have the advantage of increased optical coupling, in comparison to single QDs, allowing for ease of quantum state read-out from the system. The optical control of quantum coherence within QD ensembles has been demonstrated using exciton [56, 57, 58] and electron spin states [29, 59, 60, 61, 62]. The challenge associated with implementing ensembles of QDs in control experiments is that the fluctuations in QD size, tied to self-assembled growth, lead to inhomogeneities in transition energies, dipole moments, and g-factors throughout the ensemble. As described in the sections below, these inhomogeneities reduce the fidelity of optical control.

1.5.2.1 Rabi Rotations of Excitons in Quantum Dot Ensembles

Borri *et al.* [57] measured Rabi oscillations of the ground-state-to-exciton transition in an ensemble of InGaAs SAQDs at low temperature using differential transmission pump-probe experiments (Fig. 1.9(a)). In these experiments, the sample contained three layers of QDs within a waveguide structure, characterized by a 60 meV full width at half maximum inhomogeneous broadening of excitonic ground-state transition energies. The Rabi oscillations were found to be strongly damped, with only a few cycles of oscillation observable, as seen in Fig. 1.9(a). Borri *et al.* carried out experiments under various conditions (*e.g.* laser detuning, excitation pulse width, *etc.*) in order to investigate the cause of the observed oscillation damping. Together with a detailed comparison with theoretical calculations, these experiments indicated that the oscillation damping was caused by a distribution ($\approx 20\%$) of transition dipole moments within the ensemble. This inhomogeneity in the dipole moments would therefore limit the fidelity of exciton qubit control in ensembles of QDs.

1.5.2.2 Optical Control of Spin in Quantum Dot Ensembles

Optical control of electron spin qubits has also been achieved in ensembles of semiconductor QDs [29, 61]. As in the case of control of spin in single QDs, these experiments exploited the fact that the QD energy structure in an applied magnetic field is a three-level

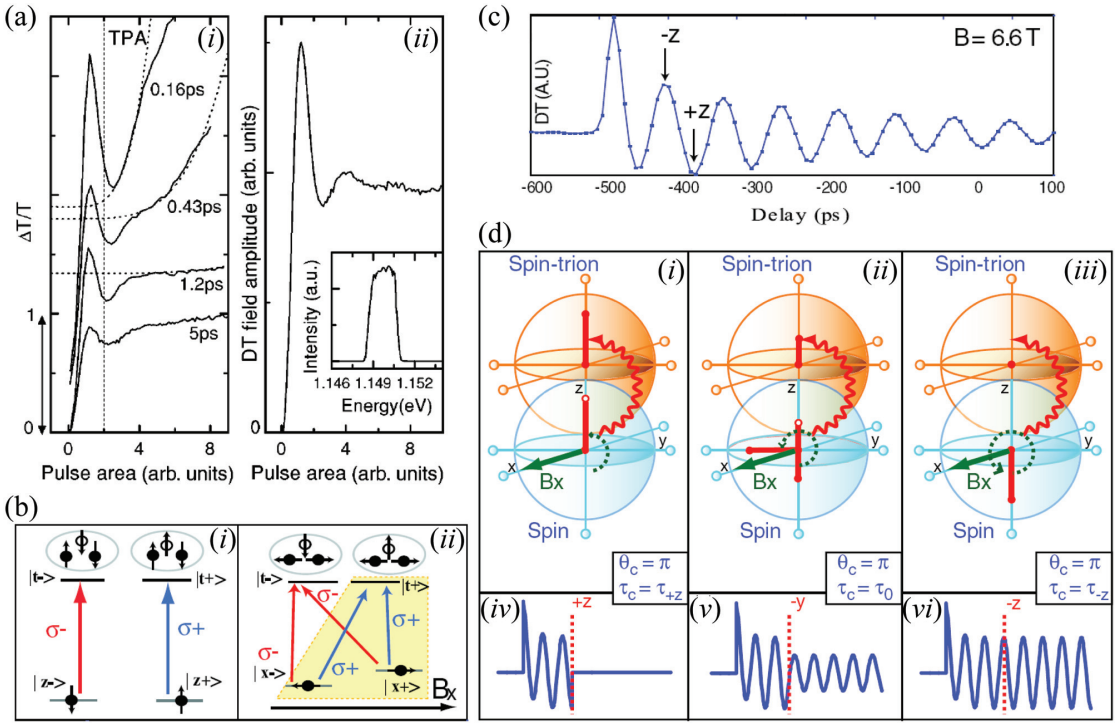

Figure 1.9: (a) (*i*) Graph of time-integrated differential transmission probe intensity for various excitation pulse durations. The dotted lines indicate two-photon absorption in the waveguide sample structure. (*ii*) Measured Rabi oscillation with narrowed pulse spectrum (inset). Adapted from Ref. [57]. (b) Level diagram of charged QDs (*i*) without an applied magnetic field and (*ii*) in magnetic field $B=B_x$. Adapted from Ref. [61]. (c) Quantum oscillation signal of the initialized spin polarization. Adapted from Ref. [61]. (d) (*i*, *ii*, *iii*), Bloch sphere representations of spin dynamics, where the upper sphere represents the trion-spin and the lower represents the initialized spin polarization. (*iv*, *v*, *vi*) Simulated quantum beats in the optical control scheme used by Wu *et al.* Adapted from Ref. [61].

system controlled through stimulated Raman transitions driven through the trion state. The experiments of Wu *et al.* [61] are depicted in Fig. 1.9(b), (c), and (d) and were carried out on GaAs/AlGaAs IFQDs using pump-probe differential transmission experiments. The pump pulse was used to initialize the spin state of the QDs and the probe pulse facilitated quantum state read-out. The pump-probe signal in this case yields quantum beat oscillations in the time-resolved signal, shown in Fig. 1.9(c). By applying a π-pulse at specific delay times relative to the pump pulse, the initialized spin population was rotated. Figure 1.9(d) (*i*, *ii*, *iii*) illustrates the spin population dynamics using the Bloch sphere representation for three cases of control pulse delay and Fig. 1.9(d) (*iv*, *v*, *vi*) are the associated simulated quantum beats. A full 2π rotation of the spin vector, as required for a

spin phase gate, was achieved later by Greilich *et al.* [29] in InAs SAQDs.

In both of the above experiments, the fidelity of optical control was fairly low due to the inhomogeneity of the transition energy and dipole moment of the trion transition across the QD ensemble. In these experiments, periodic optical excitation was used to mitigate inhomogeneity in the g-factor for different QDs by restricting the optical detection signal to spins with a procession period that is an integer multiple of the laser repetition rate, referred to as spin mode-locking. Nevertheless, high fidelity control of the full ensemble requires a precise value of the pulse area and detuning for every QD, a condition that is not achievable due to inhomogeneity in the dipole moments and transition energies.

1.6 Outline of the Thesis

All of the optical control experiments highlighted in the preceding section have utilized optical pulses with a duration of several picoseconds or longer. This restriction was introduced in order to avoid unintentional dynamics associated with nearby energetic transitions. These experiments have also been limited to QDs that have optical transition energies in the wavelength range of conventional Si detectors. Achieving optical control in QDs with emission in the telecom band, despite the increased technical challenges, is an important requirement for long-term scalability as it would enable the existing telecommunications infrastructure to be exploited. The main wavelengths used in optical fiber communications are 1.3 μm and 1.5 μm due to weak dispersive broadening and low power losses in silica fibers. Optical control in QDs with transition energies in these ranges would take advantage of the current photonics framework, utilizing existing fiber optic components which operate efficiently at these wavelengths. In addition, with the exception of recent demonstrations of ARP, existing optical control experiments in single QDs have all been carried out using TL optical pulses, which have a constant frequency and phase, as discussed above. The use of shorter optical pulses (on the order of 100 fs) would allow us to move beyond the simple chirp used in ARP experiments and explore the power and flexibility of general pulse engineering for optimizing the performance of optically-mediated quantum gates. This general approach is referred to as *optimal quantum control*, and has been applied to optimizing quantum gates in atomic and molecular systems [4, 63, 64]. Femtosecond pulse shaping techniques have also found widespread use in more general quantum control processes, including the coherent control of atomic and

molecular systems [65, 66, 67, 68, 69], chemical reactions [70, 71] and non-linear optics [72, 73, 74]. The application of these techniques in systems of single solid state qubits would be an important step forward for the prospect of developing solid state quantum computing hardware.

Quantum control experiments carried out on individual QDs can be very challenging due to the low optical signals involved. This difficulty becomes even worse when working with QDs emitting in the telecom band because of high dark current in the associated detectors. An alternate approach is to use QD ensembles as qubits since the large optical signal makes quantum state read-out much easier; however, inhomogeneities in the QD sample that lead to low-fidelity optical gates must be addressed.

This thesis work is composed of three projects which have furthered progress in the first use of pulse shaping in solid state qubit systems as well as in the development of strategies for mitigation of inhomogeneities in QD ensembles. These projects have involved the development of apparatus and extensive optical investigations of SAQDs with emission wavelengths in the 1.3 μm and 1.5 μm telecom bands, unlike the demonstrations of optical qubit control discussed above, which occur in the NIR wavelength range. Exciton qubits in control schemes have been the focus of this work as optical techniques can be efficiently applied in this case. The first project involved the design, construction, characterization, and initial testing of an infrared quantum control apparatus. The second project implemented the infrared quantum control apparatus in optimal quantum control experiments, performing simultaneous single-qubit operations on two distinct SAQDs. The third project investigated the efficacy of a one-dimensional microcavity in the spectral selection of QD subsets within an ensemble of SAQDs to be used as qubits while reducing the deleterious effects of inhomogeneity.

This thesis is organized as follows: Chapter 2 discusses the background related to the optical properties of semiconductor nanostructures, including multilayer one-dimensional cavity structures. The experimental techniques used in this thesis work are presented in Chapter 3. The results of testing the new quantum control apparatus developed in this thesis work are presented in Chapter 4 and were published in the Journal of Applied Physics. Chapter 5 contains the results of the second project in this thesis work, which involved the application of this newly constructed quantum control apparatus to the demonstration of parallel single qubit gates in different QDs. This research has been published in Nano

Letters. The results of the third project, concerning pump-probe experiments on ensembles of QDs, are presented in Chapter 6 as a manuscript submitted to Applied Physics Letters. Conclusions to this thesis work and future outlook are presented in Chapter 7.

CHAPTER 2

OPTICAL PROPERTIES OF SEMICONDUCTOR NANOSTRUCTURES

The following sections will give a brief description of the optical properties of semiconductor structures as well as the transmission characteristics of planar microcavity structures. The experiments performed in this thesis work involve the study of the interaction of ultrafast optical pulses with quantum-confined electronic states within self-assembled semiconductor quantum dots. An introduction to quantum confinement in the context of InAs self-assembled quantum dots is provided in Sec. 2.1. In Sec. 2.2 the linear optical response of quantum dots will be described, including a presentation of the optical selection rules. Section 2.3 contains a discussion of the optical control of excitons using resonant Rabi rotations, the use of pulse shaping techniques in optimal quantum control experiments, as well as a summary of the test gates used in this work. In Sec. 2.4, a transfer matrix approach describing the optical response of a one-dimensional optical cavity is provided.

2.1 Electronic Structure of III-V Semiconductors

The allowed energies of electrons in a bulk semiconductor material are described by valence and conduction energy bands. The highest-energy valence bands are separated from the lowest-energy conduction bands by a band gap, a region where no allowed electron energies exist. The allowed energies are determined by solving the Schrödinger equation including the periodic potential associated with the lattice. The resulting solutions

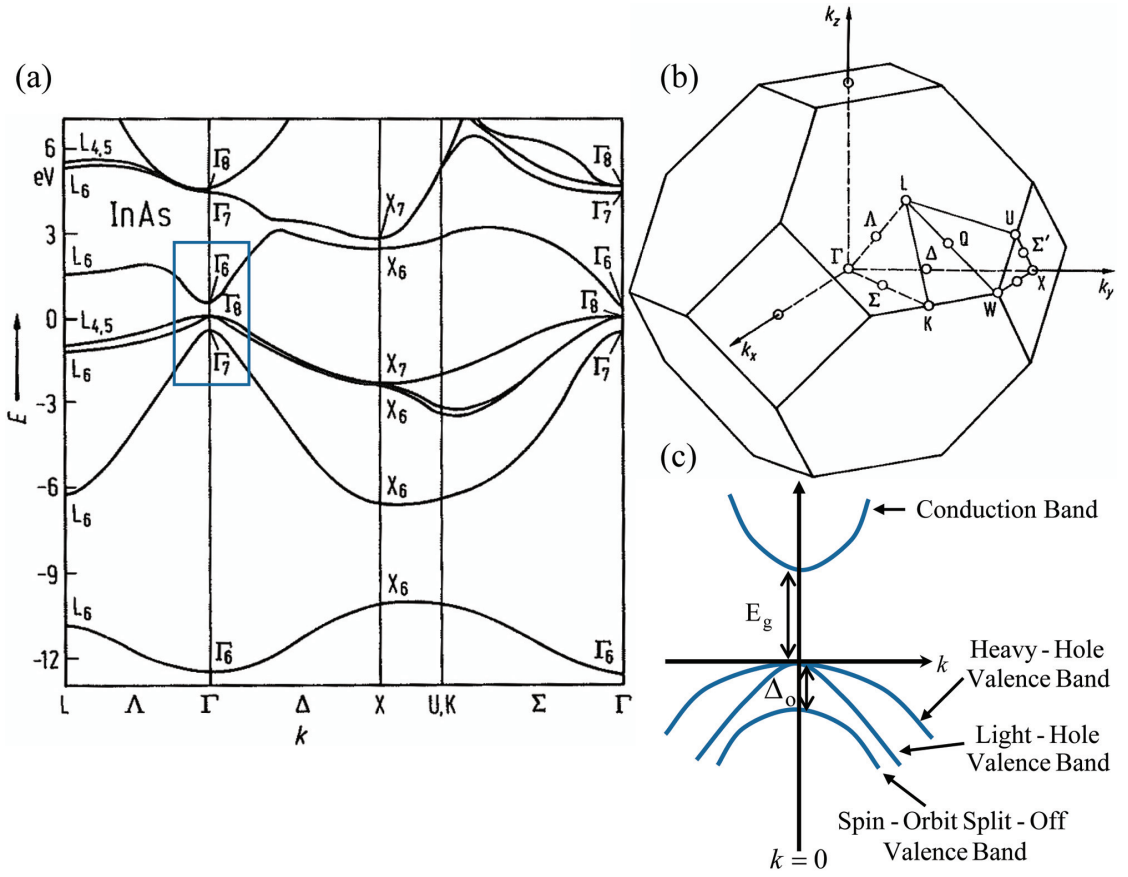

Figure 2.1: (a) Energy band structure of InAs. The horizontal axis corresponds to the electron wavevector *k* and the vertical axis to the allowed electron energies (eV). The energy bands of interest are highlighted. (b) Brillouin zone of InAs face centered cubic lattice. High-symmetry points are denoted by Γ (zone center), X, L and K, and high-symmetry lines joining some of these points are labeled Λ, Δ, and Σ. The three high symmetry directions [100], [111], and [110] are given by $\dot{\Gamma}\,\Delta\,\dot{X}$, $\dot{\Gamma}\,\Lambda\,\dot{L}$ and $\dot{\Gamma}\,\Sigma\,\dot{K}$ respectively. Adapted from Ref. [75]. (c) Simplified band diagram of InAs showing states of interest. Here, E_g is the band gap and Δ_0 is the spin-orbit splitting energy.

are Bloch functions:

$$\psi_{\nu\vec{k}}(\vec{r}) = u_{\nu\vec{k}}(\vec{r})e^{i\vec{k}\cdot\vec{r}}. \tag{2.1}$$

Bloch functions are a product of a plane wave with wavevector $\vec{k}$ and cell function $u_{\nu\vec{k}}(\vec{r})$ which contains the periodicity of the lattice, where ν is the band index. Figure 2.1(a) displays the energy band structure of InAs. Figure 2.1(c) is a simplified band diagram which displays the energy bands of interest to this thesis work for energies near the band gap region. These include the lowest energy conduction band and the three valence bands:

heavy-hole, light-hole and spin-orbit split-off bands. Each band is characterized by the total angular momentum J, of the charge carrier, as well as its projection onto the z axis characterized by the quantum number m_j.

Quantum confinement arises as a result of the band offsets between dissimilar semiconductors, such as InAs and GaAs, giving potential steps at the interfaces. In the treatment of quantum confined semiconductor heterostructures, one commonly invokes the envelope function approximation, for which the influence of these potential steps on the plane wave part of the Bloch function is taken into account and the cell function corresponding to the bulk semiconductor is retained. In order to gain insight into the electronic structure of SAQDs, one can consider a box with lateral dimensions L_x, L_y, and L_z and infinite potential barriers. Treating the plane wave part of the Bloch function using a free electron model, the Schrödinger equation is given by

$$-\frac{\hbar^2}{2m}\nabla^2\psi(\vec{r}) = E\psi(\vec{r}), \tag{2.2}$$

where m is the mass of the electron, ∇^2 is the Laplacian, $\psi(\vec{r})$ is the wavefunction, and E is the energy. The boundary conditions for this system require that $\psi(\vec{r})$ vanishes at the edges of the box (*e.g.*, for the x direction, this boundary condition corresponds to $\psi(x = 0, y, z) = \psi(x = L_x, y, z) = 0$). In this simplified system, solving Eq. 2.2 yields the allowed electronic wavefunctions which are given by:

$$\psi(z) = \sqrt{\frac{2}{L_x}}\sqrt{\frac{2}{L_y}}\sqrt{\frac{2}{L_z}}\sin\left(\frac{n_x\pi x}{L_x}\right)\sin\left(\frac{n_y\pi y}{L_y}\right)\sin\left(\frac{n_z\pi z}{L_z}\right), \tag{2.3}$$

where $n_x = 1, 2, 3...$, $n_y = 1, 2, 3...$, and $n_z = 1, 2, 3...$
The corresponding energies are given by:

$$E = E_{n_x} + E_{n_y} + E_{n_z} \tag{2.4}$$

where

$$E_{n_x} = \frac{\hbar^2\pi^2 n_x^2}{2mL_x^2}, \qquad n_x = 1, 2, 3... \tag{2.5}$$

$$E_{n_y} = \frac{\hbar^2\pi^2 n_y^2}{2mL_y^2}, \qquad n_y = 1, 2, 3... \tag{2.6}$$

$$E_{n_z} = \frac{\hbar^2 \pi^2 n_z^2}{2mL_z^2}, \qquad n_z = 1, 2, 3... \tag{2.7}$$

which are all discrete single energy levels, where n_x, n_y, and n_z are the principle quantum numbers. These energies are illustrated in Fig. 2.2(c). The density of states is given by

$$D(E) = 2\Sigma_{n_x n_y n_z} \delta \left(E - \left[E_{n_x} + E_{n_y} + E_{n_z} \right] \right) \tag{2.8}$$

and is shown in Fig. 2.3(d).

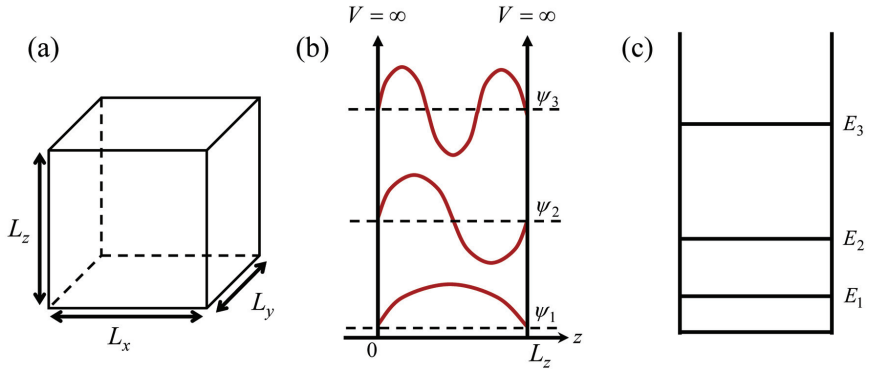

Figure 2.2: (a) Diagram of three-dimensional confinement with lateral dimensions L_x, L_y, and L_z. (b) Allowed electron wavefunctions and(c) discrete energy states corresponding to the electron wavefuntions.

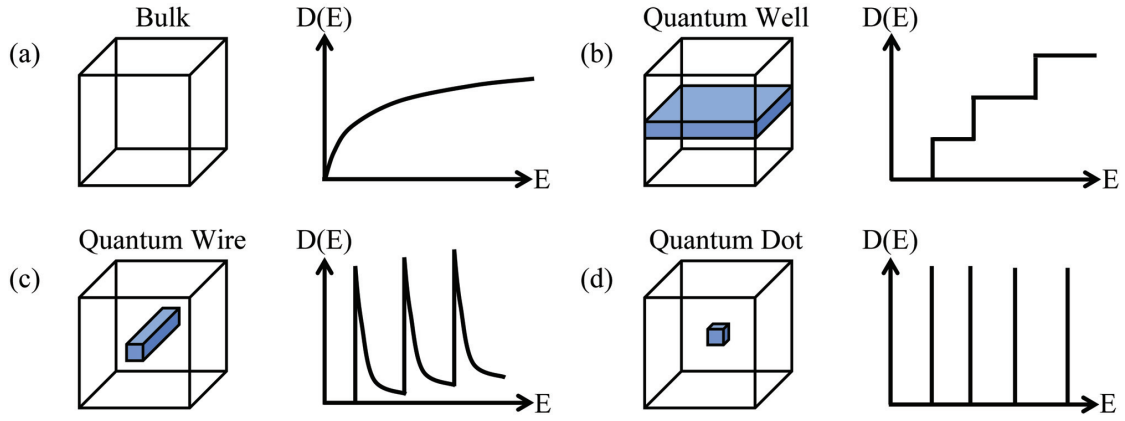

Figure 2.3: Confinement effects on the density of states. Diagrams and density of states versus energy profiles of (a) unconfined bulk material, (b) one-dimensional confinement, (c) two-dimensional confinement, and (d) three-dimensional confinement.

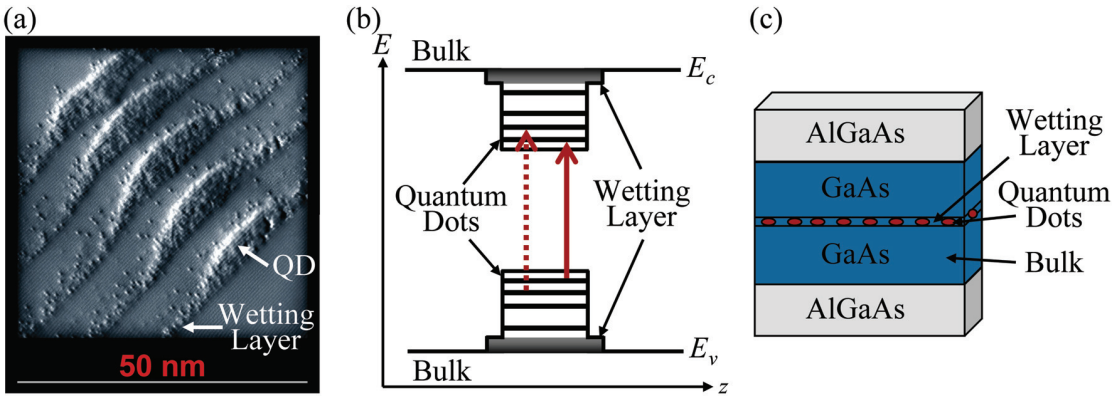

Figure 2.4: (a) STM image of five layers of InAs SAQDs grown on GaAs. The atoms forming the wetting layers underneath the QD structures are resolved. Adapted from Ref. [76]. (b) Simplified energy band structure of InAs/GaAs quantum dots. The energies of the valence band (E_v) and conduction band (E_c) are shown as a function of growth direction z. Ground state and excited state optical transitions are indicated by the solid and dashed arrows respectively. (c) Simplified diagram of layered structure of self-assembled InAs quantum dots.

In practical SAQD systems, the dots are lens shaped and have a finite potential barrier dictated by the band edge offsets between the dot material (InAs) and the bulk (GaAs). A series of discrete states will exist corresponding to each band ν in the bulk semiconductor. For example, the conduction band states can be represented as C1, C2, *etc.*, the heavy-hole valence states as HH1, HH2, *etc.*, and the light-hole valence states as LH1, LH2 and so on. The self assembly process also leads to a one-dimensionally confined region around the quantum dot, referred to as the wetting layer. A scanning tunneling microscope (STM) image of five layers of stacked InAs SAQDs grown on GaAs is shown in Fig. 2.4(a). In this image, the bright regions correspond to individual indium atoms. The band edge diagram appropriate for SAQDs is shown in Fig. 2.4(b). The wetting layer region represents a quantum well with a graded indium composition. The associated energy states correspond to a sub-band for each confined level in the growth direction (z) since the carriers are unconfined in the plane of the heterostructure (*i.e.*, the x-y plane). These delocalized sub-band states are represented in Fig. 2.4(b) by the shaded rectangles. For this thesis work, only the lowest (highest) energy confined electron (hole) levels are of interest.

2.2 Linear Optical Properties

Optical excitation may be used to promote an electron from a valence state to a conduction state in the semiconductor, leaving behind a hole. With appropriate choice of photon energy, the resulting electron-hole pair may be created in the bulk GaAs surrounding the quantum dots, the wetting layer, or inside the quantum dot. For optical excitation within the dot, light will primarily cause transitions between quantum dot states with the same principle quantum number (*i.e.*, HH1-C1, HH2-C2, *etc.*), due to the approximate orthogonality of states with different n. (In real structures with finite barrier height forbidden transitions with different principle quantum umbers are partly allowed since the different degrees of penetration of the electron and hole wavefunctions into the barrier regions prevent the envelope functions from being perfectly orthogonal.) The ground state and excited state optical transitions are indicated in Fig. 2.4(b) by the solid and dashed lines, respectively.

This optical excitation process is dependent on the polarization of the light field. The optical selection rules are determined by the matrix elements of the electric-dipole operator $\vec{\mu}$ = - e$\vec{r}$ between the cell functions of the initial and final states of the optical transition. The conduction and valence band cell functions are eigenstates of the total angular momentum operator $\vec{J} = \vec{L} + \vec{S}$, and of $\vec{J}^2$, where $\vec{L}$ and $\vec{S}$ are orbital angular momentum and spin angular momentum operators, respectively. The quantization axis for angular momentum is taken in the growth (z) direction of the semiconductor heterostructure. The cell functions can be expressed in terms of linear combinations of direct products of the eigenstates of $\vec{L}^2$ and $\vec{S}^2$. For III-V semiconductors, the allowed conduction states have quantum numbers $s = \frac{1}{2}$ and $m_s = \pm\frac{1}{2}$. The allowed valence states are given by the heavy-hole band ($j = \frac{3}{2}$ and $m_j = \pm\frac{3}{2}$), the light-hole band ($j = \frac{3}{2}$ and $m_j = \pm\frac{1}{2}$), and the spit-orbit split-off band ($j = \frac{1}{2}$ and $m_j = \pm\frac{1}{2}$), giving a total of eight energy bands, as each conduction and valence band has two spin bands. The zone center cell functions $u_{\nu\vec{k}}(\vec{r}) = \langle\vec{r}|\nu\vec{k}\rangle$ with $\vec{k} = \vec{0}$ for the conduction band are given by:

$$|\mathrm{C}\rangle_\uparrow = |s\rangle\,|s = \tfrac{1}{2}\; m_s = \tfrac{1}{2}\rangle \tag{2.9}$$

$$|\mathrm{C}\rangle_\downarrow = |s\rangle\,|s = \tfrac{1}{2}\; m_s = -\tfrac{1}{2}\rangle \tag{2.10}$$

where $\uparrow$ and $\downarrow$ denote the spin-up and spin-down bands respectively. The zone center

heavy-hole, light-hole and spin-orbit split-off valence band cell functions are given by:

$$\begin{aligned} |\mathrm{HH}\rangle_{\Uparrow} &= \left|j=\tfrac{3}{2}\, m_j=\tfrac{3}{2}\right\rangle \\ &= \left(-\tfrac{1}{\sqrt{2}}\right)\left[|x\rangle + i\,|y\rangle\right]\left|s=\tfrac{1}{2}\, m_s=\tfrac{1}{2}\right\rangle \end{aligned} \tag{2.11}$$

$$\begin{aligned} |\mathrm{HH}\rangle_{\Downarrow} &= \left|j=\tfrac{3}{2}\, m_j=\tfrac{-3}{2}\right\rangle \\ &= \left(\tfrac{1}{\sqrt{2}}\right)\left[|x\rangle - i\,|y\rangle\right]\left|s=\tfrac{1}{2}\, m_s=\tfrac{-1}{2}\right\rangle \end{aligned} \tag{2.12}$$

$$\begin{aligned} |\mathrm{LH}\rangle_{\Uparrow} &= \left|j=\tfrac{3}{2}\, m_j=\tfrac{1}{2}\right\rangle \\ &= \left(\tfrac{1}{\sqrt{3}}\right)\left(-\tfrac{1}{\sqrt{2}}\right)\left[|x\rangle + i\,|y\rangle\right]\left|s=\tfrac{1}{2}\, m_s=\tfrac{-1}{2}\right\rangle + \left(\sqrt{\tfrac{2}{3}}\right)|z\rangle\left|s=\tfrac{1}{2}\, m_s=\tfrac{1}{2}\right\rangle \end{aligned} \tag{2.13}$$

$$\begin{aligned} |\mathrm{LH}\rangle_{\Downarrow} &= \left|j=\tfrac{3}{2}\, m_j=\tfrac{-1}{2}\right\rangle \\ &= \left(\tfrac{1}{\sqrt{3}}\right)\left(\tfrac{1}{\sqrt{2}}\right)\left[|x\rangle - i\,|y\rangle\right]\left|s=\tfrac{1}{2}\, m_s=\tfrac{1}{2}\right\rangle + \left(\sqrt{\tfrac{2}{3}}\right)|z\rangle\left|s=\tfrac{1}{2}\, m_s=\tfrac{-1}{2}\right\rangle \end{aligned} \tag{2.14}$$

$$\begin{aligned} |\mathrm{SO}\rangle_{\Uparrow} &= \left|j=\tfrac{1}{2}\, m_j=\tfrac{1}{2}\right\rangle \\ &= \left(-\tfrac{1}{\sqrt{3}}\right)\left[|x\rangle + i\,|y\rangle\right]\left|s=\tfrac{1}{2}\, m_s=\tfrac{-1}{2}\right\rangle + \left(-\tfrac{1}{\sqrt{3}}\right)|z\rangle\left|s=\tfrac{1}{2}\, m_s=\tfrac{1}{2}\right\rangle \end{aligned} \tag{2.15}$$

$$\begin{aligned} |\mathrm{SO}\rangle_{\Downarrow} &= \left|j=\tfrac{1}{2}\, m_j=\tfrac{-1}{2}\right\rangle \\ &= \left(-\tfrac{1}{\sqrt{3}}\right)\left[|x\rangle - i\,|y\rangle\right]\left|s=\tfrac{1}{2}\, m_s=\tfrac{1}{2}\right\rangle + \left(\tfrac{1}{\sqrt{3}}\right)|z\rangle\left|s=\tfrac{1}{2}\, m_s=\tfrac{-1}{2}\right\rangle \end{aligned} \tag{2.16}$$

where $\langle\vec{r}|x\rangle$, $\langle\vec{r}|y\rangle$, and $\langle\vec{r}|z\rangle$ correspond to wavefunctions that are odd with respect to the three Cartesian axes and $\langle\vec{r}|s\rangle$ is spherically symetric. The conduction band cell functions have spherical (s-type) symmetry, and are even functions with respect to the three Cartesian axes. The valence band cell functions are p-type and are odd functions with respect to a single Cartesian axis, and are even functions with respect to the other two directions. The matrix elements of the electric-dipole operator can be evaluated using the properties of even and odd functions, which results in three non-zero matrix elements $\langle s|\mu_x\,|x\rangle$, $\langle s|\mu_y\,|y\rangle$, and $\langle s|\mu_z\,|z\rangle$. Considering the transition from the spin-up heavy-hole valence band to the spin-up conduction band, the matrix element is given by:

$$\begin{aligned} \langle \mathrm{C}_{\uparrow}|\mu_x|\mathrm{HH}\vec{0}_{\Uparrow}\rangle &= -\tfrac{1}{\sqrt{2}}\left[\langle s|\vec{\mu}_x\,|x\rangle + i\langle s|\vec{\mu}_x\,|y\rangle\right] \\ &= -\tfrac{1}{\sqrt{2}}\hat{x} \end{aligned} \tag{2.17}$$

$$\begin{aligned} \langle \mathrm{C}_{\uparrow}|\mu_y|\mathrm{HH}\vec{0}_{\Uparrow}\rangle &= -\tfrac{1}{\sqrt{2}}\left[\langle s|\vec{\mu}_y\,|x\rangle + i\langle s|\vec{\mu}_y\,|y\rangle\right] \\ &= -\tfrac{i}{\sqrt{2}}\hat{y} \end{aligned} \tag{2.18}$$

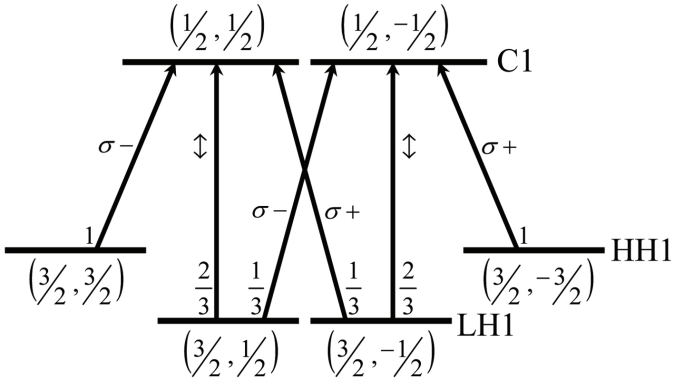

Figure 2.5: Optical selection rules of III-V semiconductor quantum dots showing the first confined level for each of the conduction, heavy-hole, and light-hole valence bands. The numbers (J, J_z) for each level are indicated and the orientation and relative magnitude of the matrix elements of the dipole operator are indicated beside the arrows representing the allowed optical transitions $\hat{\sigma}\pm = \frac{\hat{x}\pm i\hat{y}}{\sqrt{2}}$ and $\updownarrow = \hat{z}$ [77].

$$\langle \mathrm{C}_{\uparrow} | \vec{\mu} = \mu_x \hat{x} + \mu_y \hat{y} | \mathrm{HH}\vec{0}_{\Uparrow} \rangle = -\frac{1}{\sqrt{2}} \left(\hat{x} + i\hat{y} \right). \tag{2.19}$$

The optical selection rules for the heavy-hole-to-conduction and light-hole-to-conduction bands are illustrated in Fig. 2.5. The matrix element in Eq. 2.19 and the diagram in Fig. 2.5 show that resonant excitation of the lowest heavy-hole to conduction transition (HH1 - C1) with circularly-polarized light will result in a pure spin state for the resulting electron-hole pair. If linearly-polarized light is used, one will excite both spin up and down carriers with equal populations. The effects of strain and quantum confinement lift the degeneracy of the heavy-hole and light-hole valence bands, which have a relative transition strength of 3:1, as shown in Fig. 2.5.

Following excitation by a short optical pulse, the electron-hole pair may undergo a cascade of relaxation processes before ultimately recombining. The type of relaxation processes that occur depend on the type of excitation created (charge or spin) and the initial energy of the electron-hole pair. In general, carriers may interact with phonons, defects in the material, or other carriers during this relaxation process. For charge excitations (*i.e.*, an exciton or unbound electron-hole pair), the first scattering process to occur will lead to dephasing. The non-thermal (mono-energetic) carrier distribution will then thermalize to a Fermi distribution with an initial temperature determined by the initial energy of the electron and hole in the electron-hole pair relative to the associated band edges. This

is followed by energy relaxation through phonon emission which equalizes the carrier temperature with that of the lattice. Radiative recombination occurs when a photon is emitted as a result of the energy lost from an electron falling from a higher energy level to a lower energy level (*e.g.*, the conduction level to the valence level) in a semiconductor structure. This type of electron-hole recombination generates the emission detected in CWPL experiments used to characterize the electronic structure of semiconductor quantum dots.

2.3 Coherent Optical Control of Excitonic Transitions

Prior to the dephasing process described in the previous section, the evolution of the electron hole pairs are said to be in the "coherent regime". Optical excitation and subsequent manipulation of the quantum state of the electron-hole pair during this regime is referred to as "coherent control". We will consider the ground state-to-exciton transition as a simple two-level system, where the ground state is represented by $|0\rangle$ and the exciton state by $|1\rangle$. We assume that the energy of the exciton is $\hbar\omega_{01}$, as shown in Fig. 2.6(a). In the presence of a monochromatic plane wave of frequency ω, the system can undergo transitions between $|0\rangle$ and $|1\rangle$. The Hamiltonian describing the system is:

$$\hat{\mathrm{H}} = \hat{\mathrm{H}}^{(0)} + \hat{\mathrm{H}}_{\mathrm{int}} \tag{2.20}$$

where $\hat{\mathrm{H}}^{(0)}$ is the unperturbed Hamiltonian with $\hat{\mathrm{H}}^{(0)}|0\rangle = \mathrm{E}_0^{(0)}|0\rangle$ and $\hat{\mathrm{H}}^{(0)}|1\rangle = \mathrm{E}_1^{(0)}|1\rangle$, (*i.e.*, so that $\hbar\omega_{01} = \mathrm{E}_1^{(0)} - \mathrm{E}_0^{(0)}$) and where $\hat{\mathrm{H}}_{\mathrm{int}}$ describes the time-dependent interaction with the electric field of the applied light. Within the electric-dipole and rotating-wave approximations, this interaction is of the form:

$$\hat{\mathrm{H}}_{\mathrm{int}} = \begin{bmatrix} 0 & \{-\frac{(\vec{\mu}_{10}\cdot\vec{E}_0)}{2}e^{-\mathrm{i}\omega t}\} \\ \{-\frac{(\vec{\mu}_{10}\cdot\vec{E}_0)^*}{2}e^{\mathrm{i}\omega t}\} & 0 \end{bmatrix}. \tag{2.21}$$

In Eq. 2.21, E_0 is the field amplitude and $\vec{\mu}_{01}$ and $\vec{\mu}_{10}$ are the matrix elements of the electric-dipole operator $\vec{\mu}$ = - e$\vec{r}$ between $|0\rangle$ and $|1\rangle$. In the presence of $\hat{\mathrm{H}}_{\mathrm{int}}$, the state of the system is

$$|\psi(t)\rangle = c_0(t)\,|0\rangle + c_1(t)\,|1\rangle\,. \tag{2.22}$$

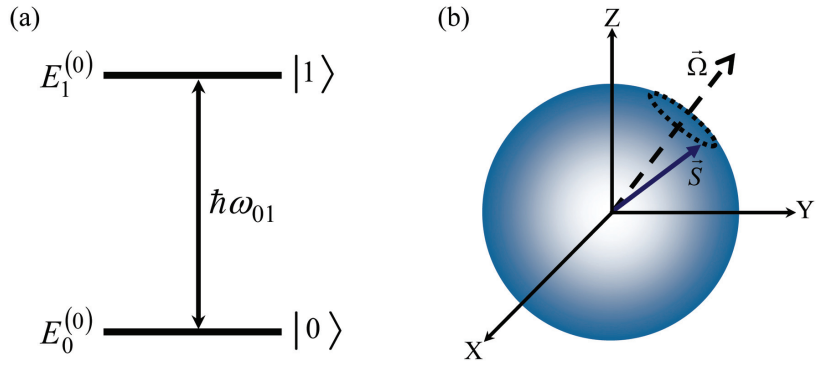

Figure 2.6: (a) Energy level diagram of two-level system with ground state $|0\rangle$ and excited state $|1\rangle$. (b) Bloch sphere representation of the precession of the Bloch vector about $\vec{\Omega}$ in the presence of a driving monochromatic electric field.

The interaction of the laser pulse with the two-level system can be described using a density matrix formalism, where the Liouville equation is given by

$$\frac{\partial \rho}{\partial t} = \frac{i}{\hbar}\left[\rho, \hat{\mathrm{H}}\right], \tag{2.23}$$

and ρ is the density matrix which describes the ensemble average of quantum state. In matrix form, ρ can be expressed as

$$\rho = \begin{bmatrix} \rho_{11} & \rho_{10} \\ \rho_{01} & \rho_{00} \end{bmatrix} = \begin{bmatrix} |c_1|^2 & c_1 c_0^* \\ c_0 c_1^* & |c_0|^2 \end{bmatrix}. \tag{2.24}$$

The diagonal elements in Eq. 2.24 are the occupation probabilities of the two energy levels and the off-diagonal elements describe the coherence of the system. One can solve for the time-dependent density matrix using Eq. 2.23, which gives four equations for the two-level system. However, as the elements of ρ are related ($\rho_{10} = \rho_{01}^*$ and $\rho_{00} + \rho_{11} = 1$), only two equations are needed to describe the system dynamics. Within the electric dipole, rotating wave, and relaxation-time approximations, these equations, called the Optical Bloch equations, are given by:

$$\frac{\partial \widetilde{\rho}_{10}}{\partial t} = -i\Delta\widetilde{\rho}_{10} + i\frac{\chi_R}{2}(2\widetilde{\rho}_{11} - 1) - \frac{\widetilde{\rho}_{10}}{\mathrm{T}_2} \tag{2.25}$$

$$\frac{\partial \widetilde{\rho}_{11}}{\partial t} = -i\left[\frac{\chi_R}{2}\widetilde{\rho}_{01} - \widetilde{\rho}_{10}\frac{\chi_R^*}{2}\right] - \frac{\widetilde{\rho}_{11}}{\mathrm{T}_1} \tag{2.26}$$

where $\Delta \equiv \omega_{01} - \omega$ is the laser detuning and $\chi_R = -\frac{\vec{\mu}_{10} \cdot \vec{E}_0}{\hbar}$ is the Rabi frequency. The change of variables

$$\rho_{10}(t) = \widetilde{\rho}_{10}(t) e^{-i\omega t} \tag{2.27}$$

$$\rho_{01}(t) = \widetilde{\rho}_{01}(t) e^{i\omega t} \tag{2.28}$$

$$\rho_{11}(t) = \widetilde{\rho}_{11}(t) \tag{2.29}$$

$$\rho_{00}(t) = \widetilde{\rho}_{00}(t) \tag{2.30}$$

is a result of invoking the rotating wave approximation and removes the fast variations in the coherences. T_1 is the longitudinal decay time, reflecting the time evolution of the occupation in $|1\rangle$ and T_2 is the transverse decay time, reflecting the decay of coherence.

This two-level system may be characterized by the value of three variables S_x, S_y, and S_z which form the $\hat{\mathrm{X}}$, $\hat{\mathrm{Y}}$ and $\hat{\mathrm{Z}}$ components of the optical Bloch vector $\vec{S}$=(S_x,S_y,S_z). These components are given by [78]:

$$S_x = \rho_{10} + \rho_{01} = c_1 c_0^* + c_0 c_1^* = 2\mathrm{Re}\{c_1 c_0^*\} \tag{2.31}$$

$$S_y = i(\rho_{10} - \rho_{01}) = \mathrm{i}(c_1 c_0^* - c_0 c_1^*) = -2\mathrm{Im}\{c_1 c_0^*\} \tag{2.32}$$

$$S_z = \rho_{11} - \rho_{00} = |c_1|^2 - |c_0|^2. \tag{2.33}$$

Since the Bloch vector is normalized, the tip always lies on the unit sphere. All points on the sphere uniquely determine a state of the two-level system. In the presence of $\hat{\mathrm{H}}_{\mathrm{int}}$, the Bloch vector satisfies

$$\frac{d\vec{S}}{dt} = \vec{\Omega} \times \vec{S} \tag{2.34}$$

where

$$\vec{\Omega} = \left(-\frac{\mu E_0}{\hbar}, 0, \Delta \right). \tag{2.35}$$

Here we have assumed that the electric field is polarized in the x-direction and $\mu_{01x} \equiv \mu$. The Bloch vector precesses about the field vector $\vec{\Omega}$ at frequency $\left|\vec{\Omega}\right|$ as shown in Fig. 2.6. Thus, the electric field of the applied light provides an effective means of controlling the state of the two-level system.

For resonant excitation of the two-level system (Δ = 0), and assuming that the Bloch vector is initially pointing downward (so that $S_z\,(t = 0)$ = -1, and the system is in state

$|0\rangle$) one can show that Eq. 2.34 has solutions of the form:

$$S_y(t) = -\sin\left(\frac{\mu E_0 t}{\hbar}\right) \tag{2.36}$$

$$S_z(t) = -\cos\left(\frac{\mu E_0 t}{\hbar}\right). \tag{2.37}$$

These solutions correspond to oscillations of the Bloch vector around the Bloch sphere about the -$\hat{\mathrm{X}}$ direction at a rate of $(\mu E_0/\hbar)$. This corresponds to a time-dependent oscillation of the state occupations, and is referred to as a resonant Rabi oscillation. From the definition of $\vec{S}$, this gives:

$$\rho_{00} = \frac{1}{2}\left(1 + \cos\left(\frac{\mu E_0 t}{\hbar}\right)\right) \tag{2.38}$$

and

$$\rho_{11} = \frac{1}{2}\left(1 - \cos\left(\frac{\mu E_0 t}{\hbar}\right)\right). \tag{2.39}$$

In the case of pulsed optical excitation, the field amplitude E_0 is not constant. Provided the pulse phase is constant and $E_0\,(t)$ varies slowly compared to an optical cycle, the above solution is still valid. The degree of rotation is then represented by an integral, called the pulse area, given by:

$$\Theta(t) = \int_0^t dt'\,\mu\frac{E_0(t')}{\hbar}. \tag{2.40}$$

The pulse area determines the change in state occupation, or the degree of rotation as represented on the Bloch sphere. From Eq. 2.38 and Eq. 2.39, we can see that a pulse area of π will rotate the Bloch vector by 180° and invert the occupation of the two-level system (*i.e.*, control the occupation of the exciton level $|1\rangle$).

The above development corresponds to the case of a real electric field. In the more general case, the field vector is given by

$$\vec{\Omega} = \left(-\mathrm{Re}\left[\frac{\mu E_0}{\hbar}\right], \mathrm{Im}\left[\frac{\mu E_0}{\hbar}\right], \Delta\right). \tag{2.41}$$

One can utilize the phase of the optical pulse as a means to rotate the Bloch vector about an arbitrary axis in the XY plane. This approach is used to measure decoherence times [79] and provides a way to perform full quantum state tomography [80]. In these types

of experiments, a pair of phase-locked $\pi/2$-pulses are used. The first pulse rotates the Bloch vector about -$\hat{\mathrm{X}}$ and the second pulse rotates the Bloch vector about a second axis, defined by the relative phase of the two pulses. In the case of quantum state tomography, the in-plane components of the Bloch vector are projected onto the Z-axis by a suitable laser pulse. Measurement of the occupation then provides a measurement of that in-plane component. For example, if the phase of the field is $\pi/2$, one projects the X-component of the Bloch vector onto the Z-axis. Ultrafast pulses can be engineered to have specific wavelength, amplitude and spectral phase components. In this case, the trajectory on the Bloch sphere can be much more complex compared to that for a real electric field. This capability allows one to tailor the quantum state dynamics in a flexible way, as described in the next section.

2.3.1 Optimal Quantum Control Using Pulse Shaping

In the ultrafast control of the two-level system, the pulse area can be modified by controlling the average pulse power, or by changing the pulse duration through adjustments at the laser source or through external optical components. In order to realize a general target state in a quantum dot system (*i.e.*, a particular point on the Bloch sphere), one can fine tune the phase and/or amplitude components of the applied laser field using femtosecond pulse shaping techniques, through which one achieves complete control over the phase and amplitude of the individual frequency components of the optical pulse.

As in Eq. 2.21, the interaction of the laser field and the two-level system is described by $H_{\mathrm{int}} = -\vec{\mu} \cdot \vec{E}(t)$, where $\vec{E}(t) = \frac{1}{2}\hat{\epsilon}E_0(t)[\exp(-i\omega t - i\phi(t)) + \exp(i\omega t + i\phi(t))]$ is the electric field of the optical pulse, and here we have allowed the amplitude $E_0(t)$ and the phase $\phi(t)$ to be time-dependent. Full control of the pulse amplitude and phase can be achieved by using a spatial light modulator (SLM) as the spatial mask within a 4-f pulse shaper geometry, shown in Fig. 2.7(a). An SLM uses a nematic liquid crystal (LC) array (Fig. 2.7(b)) in which the pixels have an electrically tunable index of refraction, allowing for control over the phase of the incident light. Within the SLM, the phase retardance caused by the applied voltage *V* is given by

$$\Delta\phi = \omega\Delta n(V)l/c \tag{2.42}$$

where $\Delta n(V)$ is the voltage dependent index of refraction, l is the thickness of the LC layer,

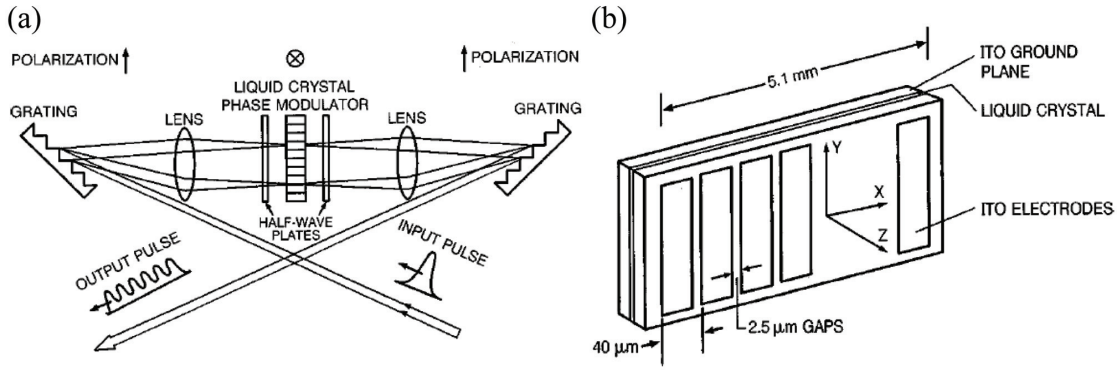

Figure 2.7: (a) Programmable 4-f pulse shaper geometry with a liquid crystal array for phase modulation. Here, f refers to the focal length of the lenses involved, creating a geometry which is four times f in length. (b) Diagram of electronically addressable liquid crystal array. Adapted from Ref. [81].

ω is the angular frequency of the incident light and c is the speed of light in vacuum [82]. In the frequency domain, the SLM can be used to impose a mask function $M(\omega)$, given by the product of the frequency-dependent amplitude $A_M(\omega)$ and phase $\Phi_M(\omega)$ masks

$$M(\omega) = A_M(\omega) \exp\left[i\Phi_M(\omega)\right]. \tag{2.43}$$

The Fourier transform of the ultrafast pulse exiting the shaper is described by

$$\tilde{E}_{\text{out}}(\omega) = \tilde{E}_{\text{in}}(\omega)\, M(\omega)\,, \tag{2.44}$$

where $\tilde{E}_{\text{in}}(\omega)$ is the Fourier transform of the transform-limited (TL) input pulse, $E(t) = |E_0|\text{sech}(1.76t/\tau)\exp(i\omega t)$, and τ is the pulse duration. The SLM used in this work has 128 pixels. The mask $M(\omega)$ is designed to be sufficiently slowly varying with ω that the focused spot sizes of the individual frequency components at the mask are small compared to these variations.

2.3.2 Test Gates for Optimal Quantum Control

Two test gates were chosen in order to assess the application of optimal quantum control to SAQDs. The first test gate considered in this work was the C-ROT gate, a two-qubit gate that utilizes excitonic states in an individual QD. The C-ROT is achieved using a four-level system created by the vacuum ground state $|00\rangle$, two oppositely-polarized exciton states ($|01\rangle$ and $|10\rangle$), and the bound biexciton state $|11\rangle$. The C-ROT implements a π rotation

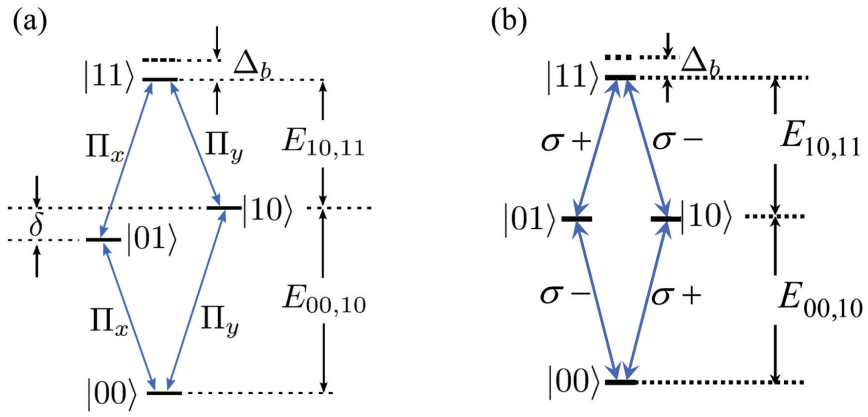

Figure 2.8: Level diagrams for C-ROT gate where $|00\rangle$, $|01\rangle$, $|10\rangle$, $|11\rangle$, and Δ_b are the ground state, oppositely polarized exciton states, the biexciton state, and the biexciton binding energy respectively. (a) Diagram for a QD with an elongated structure, lifting the degeneracy between the oppositely polarized exciton states by an amount equal to the exchange splitting δ. (b) Diagram for a QD with cylindrical symmetry with degenerate exciton states. The selection rules in (a) permit Π_x or Π_y linearly polarized excitation, while circularly polarized $\sigma\pm$ excitation is used in (b).

on the second qubit if and only if the control qubit is present. Figure 2.8 shows two energy level schemes for the C-ROT gate in QDs with different shapes. In InAs/GaAs SAQDs, the anisotropic exchange interaction along with a slight elongation of the QD lifts the degeneracy between the exciton states and leads to linearly-polarized optical selection rules (Fig. 2.8(a)). For QDs with cylindrical symmetry, the oppositely-spin-polarized exciton states are nominally degenerate and circularly-polarized optical selection rules are used (Fig. 2.8(b)). The C-ROT is a unitary rotation described by the following transformation matrix [28]:

$$\hat{U}_{C-ROT} = \begin{bmatrix} 1 & 0 & 0 & 0 \\ 0 & 1 & 0 & 0 \\ 0 & 0 & 0 & -1 \\ 0 & 0 & 1 & 0 \end{bmatrix}. \tag{2.45}$$

The result of the C-ROT rotation is determined using matrix algebra: $|\psi_f\rangle = \hat{U}\,|\psi_i\rangle$ where $|\psi_i\rangle$ and $|\psi_f\rangle$ are the initial and final states of the system. Considering initial occupation

in $|00\rangle$ as an example, for which the control qubit is absent:

$$|\psi_f\rangle = \begin{bmatrix} 1 & 0 & 0 & 0 \\ 0 & 1 & 0 & 0 \\ 0 & 0 & 0 & -1 \\ 0 & 0 & 1 & 0 \end{bmatrix} \begin{bmatrix} 1 \\ 0 \\ 0 \\ 0 \end{bmatrix} = \begin{bmatrix} 1 \\ 0 \\ 0 \\ 0 \end{bmatrix} \tag{2.46}$$

where the final state occupation is also in $|00\rangle$, as required. In the case where control qubit is present, with initial occupation in the exciton state $|10\rangle$, we have:

$$|\psi_f\rangle = \begin{bmatrix} 1 & 0 & 0 & 0 \\ 0 & 1 & 0 & 0 \\ 0 & 0 & 0 & -1 \\ 0 & 0 & 1 & 0 \end{bmatrix} \begin{bmatrix} 0 \\ 0 \\ 1 \\ 0 \end{bmatrix} = \begin{bmatrix} 0 \\ 0 \\ 0 \\ 1 \end{bmatrix}. \tag{2.47}$$

The right side of Eq. 2.47 indicates that a π rotation was performed on the second qubit and the final occupation is in the $|11\rangle$ state, as required. Similar to the C-ROT, a controlled-NOT gate, or C-NOT operation, also inverts the target qubit if the control qubit is present; however, the transformation matrix for the C-NOT contains only positive elements. The C-ROT rotation is easier to experimentally realize than a C-NOT operation [22, 28] and is considered in the first project of this thesis work. The C-ROT was experimentally realized in elongated QDs (Fig. 2.8(a)) by Li *et. al.* [28] using TL optical pulses as discussed in Sec. 1.3 and Sec. 1.5.1.2, where a two-colour excitation scheme was utilized. A pre-pulse tuned to an exciton transition was used to prepare the control qubit (*i.e.*, initialize the state in $|10\rangle$). A second laser pulse tuned to the exciton-to-biexciton transition was then used to manipulate the state of the second qubit (*i.e.*, induce a transition from $|10\rangle$ to $|11\rangle$). Shaped femtosecond pulses can also be used to implement a C-ROT gate on an individual QD, as proposed theoretically by Chen *et. al.* [22]. Chapter 4 shows the experimental realization and characterization of shaped femtosecond pulses optimized using optimal quantum control considering the C-ROT level scheme in Fig. 2.8(b). A single shaped optical pulse is designed to implement a C-ROT considering four initial states corresponding to unit occupation of each of the basis states of the four-level system. The general approach used to optimize the pulse shaping mask is discussed in the following section.

The second test gate considered in this thesis work involves parallel single qubit gates

in two distinct QDs (*i.e.*, QDs with distinct transition energies and dipole moments). In particular, the gate consists of simultaneous π and 2π rotations on uncoupled exciton qubits in distant QDs. These single qubit rotations are characterized by rotation operators, which describe rotations about the Bloch sphere. The single qubit π rotation inverts the state occupation of the two-level system, which rotates the Bloch vector about the X axis. For an arbitrary angle of rotation, the rotation operator is given by:

$$R_x(\theta) = \begin{bmatrix} \cos\frac{\theta}{2} & -i\sin\frac{\theta}{2} \\ -i\sin\frac{\theta}{2} & \cos\frac{\theta}{2} \end{bmatrix}, \tag{2.48}$$

where θ is the angle of rotation. The single QD two-level system consists of the vacuum ground state $|0\rangle$ and exciton state $|1\rangle$. A π rotation about X, considering initial occupation in the ground state, is given by:

$$|\psi_f\rangle = \begin{bmatrix} \cos\frac{\pi}{2} & -i\sin\frac{\pi}{2} \\ -i\sin\frac{\pi}{2} & \cos\frac{\pi}{2} \end{bmatrix} \begin{bmatrix} 1 \\ 0 \end{bmatrix} = -i \begin{bmatrix} 0 \\ 1 \end{bmatrix} \tag{2.49}$$

which transfers the state occupation from $|0\rangle$ to $|1\rangle$ with a change in the overall phase by -i. For a 2π rotation with the same initial conditions,

$$|\psi_f\rangle = \begin{bmatrix} \cos\frac{2\pi}{2} & -i\sin\frac{2\pi}{2} \\ -i\sin\frac{2\pi}{2} & \cos\frac{2\pi}{2} \end{bmatrix} \begin{bmatrix} 1 \\ 0 \end{bmatrix} = - \begin{bmatrix} 1 \\ 0 \end{bmatrix} \tag{2.50}$$

where the resulting state occupation is in $|0\rangle$, but with a negative sign representing a change in the overall phase. These phase changes are characteristic of spin-$\frac{1}{2}$ systems. The parallel control gate considered here (*i.e.*, a π rotation on qubit 1 and 2π rotation on qubit 2) is a four by four block diagonal matrix given by

$$\hat{U}_{par} = \begin{bmatrix} 0 & -i & 0 & 0 \\ -i & 0 & 0 & 0 \\ 0 & 0 & -1 & 0 \\ 0 & 0 & 0 & -1 \end{bmatrix}. \tag{2.51}$$

Single qubit rotations can be achieved using a TL optical pulse with a pulse area corresponding to the desired degree of rotation. The accurate parallel control of two

separate QDs with different transition energies and dipole moments is not possible with a single TL pulse. By implementing optimal quantum control and pulse shaping techniques, simultaneous control of two independent two-level systems in separate QDs is attainable (Chapter 5).

2.3.3 Pulse Shaping Mask Optimization

In this work, femtosecond pulse shaping was used to optimize the fidelity of two quantum gates: (*i*) a C-ROT gate involving two opposite-spin polarized excitons in the same QD, and (*ii*) parallel single qubit gates on two distant distinct QDs. The fidelity of a gate is given by:

$$F = \mathrm{Tr}[\rho_{\mathrm{ph}}\rho_{\mathrm{id}}], \tag{2.52}$$

where ρ_{ph} is the physical density matrix at the end of the laser pulse and ρ_{id} is the ideal density matrix for the quantum gate. In both cases, the quantum state dynamics were optimized numerically by a fellow graduate student Reuble Mathew as a component of his doctoral thesis work. In case (*i*), the optimized pulses were generated experimentally by the author to provide a means of testing the functionality of the new quantum control apparatus constructed by the author (Chapter 4). In case (*ii*), the optimized pulses were implemented experimentally by the author in coherent control experiments on QDs (Chapter 5).

The optical Bloch equations for the four-level system of two excitons in a single QD (Fig. 1.3(b)) is a direct extension of the single exciton treatment presented in Sec. 2.3 and is detailed extensively in Ref. [83], and briefly in Ref. [84] (Chapter 4) and is omitted here for brevity. The mathematical treatment of excitons in separate QDs involves the simultaneous numerical evaluation of independent two-level systems (Sec. 2.3) under excitation by the same optical pulse. For each of the target quantum state dynamics in (*i*) and (*ii*), the optimization of the pulse shape was carried out numerically by choosing a specific functional form for the mask applied to the SLM, with parameters that could be adjusted to optimize the fidelity of the gate. For example, the following phase-only shaping mask:

$$\Phi_M(\omega) = \alpha \cos\left[\gamma(\omega - \omega_0) - \varphi\right], \tag{2.53}$$

containing the free parameters α (the amplitude), γ (spectral frequency), and φ (phase shift), and together with the pulse area Θ, form input vectors $\vec{q_i} = \{\alpha_i, \gamma_i, \varphi_i, \Theta_i\}$. The optical Bloch equations were solved numerically for a set of ≈ 500 specific values of the

input vectors $\vec{q_i}$, within the experimentally accessible parameter space for the pulse shaping system, to obtain the density matrix ρ_{ph} at the end of the laser pulse. This density matrix was used to evaluate the fidelity in Eq. 2.52. The optimum value of fidelity found within the set of input vectors allowed the optimum mask function to be determined. Details of experimental implementation are described in the Chapter 3.

2.4 Optical Microcavities

The focus of this thesis work is on a one-dimensional λ-microcavity in which the mirrors are fabricated using eight period $\lambda/4$ SiO_2/Ta_2O_5, with a final $\lambda/2$ layer of Ta_2O_5, Bragg stacks. These Bragg stacks surround an InP spacer layer (thickness λ) containing the InAs semiconductor QDs. This type of cavity is similar to the $\lambda/2$ structure shown in Fig. 3.4(a) and is described in more detail in Sec. 3.1. In the third component of this thesis work, this structure was studied using angle-resolved PL and pump-probe spectroscopy techniques. These experiments investigated the efficacy of using the angle-dependent transmission resonance of a planar microcavity for the spectral selection of subsets of QDs within the ensemble. This section will summarize a transfer matrix approach to calculating the transmission and reflection coefficients for this type of microcavity structure.

2.4.1 Microcavity Transmission and Reflection

The transfer matrix for a multilayer system can be found by multiplying the matrices which describe each of the optical elements within the structure. There are two types of matrices to consider, the first describes the reflection and transmission of an electric field at an interface between two dielectric materials, and the second describes the phase accumulated by an electric field when traveling through a dielectric material.

Figure 2.9(a) shows a diagram of an electric field normally incident on three dielectric layers. Considering the first interface between regions 0 and 1, E_{+}^{0} and E_{-}^{0} represent the sum of all waves in region 0 at the interface, traveling to the right and to the left respectively. Similarly, E_{+}^{1} and E_{-}^{1} denote the fields in region 1, traveling to the right and to the left respectively. The reflection and transmission coefficients at this interface are given by:

$$\mathrm{r}_{01} = \frac{\mathrm{E}_{-}^{0}}{\mathrm{E}_{+}^{0}} = \frac{\mathrm{n}_0 - \mathrm{n}_1}{\mathrm{n}_0 + \mathrm{n}_1} = -\mathrm{r}_{10} \tag{2.54}$$

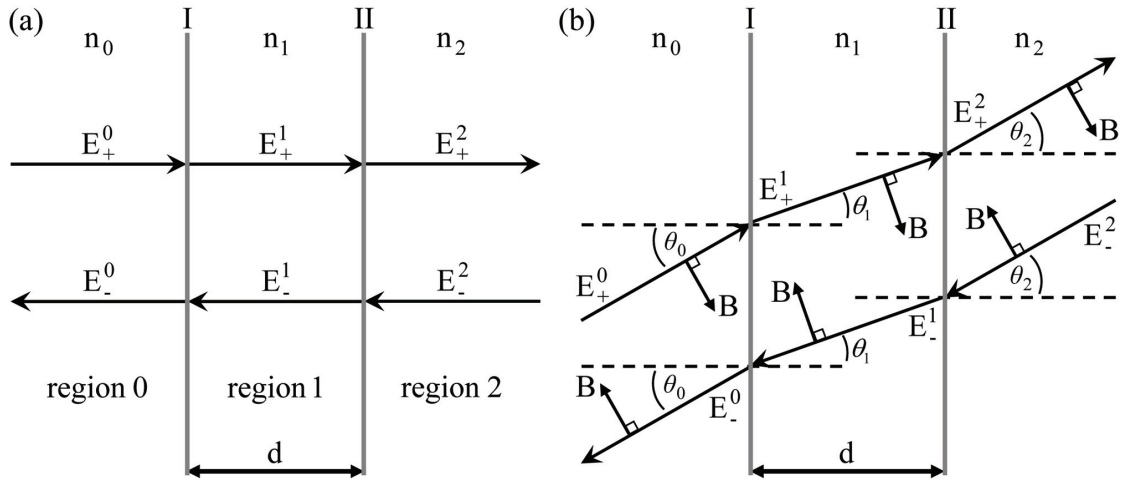

Figure 2.9: (a) Electric field at normal incidence to a multilayer dielectric system. (b) Light propagating through two dielectric interfaces at non-normal incidence [85].

and

$$\mathrm{t}_{01} = \frac{\mathrm{E}_{+}^{1}}{\mathrm{E}_{+}^{0}} = \frac{2\mathrm{n}_0}{\mathrm{n}_0 + \mathrm{n}_1}, \tag{2.55}$$

where n_0 and n_1 are the refractive indices of the media forming the interface. Using boundary conditions for electro-magnetic waves, the electric fields before and after an interface can be expressed in matrix form:

$$\begin{bmatrix} \mathrm{E}_{+}^{0} \\ \mathrm{E}_{-}^{0} \end{bmatrix} = \frac{1}{\mathrm{t}_{01}} \begin{bmatrix} 1 & \mathrm{r}_{01} \\ \mathrm{r}_{01} & 1 \end{bmatrix} \begin{bmatrix} \mathrm{E}_{+}^{1} \\ \mathrm{E}_{-}^{1} \end{bmatrix}. \tag{2.56}$$

The electric field does not undergo any reflections while traveling through region 1; however, E_{+}^{1} and E_{-}^{1} accumulate a phase given by $k_1\mathrm{d}$, where d is the thickness of the material, $k_1 = 2\pi/\lambda_1$, and the wavelength inside the dielectric material λ_1 is dependent on the wavelength of light in vacuum λ_0, as $\lambda_1 = \lambda_0/\mathrm{n}_1$. This phase accumulation can be written as

$$\begin{bmatrix} \mathrm{E}_{+}^{\mathrm{I}} \\ \mathrm{E}_{-}^{\mathrm{I}} \end{bmatrix} = \begin{bmatrix} e^{-ik_1\mathrm{d}} & 0 \\ 0 & e^{+ik_1\mathrm{d}} \end{bmatrix} \begin{bmatrix} \mathrm{E}_{+}^{\mathrm{II}} \\ \mathrm{E}_{-}^{\mathrm{II}} \end{bmatrix}, \tag{2.57}$$

where E^{I} and E^{II} are the electric fields at interfaces I and II respectively. Propagation through the entire multilayer system is described by multiplying the 2 by 2 matrices which represent each interface and region throughout the microcavity, such as the 2 by 2 matrices in Eq. 2.56 and Eq. 2.57. The electric field transmitted by the microcavity, E^{t}, can be

calculated using matrix multiplication:

$$\begin{bmatrix} \mathrm{E}_{+}^{0} \\ \mathrm{E}_{-}^{0} \end{bmatrix} = \mathrm{A} \begin{bmatrix} \mathrm{E}_{+}^{t} \\ \mathrm{E}_{-}^{t} \end{bmatrix} \tag{2.58}$$

where A is the transfer matrix for j optical elements, $\mathrm{A} = \mathrm{A_1A_2A_3A_4...A}_j$, and $\mathrm{t}_s = \mathrm{E}_{+}^{t}/\mathrm{E}_{+}^{0}$ is the transmission coefficient of the system. By performing matrix algebra for different values of λ_0, the transmission spectrum of the microcavity may be calculated.

2.4.2 Angle Dependence of Microcavity Transmission and Reflection

Figure 2.9(b) illustrates the case where the light incident on the microcavity is at an angle. At each interface, the angle of incidence will depend on Snell's law ($\mathrm{n}_0 \sin\theta_0 = \mathrm{n}_1 \sin\theta_1$). As in the previous section, the electromagnetic field develops a phase difference as it propagates through the material. Considering region 1, the accumulated phase is given by:

$$\delta_{\mathrm{p}} = \frac{2\pi}{\lambda_0} \mathrm{n}_1 \mathrm{d} \cos\theta_1. \tag{2.59}$$

In a matrix representation, the electromagnetic field at boundary I can be related to the field at boundary II:

$$\begin{bmatrix} \mathrm{E_I} \\ \mathrm{B_I} \end{bmatrix} = \begin{bmatrix} \cos\delta_{\mathrm{p}} & \frac{i}{\gamma_1}\sin\delta_{\mathrm{p}} \\ i\gamma_1 \sin\delta_{\mathrm{p}} & \cos\delta_{\mathrm{p}} \end{bmatrix} \begin{bmatrix} \mathrm{E_{II}} \\ \mathrm{B_{II}} \end{bmatrix} = \begin{bmatrix} a_{11} & a_{12} \\ a_{21} & a_{22} \end{bmatrix} \begin{bmatrix} \mathrm{E_{II}} \\ \mathrm{B_{II}} \end{bmatrix}. \tag{2.60}$$

The transmission coefficient of the multilayer system is given by

$$\mathrm{t} = \frac{2\gamma_0}{\gamma_0 a_{11} + \gamma_0\gamma_2 a_{12} + a_{21} + \gamma_2 a_{22}}. \tag{2.61}$$

Here,

$$\gamma_0 \equiv \mathrm{n}_0 \sqrt{\epsilon_0\mu_0} \cos\theta_0 \tag{2.62}$$

$$\gamma_1 \equiv \mathrm{n}_1 \sqrt{\epsilon_0\mu_0} \cos\theta_1 \tag{2.63}$$

$$\gamma_2 \equiv \mathrm{n}_2 \sqrt{\epsilon_0\mu_0} \cos\theta_2. \tag{2.64}$$

In this case, the polarization of the incident electric field is chosen to be perpendicular to the plane of incidence of the cavity structure. For an incident electric field parallel to the plane of incidence, $\gamma_x = (\mathrm{n}_x\sqrt{\epsilon_0\mu_0})/(\cos\theta_x)$ [85]. The angle-dependent transmission

spectrum of the microcavity can be calculated using matrix algebra as discussed above. For increasing angles of incidence, the microcavity mode increases in energy and could be utilized for the optical encoding of qubits in a QD ensemble within a one-dimensional microcavity by selectively addressing subsets of QDs with transition energies resonant with the cavity mode.

CHAPTER 3

EXPERIMENTAL METHODS

This thesis work involved optical investigations of single semiconductor quantum dots as well as a quantum dot ensemble. The following is a brief description of the types of samples and spectroscopic techniques used. In Sec. 3.1, details of the self-assembled quantum dot structures studied in this work are provided. Section 3.2 contains a description of the continuous-wave photoluminescence and photoluminescence excitation techniques used for the characterization of these quantum dot structures. Ultrafast pulse shaping is presented in Sec. 3.3. Dispersion compensation and the experimental approach to optical control experiments are described in Sec. 3.4 and Sec. 3.5, followed by time-resolved pump-probe spectroscopy methods in Sec. 3.6.

3.1 Self-Assembled Quantum Dots

The semiconductor quantum dot samples investigated in this thesis work were grown using epitaxial techniques by the research groups of Dennis Deppe at the University of Central Florida and Robin Williams at the National Research Council of Canada. The self-assembly technique is described here for clarity. One deposits a few monolayers of one material onto another bulk material with a different lattice constant. For example, consider InAs quantum dots fabricated inside of bulk GaAs. At the interface, the deposited InAs monolayers will spontaneously form small islands due to the strain caused by the lattice mismatch. More GaAs is then deposited on top of these islands, resulting in three dimensional confinement of the InAs. The GaAs deposited directly after the InAs islands does not form a pure interface with the previous layers of GaAs. The result is a graded composition of InGaAs in the plane of the InAs islands, referred to as the wetting layer.

This layer acts as a one-dimensionally confined region. A simplified energy band diagram of the resulting InAs/GaAs quantum dots is shown in Fig. 2.4(b).

The self-assembled InAs/GaAs quantum dots investigated in the second project of this thesis work were grown by the research group of Dennis Deppe at the University of Central Florida. Figure 3.1 shows an atomic force microscopy image of a similar quantum dot sample and a diagram of the layered structure. It consists of a single layer of InAs quantum dots grown on top of a 200 nm layer of GaAs, which was overgrown with another 65 nm of GaAs. These layer are bounded by AlGaAs diffusion barriers. A unique feature of this sample is that it contains a bimodal size distribution of QDs. The PL spectrum, shown in Fig. 3.2(b), has three distinct peaks, one large peak at 1220 nm and two smaller peaks at 1140 nm and 1290 nm. The origin of each of these peaks was determined by the author using PL and PLE experiments. The large peak at 1220 nm and the smaller peak at 1290 nm result from emission from the ground state optical transition from two different populations of QDs. The ground state to excited state transitions are separated by 75 meV for the 1220 nm dots and by 95 meV for the 1290 nm population. The 1140 nm peak in the ensemble PL is therefore the excited state corresponding to the 1220 nm ground state QDs, while the excited state of the 1290 nm QD population is within the 1220 nm peak. These distinct peaks in Fig. 3.2(b) show that the QD ensembles have good size uniformity. The 1220 nm QDs have an areal density of 10^{10} cm^{-2} while the population at 1290 nm has a density of approximately 10^{9} cm^{-2}. These densities were estimated by D. G. Deppe using AFM measurements on a sample grown under similar conditions.

Individual QDs from this sample were isolated using a metallic mask of apertures, which allowed for excitation of a relatively small number of QDs. The gold mask was fabricated

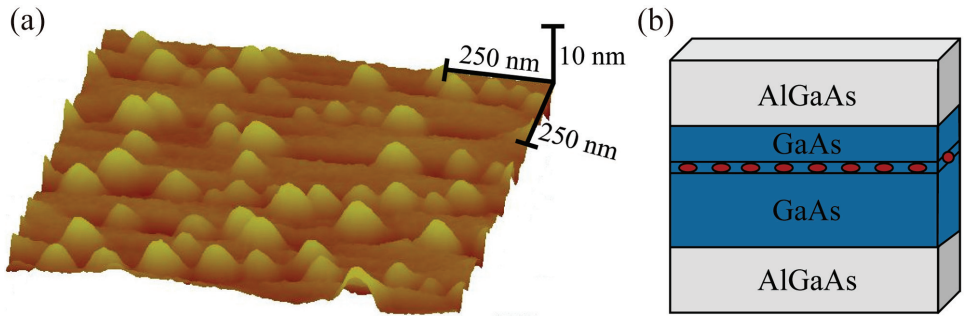

Figure 3.1: Atomic force microscopy image of InAs quantum dot sample. (b) Simplified diagram of layered quantum dot structure.

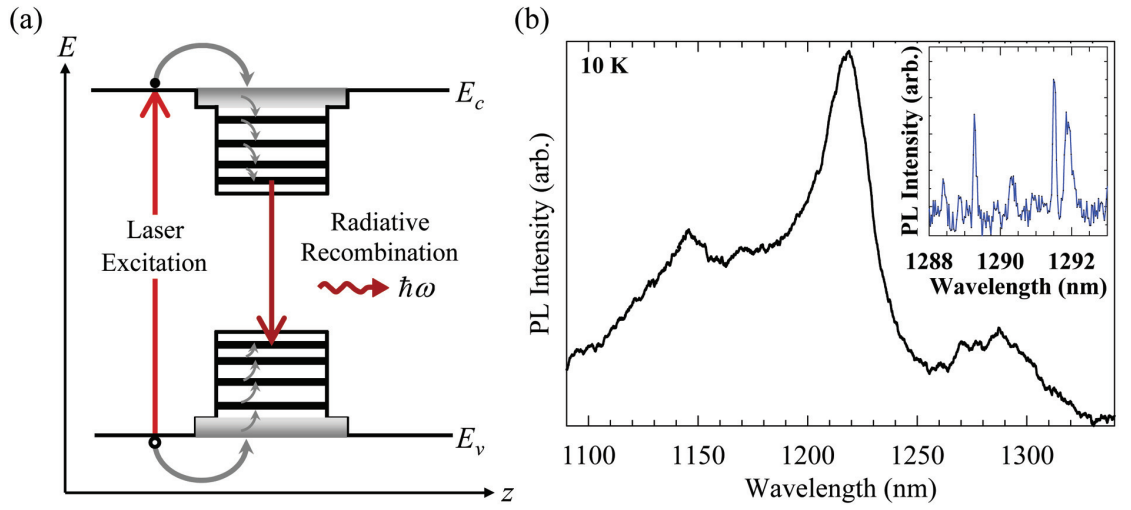

Figure 3.2: (a) Simplified band edge diagram of InAs/GaAs quantum dots. Free carriers in the GaAs are excited and radiatively recombine at discrete energies. (b) Photoluminescence spectrum of the InAs/GaAs quantum dot ensemble grown by the research group of Dennis Deppe. Inset: Single QD PL collected using a mask of apertures and micro-PL apparatus.

by CMC Microsystems using electron beam lithography. This mask was designed by the author to have numerous square sections containing apertures of the same diameter, ranging from 1 μm to 100 nm, and is shown in Fig. 3.3. Micro-PL results, collected through a 0.4 μm aperture, are shown as an inset in Fig. 3.2(b). Within such an aperture, based on the estimated areal density, we expect to see emission from $\sim$12 QDs in the 1220 nm population and $\sim$1 QD in the 1290 nm population; however, micro-PL investigations showed that the areal density of both QD populations is inhomogeneous from aperture to aperture of the same diameter. Emission from the 1220 nm population within a 0.4 μm aperture can vary from $\sim$10 to $\sim$20 QDs, while emission from the 1290 nm QD population can vary from 0 to $\sim$10 QDs. The inset in Fig. 3.2(b) shows a collection of emission peaks from the 1290 nm QD population.

The second QD sample used in this thesis work was grown by the research group of Robin Williams at the National Research Council of Canada using experimental methods that are described in detail in Ref. [31]. This sample contains InAs/InP QDs within a dielectric Bragg stack λ cavity. The high reflectors which form the cavity are high-low index pairs of SiO_2 and Ta_2O_5 forming Bragg stacks on the top and bottom of the semiconductor layer. These were fabricated by depositing the dielectric stack on the surface of a semiconductor wafer containing the QDs, gluing the structure face down on

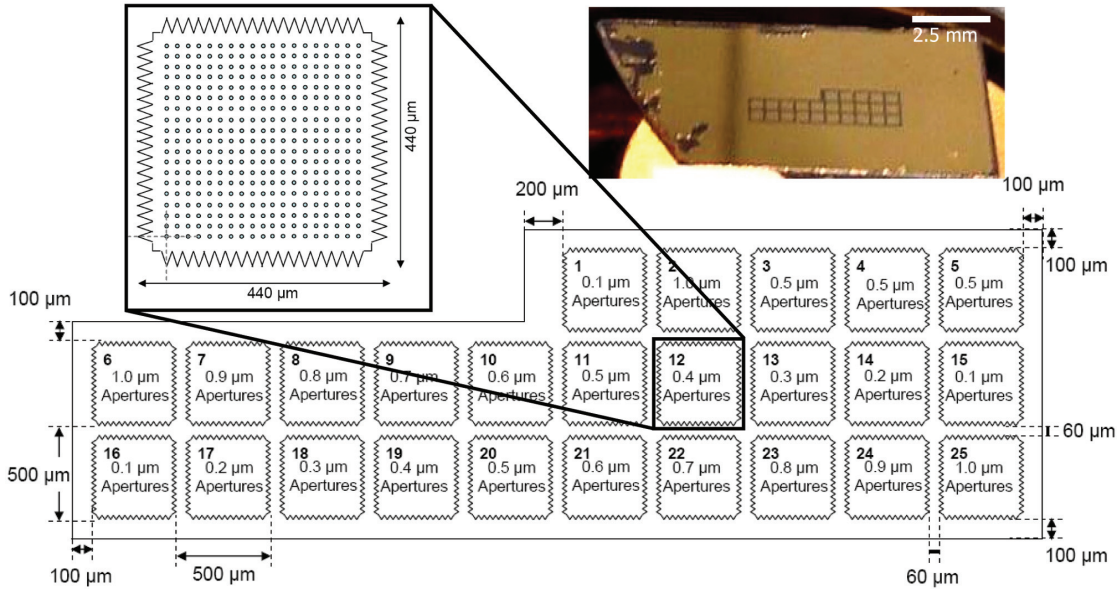

Figure 3.3: Diagram of metallic mask with squares containing equal sized apertures deposited on the QD sample. Inset: Photograph of masked QD wafer.

a glass substrate, removing the substrate by wet etching and depositing a second Bragg stack on the bottom of the semiconductor layer. The QDs within the semiconductor layer were grown by chemical beam epitaxy and have a low areal density of two dots per square micrometer. The sample structure is similar to that shown in Fig. 3.4(a), but with a two times thicker InP spacer layer to result in a λ cavity. This microcavity structure has a transmission resonance that varies in energy with incident angle, as described in Sec. 2.4.2. The experiments described in Chapter 6 exploit this cavity resonance to select different subsets of the full QD ensemble for optical control. Angle-resolved PL data, shown in Fig. 3.4(b), show the energy shift of the cavity mode with angle. The observation of emission for the full range of detection angles indicates the presence of QDs with the ground state optical transition resonant with this mode. The rapid drop in PL emission strength is due primarily to the effect of the optical density of modes in the microcavity, which increases the probability of emission into the normal incidence mode at the expense of emission for non-zero detection angle [32].

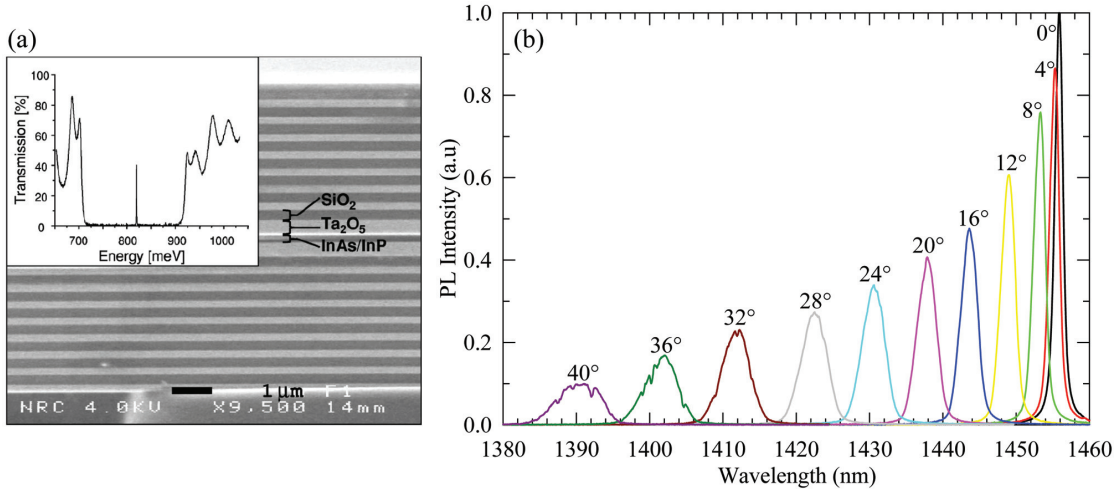

Figure 3.4: (a) Scanning electron micrograph of dielectric cavity structure, adapted from Ref. [31], similar to the sample used in this thesis. (b) PL spectra of the InAs/InP quantum dot ensemble as a function of sample angle. Measured by the author.

3.2 Continuous-Wave Photoluminescence and Photoluminescence Excitation

Continuous-wave photoluminescence (CWPL) investigations utilize the radiative recombination of carriers in self-assembled semiconductor structures to determine the photon energies for allowed optical transitions within the structure. A laser is used to excite free electron-hole pairs into the surrounding bulk material. These carriers then relax into the discrete energy levels of the confined system before recombining and emitting photons, or photoluminescence, at frequencies associated with the allowed transitions. A monochromator is used to spectrally resolve the emitted light. A simplified energy band edge diagram demonstrating the optical excitation and a CWPL spectrum for InAs/GaAs quantum dots is shown in Fig. 3.2(a) and (b).

In a typical CWPL experiment, the spot size of the excitation laser is $\approx$30 μm, leading to excitation of a large number of quantum dots ($\approx 10^5$). If one combines this approach with diffraction-limited light focusing and collection capabilities, the experimental technique is called micro-PL and the emission lines from a single quantum dot can be observed using a high resolution monochromator. In this thesis work, both ensemble and single quantum dot CWPL experiments were carried out.

Photoluminescence Excitation (PLE) measurements, which were carried out under

conditions of diffraction limited focusing, also utilize the radiative recombination of carriers; however, in this case, the laser is used to excite carriers directly into one of the excited state transitions in the QD. In particular, in order to determine the excited states of a QD, the excitation laser is tuned throughout a range of higher energies while detecting the PL from the ground state transition. PL and PLE measurements were performed on individual InAs/GaAs QDs in order to characterize their ground state and excited state optical transition energies. This information was used in the numerical pulse shape optimization involved in the second project of this thesis work.

3.3 Femtosecond Pulse Shaping

Femtosecond pulse shaping techniques allow for the independent control of the amplitude and phase of the frequency components in a femtosecond optical pulse, leading to a customized ultrafast optical waveform. In this thesis, a reflective pulse shaper geometry was used, as shown in Fig. 3.5. The input pulse is spread by a diffraction grating and the spectrum is reflected by a curved mirror. The spectral components pass through a spatial mask in the Fourier plane and are reflected back to the curved mirror and diffraction grating, where the spectrum is recombined into the output pulse. By using a spatial light modulator (SLM) as the mask, one can achieve programmable computer control of the amplitude and/or phase of the output pulse. The SLM used here was purchased from Cambridge Research & Instrumentation Inc. and contains 128 pixels in a dual mask configuration. As described in Sec. 2.3.1, each pixel has an electrically variable index of refraction that can be used to modulate the phase of the incident light. In the case of a dual mask SLM, two liquid crystal arrays are oriented with extraordinary axes at 90° to each other and at 45° relative to the incident light polarization. In combination with an input and output polarizer, this configuration allows the SLM to control the total phase retardation and act as an electrically tunable waveplate for amplitude modulation at each wavelength. This computer controlled approach to femtosecond pulse shaping was utilized in the first and second projects of this thesis, to realize optimized pulse shapes for optimal quantum control experiments.

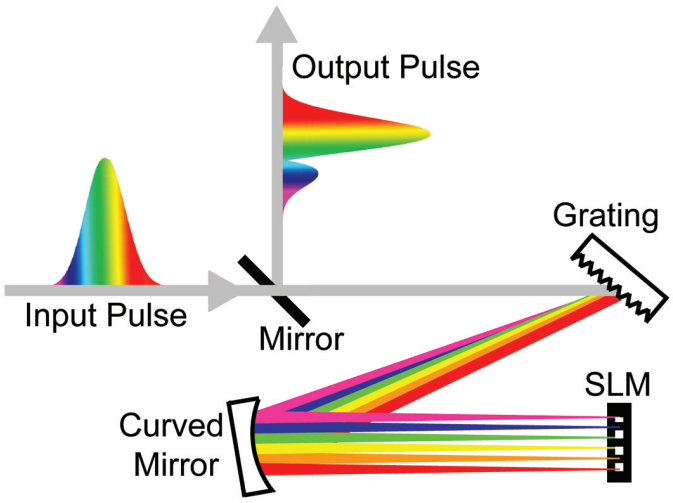

Figure 3.5: Reflective pulse shaper geometry.

3.4 Dispersion Compensation and Pulse Characterization

Dispersion compensation is crucial for the optimal quantum control experiments within this work as the numerically optimized pulse shaping masks are designed to be applied to transform-limited optical pulses. Ultrafast pulses from mode-locked sources are rarely transform-limited and propagation through an optical apparatus can introduce additional phase distortions, leading to an unknown pulse phase at the QD sample. The programmable pulse shaper used for the optical control experiments in this thesis was also used for dispersion compensation using an approach called multiphoton intrapulse interference phase scan (MIIPS) [86]. MIIPS is a single beam pulse characterization technique that utilizes the second harmonic spectrum of the pulse at the sample position (or an equivalent focus) to carry out a measurement of the pulse phase. In particular, the second harmonic spectrum is given by

$$S^{(2)}(2\omega) \propto \left| \int |E(\omega+\Omega)|\,|E(\omega-\Omega)|\, e^{i[\phi(\omega+\Omega)+\phi(\omega-\Omega)]} d\Omega \right|^2, \tag{3.1}$$

where Ω is an integration variable describing frequency components in the pulse. The second harmonic power density at a particular frequency 2ω will be maximum when the phase factor in the integrand in Eq. 3.1 is equal to unity, as would occur for a TL

pulse. To measure the compensation phase required to make the initial pulse transform-limited, the SLM is used to iteratively determine the extra phase at each ω required to maximize the second harmonic power spectrum at 2ω. The extra phase added by the SLM is systematically varied by using a reference function of the form:

$$\xi(\omega, \delta) = \alpha \, cos[\gamma\omega - \delta(\omega)] \tag{3.2}$$

where $\alpha = 2\pi$ in this case, and determines the maximum imposed phase. To determine γ, one first measures the pulse bandwidth using a spectrometer. This bandwidth is then used to calculate the corresponding theoretical TL pulse duration. γ is equal to the inverse of this pulse duration. Using these fixed values of α and γ, δ is then scanned to determine the phase that maximizes the second harmonic power spectrum.

The essential optical components required to perform MIIPS are illustrated in Fig. 3.6(a), including a non-linear βeta Barium Borate (BBO) crystal to create the second harmonic spectrum. In optimal quantum control experiments, the BBO crystal is placed at the sample position. Example MIIPS traces are shown in Fig. 3.6(b) and (c). The contour scale shows the second harmonic intensity as a function of the wavelength and the scanning parameter δ. For TL pulses, Fig. 3.6(b) shows evenly spaced features on the MIIPS trace which all have the same slope [87]. Second and third order phase distortions appear on the MIIPS trace in the form of unevenly spaced features and unequal slopes, respectively (Fig. 3.6(c)). The software which carries-out the MIIPS routine was purchased from Biophotonic Solutions Inc.

In this thesis work, autocorrelation techniques were used to characterize the optical pulses in the quantum control experiments. The pulses were characterized before and after dispersion compensation as well as after the intended optimum shaping mask was applied. From a general perspective, correlation analysis is used to compare two signals to determine their degree of similarity. In the case of an autocorrelation, the laser pulse is compared to itself. This is accomplished by the interference of two copies of the pulse, one at a controllable time delay relative to the other in a non-linear optical crystal (BBO). The second harmonic intensity resulting from the two pulses is measured versus the time delay between the pulses. There are two relevant configurations: (*i*) non-collinear (background-free) autocorrelation; and (*ii*) collinear (or interferometric) autocorrelation. In the former case, the full-width at half maximum of the autocorrelation is proportional to the pulse

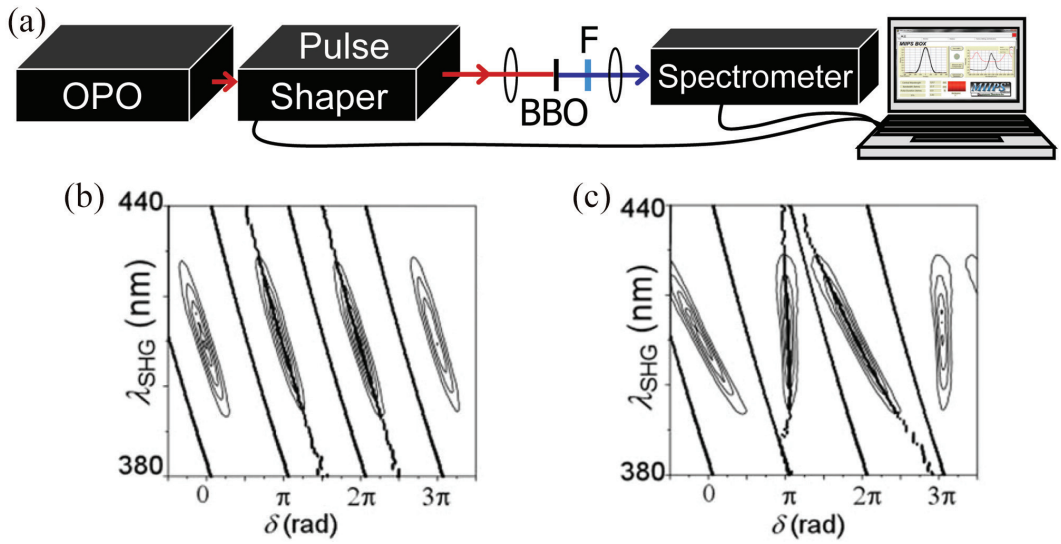

Figure 3.6: MIIPS traces of (a) Schematic diagram of MIIPS pulse characterization and dispersion compensation apparatus. The laser source is an optical parametric oscillator (OPO). Filter F is used to block the fundamental beam. (b) MIIPS trace of TL pulses with optimized MIIPS phase compensation mask and (c) MIIPS trace of ultrafast pulses before dispersion compensation. Adapted from Ref. [87].

duration with a proportionality factor determined by the pulse shape [88]. In the later case, one gains insight into the phase characteristics of the optical pulse. An interferometer was designed and constructed to enable both non-collinear and collinear autocorrelation measurements, and is shown in Fig. 3.7(a). One may convert between the two alignment geometries by removing mirror M3 from the optical path. The autocorrelation is obtained using a rapid scan approach by controlling the length of one of the arms of the interferometer dynamically using a light-weight retroreflector on the cone of a speaker. The speaker is driven by a function generator followed by an amplifier. Background-free autocorrelations before and after dispersion compensation are shown in Fig. 3.7(b) and (d) together with the corresponding interferometric autocorrelations in Fig. 3.7(c) and (e). The pulse durations obtained from these autocorrelations were determined assuming a pulse shape of the form $E_0(t) = |E_0|\mathrm{sech}(1.76t/\tau)$ and are indicated in each case. The raised wings present in Fig. 3.7(c) are characteristic of a chirped pulse. These raised wings are absent in the compensated pulse, as shown in Fig. 3.7(e), indicating that the chirp was removed.

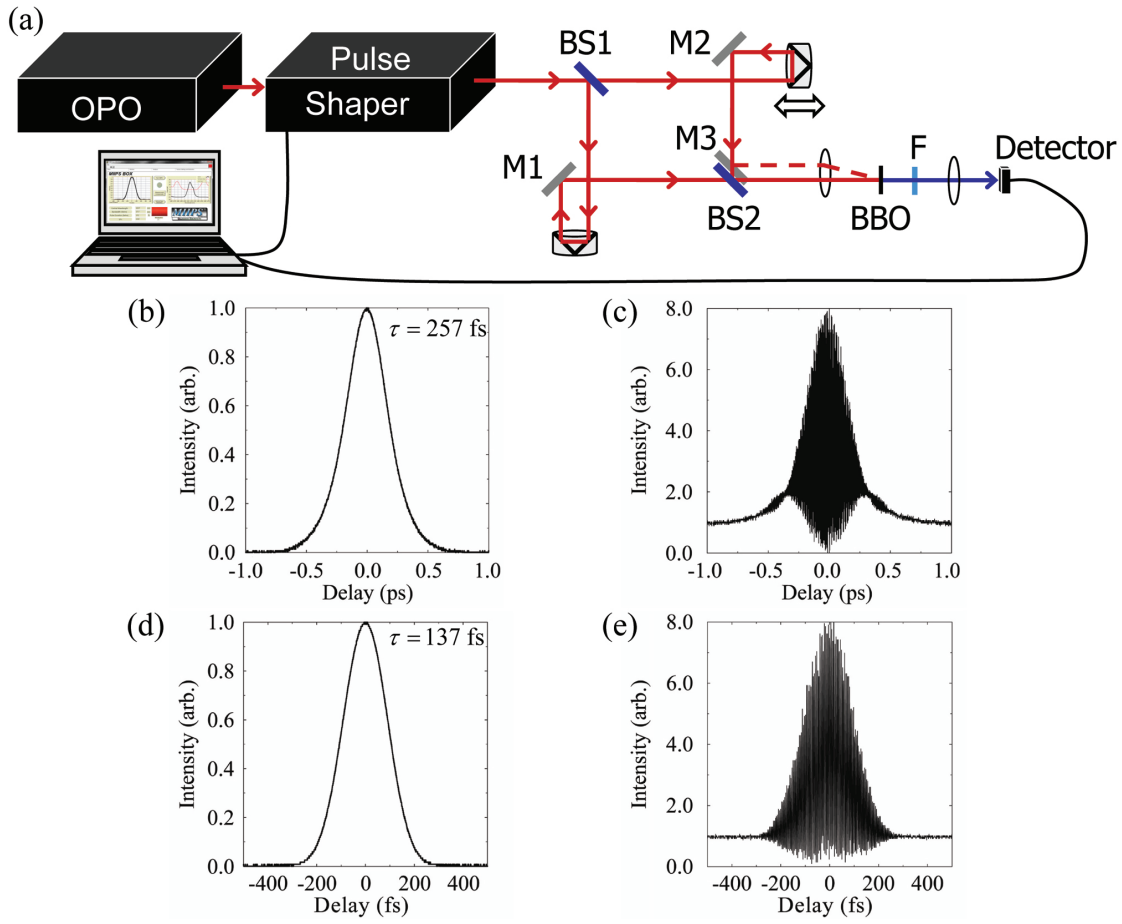

Figure 3.7: (a) Diagram of autocorrelator for laser pulse characterization. Zero-background autocorrelations are measured with mirror M3 in the optical path. The removal of mirror M3 allows for a collinear geometry, used to collect interferometric autocorrelations. The detector is an optical fiber when MIIPS is performed. A photomultiplier tube was used to detect the autocorrelation traces. (b)((d)) Background-free and (c)((e)) interferometric autocorrelation traces from OPO laser source (with applied dispersion compensation). The raised wings in (c) are characteristic of an interferometric autocorrelation of a chirped laser pulse.

3.5 Optical Control Experiments

In this thesis work, a quantum control apparatus was designed, constructed and implemented in the quantum control of the excitonic states of QDs with ground state transition energies in the telecom frequency band. In these experiments, the objective is to tailor the quantum state dynamics of excitons using pulse shaping. Excitation is carried out on the first excited state transition, and the steady-state PL on the ground state transition is

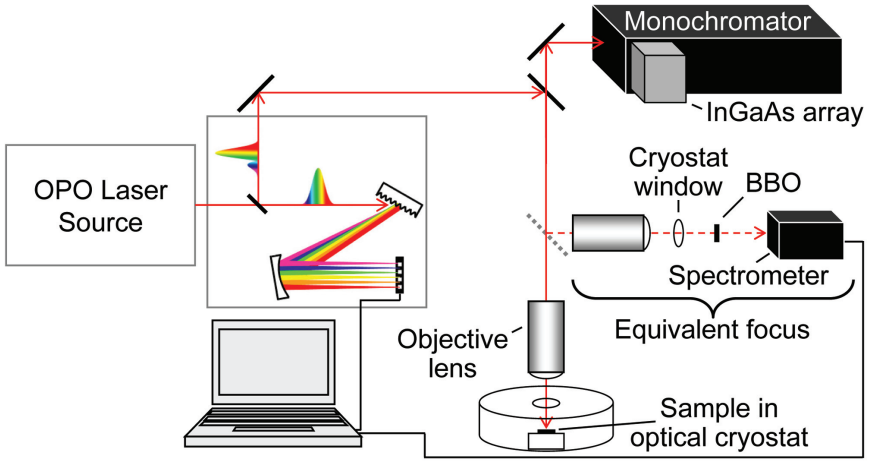

Figure 3.8: Schematic diagram of quantum control apparatus, including pulse shaper, monochromator and InGaAs array detector.

used to read out the quantum state at the end of the laser pulse. A schematic diagram of the complete quantum control apparatus used in these experiments is shown in Fig. 3.8 and photographs of the setup are shown in Fig. 3.9. The excitation laser beam is focused onto the QD sample through an objective lens and ultra-thin cryostat window. The objective lens is a Mitutoyo 100× high numerical aperture (NA=0.7) microscope objective designed to operate at infrared wavelengths. The QD sample is mounted on an attocube three-dimensional nanopositioning stage at 10 K in a continuous flow microscopy cryostat (Janis Research ST-500). The second harmonic spectrum required for dispersion compensation using MIIPS is detected at an equivalent focus. Figure 3.8 illustrates this region, equivalent to the optical path used to access the QD sample; however, a BBO second harmonic crystal is placed at the sample position in this case. This equivalent focal path includes the same microscope objective lens and ultra-thin cryostat window used in the QD excitation line (Fig. 3.9(b)). The dispersion compensation phase, determined using MIIPS, was then added to the numerically optimized control pulse shape for each project. The PL from the ground state was collected using a 0.75 m monochromator (Princeton Instruments) and InGaAs liquid nitrogen cooled array detector (from HORIBA Jobin Yvon). A long-pass filter placed in front of the monochromator was used to minimize the detection of the scattered pump laser light.

The excitation laser spot size was determined using a blade-edge type measurement. Using the attocube nanopositioners, the focused laser spot was stepped off of a straight

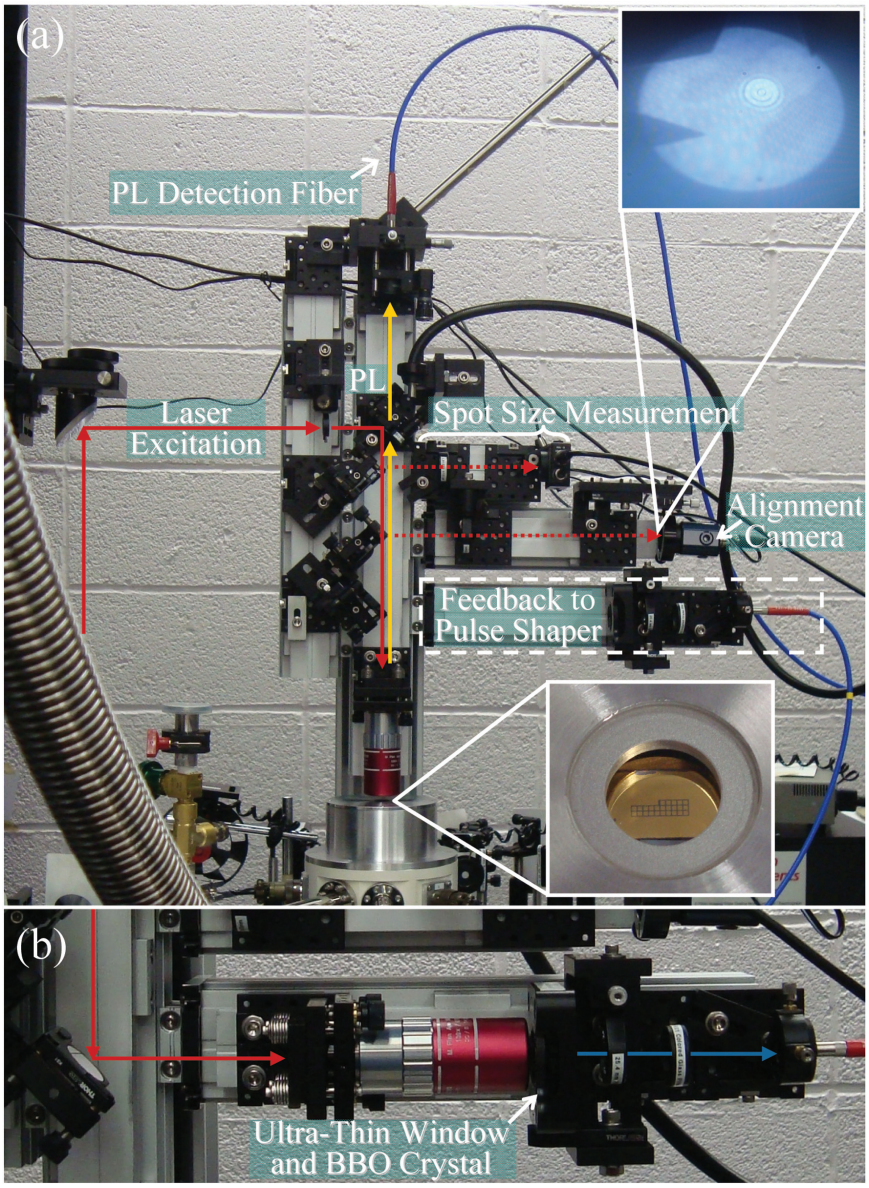

Figure 3.9: Photograph of a section of the quantum control apparatus with extra components. (a) The objective lens is placed above the microscopy cryostat window for QD excitation and PL detection. Two pellicle beam splitters and one mirror, each on flip mounts, allow for access to the three arms of the structure: for laser spot size measurement, alignment of the laser to the mask of apertures, and an equivalent focus which duplicates the optical path to the the QD sample. The masked QD sample within the optical cryostat as well as the image captured by the alignment camera, of the mask of apertures and the focused laser spot, are inset. (b) Equivalent focus arm providing feedback to pulse shaper.

edge present on the metallic mask deposited on the QD sample (Sec. 3.1). The change in the intensity of the reflected beam was detected using a single channel InGaAs detector.

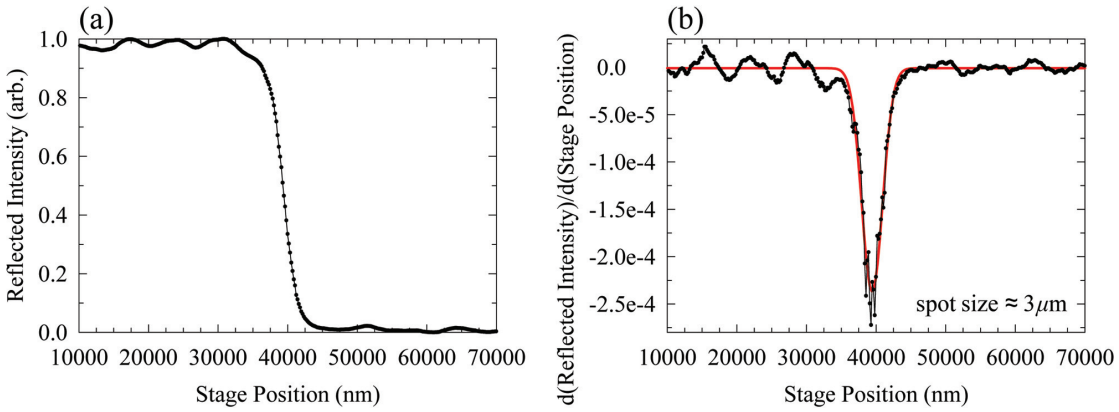

Figure 3.10: (a) Example of reflected intensity data, from metallic mask step edge. (b) Differentiated data from (a), fit to a Gaussian peak.

An example of the collected reflected intensity data is shown in Fig. 3.10(a). This data was then numerically differentiated and fit to a Gaussian peak (Fig. 3.10(b)), allowing for the radius of the focused laser spot to be determined. The portion of the apparatus used to measure the spot size is shown in Fig. 3.9(a).

For the experiments in Chapter 4, the shaped pulses were characterized to verify accurate pulse shape control within the apparatus. This included calculations of the autocorrelations and MIIPS traces using a software package called femtoPulse Master which was purchased from Biophotonic Solutions Inc. For the experiments in Chapter 5, the pulse shapes were applied to quantum control of two excitons in two different QDs. The quantum state dynamics for the optimal quantum control experiments were calculated using the optical Bloch equations, discussed in Sec. 2.3, incorporating the experimentally measured values of the exciton transition energies and dipole moments in each QD. The exciton transition energies were measured using PLE experiments, which were performed using the same quantum control apparatus. In this case, the excitation laser was the optical parametric oscillator (OPO) laser source. The ground state PL emission was detected using the monochromator and InGaAs array. In order to determine the dipole moments of the QDs, Rabi rotations were performed by resonantly exciting the first excited state transition of each QD with a TL femtosecond pulse and varying the pulse area by increasing the excitation power at the sample. The fit to these oscillations, in addition to laser spot size measurements, were used to extract the dipole moments for each QD.

3.6 Pump-Probe Spectroscopy

Time-dependent phenomena in semiconductor quantum dots can be characterized using an ultrafast spectroscopy technique called pump-probe. In this case, time resolution is achieved by splitting a laser pulse in two and delaying one copy of the pulse with respect to the other. The pump is the first copy of the pulse which excites the sample. The probe pulse is much weaker than the pump ($\geq$ 10 times weaker) so that the probe does not cause significant excitation in the sample in comparison to the pump pulse. The probe pulse is used to detect some optical property (*e.g.*, transmissivity or Faraday rotation) that is modified as a result of the excitation created by the pump pulse. The probe pulse arrives at a later time, determined by the difference in path lengths of the two pulses. The path difference between the two pulses can be adjusted, allowing the relaxation of the system of electron-hole pairs to be observed in the time domain. There are a variety of configurations for a pump-probe experiment, determined by: (*i*) what characteristic is measured (for example transmissivity); (*ii*) whether the pump and probe beam are collinear or non-collinear; and (*iii*) whether they have been derived from the same laser pulse (referred to as a degenerate experiment) or pulses with different center wavelengths using different output beams from an ultrafast laser system (a non-degenerate experiment). In this thesis work, degenerate pump and probe pulses were used in a configuration referred to as differential transmission, which measures the pump induced change in transmissivity. This technique is described in detail in the next section. Figure 3.11(a) shows a basic schematic diagram of a pump-probe experiment.

3.6.1 Differential Transmission

Differential transmission experiments were used in the third project of this thesis to measure the carrier lifetime of InAs/InP QDs as well as to investigate the ability to spectrally select QD subsets using angle-dependent pump-probe measurements. In a differential transmission experiment, one detects the pump-induced change in the transmissivity of the sample. The electron hole pairs injected by the pump pulse reduce the absorption on optical transitions for which either the valence state or conduction state is occupied. This effect is called state filling, and the associated reduction in absorption is commonly referred to as bleaching. In the experiment, the transmission is increased by the reduced absorption, resulting in a positive differential transmission signal. As described in Sec. 2.2,

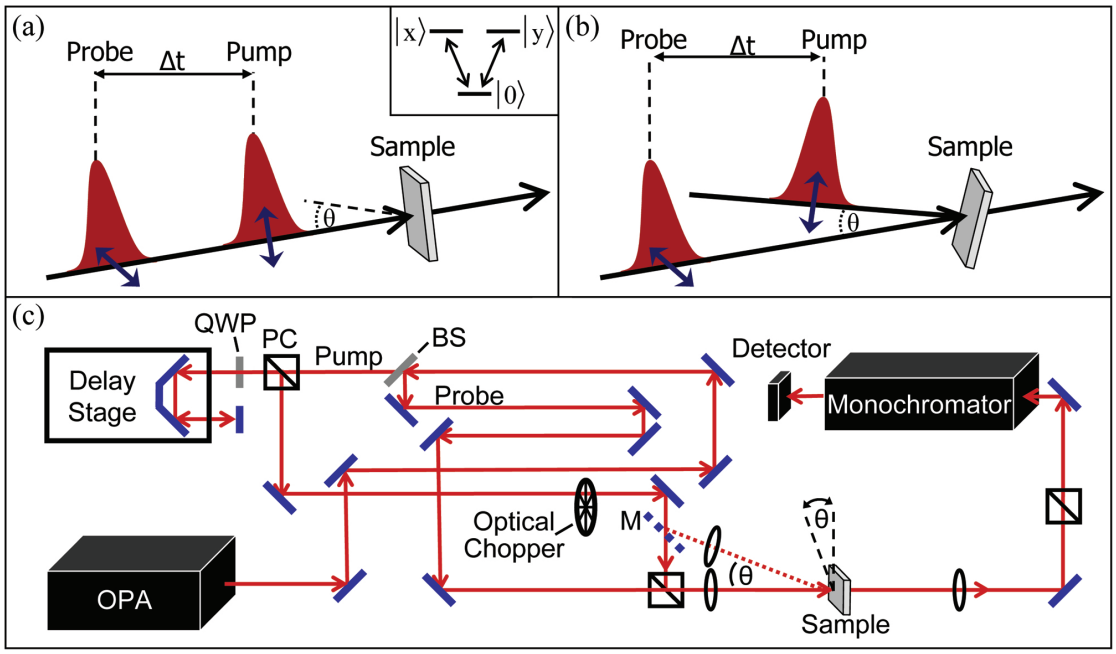

Figure 3.11: (a) Schematic representation of a pump-probe experiment shown in collinear differential transmission geometry. Δt is the variable optical delay between the pump and probe pulses. Inset: InAs QD energy level diagram with polarized excited state selection. (b) Schematic representation of differential transmission experiment in non-collinear geometry. The pump beam is at normal incidence and the probe beam is incident at angle θ to the sample. (c) Diagram of pump-probe experiment set-up using IR OPA laser source. The collinear excitation geometry is achieved when mirror M is removed.

the optical transitions excited by the pump pulse depend on its polarization. If the pump pulse is linearly polarized, equal populations of spin-up and spin-down carriers are injected and contribute equally to the bleaching signal. The decay of this signal with increasing probe delay provides a measurement of the recombination time of the electrons and holes.

The schematic diagram of the pump-probe apparatus used in the the third component of this thesis work is shown in Fig 3.11 (c). A beam splitter with a ratio of approximately 95:5 is used to split the laser beam into pump and probe beams. A retroreflector mounted on a motorized delay stage with a minimum step size of 0.1 μm and a full range of 40 cm is used to introduce a variable path length difference between the pump and probe pulses. A double pass configuration was used, in which a quarter-wave plate is placed in front of the retroreflector and the retroreflected beam is sent back onto the same path using a planar mirror at normal incidence. This doubles the total accessible path length and results in pump and probe beams with orthogonal linear polarizations. This aids in the rejection

of scattered pump light and allows the two beams to be made collinear using a polarizing beam splitter cube (PC) as shown in Fig. 3.11(c). The appropriate selection rules for the QDs are shown as an inset in Fig. 3.11(a). By probing on the $|0\rangle$ to $|\mathrm{y}\rangle$ transition, we can detect a bleaching signal associated with the excitation of the $|0\rangle$ to $|\mathrm{x}\rangle$ transition. The two beams are then focused onto the same spot on the sample (approximately 90 μm in diameter). The probe beam is spectrally resolved using a 0.25 m monochromator and detected using an InGaAs photodiode. In order to reject scattered pump light, the probe beam was passed through a polarizer placed in front of the monochromator. The probe transmission in the absence of the pump pulse (T_0) is measured by chopping the probe beam using a mechanical chopper and detecting the amount of transmitted light through the sample at each wavelength using a lock-in amplifier. This process is then repeated with the sample removed. T_0 is then determined as the ratio of the resulting spectra. After removing the sample, the alignment into the monochromator and detector is carefully re-optimized to account for beam steering by the sample substrate. The pump induced change in transmission ($\Delta T \equiv T - T_0$) is then measured by moving the mechanical chopper into the pump beam path and detecting the component of the probe detector signal at the chopper frequency using a lock-in amplifier.

The experiments described in Chapter 6 involve the application of pump-probe differential transmission techniques on the one-dimensional microcavity structure described in Sec. 3.1. In these experiments, the differential transmission signal is compared for collinear and non-collinear excitation geometries. In Fig. 3.11(c), the mirror M in the pump beam path is used to switch between these geometries. A polarizing beamsplitter cube is used to combine the pump and probe beams in the collinear case. Another cube is placed in front of the monochromator to isolate the probe beam for detection.

CHAPTER 4

OPTICALLY ENGINEERED ULTRAFAST PULSES FOR CONTROLLED ROTATIONS OF EXCITON QUBITS IN SEMICONDUCTOR QUANTUM DOTS

Authors: Angela Gamouras, Reuble Mathew, and Kimberley C. Hall

Department of Physics and Atmospheric Science, Dalhousie University, Halifax, Nova Scotia B3H4R2, Canada

Reprinted with permission from Journal of Applied Physics **112**, 014313, Angela Gamouras, Reuble Mathew, and Kimberley C. Hall, "Optically Engineered Ultrafast Pulses for Controlled Rotations of Exciton Qubits in Semiconductor Quantum Dots". Copyright 2012, American Institute of Physics. Angela Gamouras developed the techniques, performed the experiments and data analysis. Reuble Mathew carried out the theoretical analysis and numerical modeling. Kimberley C. Hall conceived and designed the experiments. Angela Gamouras and Kimberley C. Hall wrote the manuscript with input from all authors.

4.1 Abstract

Shaped ultrafast pulses designed for controlled-rotation (C-ROT) operations on exciton qubits in semiconductor quantum dots are demonstrated using a quantum control apparatus operating at $\sim$1 eV. Optimum pulse shapes employing amplitude and phase shaping

protocols are implemented using the output of an optical parametric oscillator and a programmable pulse shaping system and characterized using autocorrelation and multiphoton intrapulse interference phase scan (MIIPS) techniques. We apply our pulse characterization results and density matrix simulations to assess the fundamental limits on the fidelity of the C-ROT operation, providing a benchmark for the evaluation of sources of noise in other quantum control experiments. Our results indicate the effectiveness of pulse shaping techniques for achieving high fidelity quantum operations in quantum dots with a gate time below 1 ps.

4.2 Introduction

Semiconductor quantum dots (QDs) are strong candidates for future solid state quantum computing architectures, in which the fundamental qubits may be realized using the quantum states of excitons or individual carrier spins [19, 20, 21, 22, 23, 25, 26, 89, 90, 91, 92, 93, 94]. Such an approach offers the promise of long term scalability through rapid advances in semiconductor growth and fabrication techniques, including tailored coupling via optical microcavity and waveguide modes [20, 26, 93], as well as ease of integration with conventional computing technology. The possibility of manipulating the fundamental quantum states using optical techniques would exploit established photonic technologies, and may lead to THz operation rates. This potential has led to an intensive research effort in recent years dedicated to the pursuit of coherent optical control of quantum states in semiconductor quantum dots, including demonstrations of single qubit rotations involving excitons and single carrier spins [42, 43, 44, 45, 49, 50, 52, 54, 57], entanglement [28, 95, 96], adiabatic passage [30, 51], and quantum state tomography [80].

Femtosecond pulse shaping techniques provide independent control of the temporal characteristics of the phase and amplitude of an optical pulse [81], providing a means to tailor the light-matter interaction responsible for quantum control. The benefits of pulse shaping have been realized, for example, in the control of atomic and molecular systems [65, 66, 67, 68, 69] and chemical reactions [70, 71]. It has recently been shown theoretically that the application of pulse shaping techniques to optically-controlled quantum operations in semiconductor quantum dots can lead to substantial improvements in performance metrics such as gate fidelity and speed [22, 23, 83]. For these studies, the pulse shaping method was applied to the controlled-rotation (C-ROT) operation involving

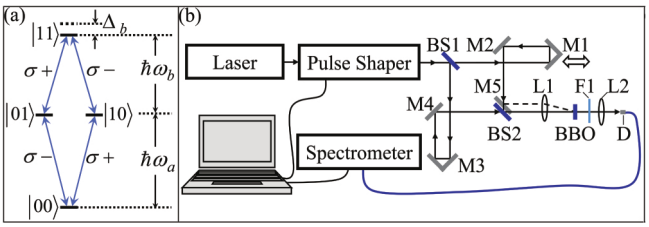

Figure 4.1: (a) Energy level diagram showing excitonic transitions in semiconductor quantum dots with cylindrical symmetry. The system ground state (no excitons) is $|00\rangle$. Opposite circularly-polarized light (represented by σ_+ and σ_-) leads to the generation of excitons with opposite spin ($|01\rangle$ and $|10\rangle$). The biexciton state $|11\rangle$ consists of two excitons of opposite spin, with biexciton binding energy Δ_b. (b) Schematic diagram of the portion of the quantum control apparatus used to generate and characterize the pulse shaping protocols. Femtosecond pulses from the laser enter the pulse shaper where amplitude or phase masks are implemented on TL pulses. The shaped pulses enter the interferometric/non-collinear autocorrelator. Mirror M1 is mounted on a speaker driven by a function generator, providing a rapid scan delay line. The retroreflected beam is focused using lens L1 into a BBO crystal for second harmonic generation. Mirror M5 (beamsplitter BS2) is used for noncollinear (interferometric) autocorrelation measurements. Filter F1 removes any remaining IR components. Detector D is a photomultiplier tube used to collect autocorrelation traces or an optical fiber input connected to a spectrometer, providing feedback to the pulse shaper.

exciton qubits, representing a useful prototype for the general application of shaping techniques to optical control of charge and spin states in semiconductor quantum dots. The C-ROT operation is achieved using a four-level system consisting of the vacuum ground state $|00\rangle$, two exciton states $|01\rangle$ and $|10\rangle$, and the biexciton state $|11\rangle$ within a single self-assembled semiconductor QD (Fig. 4.1(a)). Two qubits are represented by the single exciton states $|10\rangle$ and $|01\rangle$ and the C-ROT operation is performed by implementing a π rotation on the first (target) qubit if and only if the second (control) qubit is in state 1. For the successful experimental implementation of optical control schemes employing pulse shaping techniques, it is essential that the quantum control system be well characterized using convenient, real-time pulse measurement tools.

Here we report the experimental demonstration of the pulse shaping protocols found in Ref. [83] for C-ROT operations in quantum dots using a quantum control apparatus operating in the infrared spectral region ($\sim$1 eV, aimed at quantum dots with emission wavelengths in the 1.3 μm telecom band), in contrast to existing quantum control demonstrations in the visible and near infrared [65, 66, 67, 68, 69, 70, 71]. This apparatus is also used to assess the experimental limitations on gate fidelity due to inaccuracies in the

pulse shaping system and other laser instabilities, indicating the feasibility of high fidelity ($\sim$0.99) quantum operations with a gate time below 1 ps with the implementation of pulse shaping. These findings thereby provide a useful benchmark in assessing noise limitations in more general quantum control applications using shaped optical pulses. In this work, the theoretical simulations in Ref. [83] are also extended to the application of shaping protocols to C-ROT operations on quantum dots of cylindrical symmetry, for which the exciton states are spin polarized, illustrating the universality of our approach. The pulse shapes were characterized using interferometric and noncollinear (zero-background) autocorrelation techniques as well as multiphoton intrapulse interference phase scan (MIIPS) [86, 87]. We find that the MIIPS trace exhibits unique visual signatures that would greatly aid in the implementation of real-time quantum control experiments. Our results lay the foundation required for the experimental implementation of general phase and amplitude pulse shaping protocols for application to a variety of quantum processes in semiconductor quantum dots, including Rabi rotations [97], adiabatic passage [30, 51, 98], and schemes for dynamical decoupling [27, 99, 100].

4.3 Numerical Pulse Shape Optimization for Controlled Rotations

The interaction between the four-level system in Fig. 4.1(a) and the applied laser field is described by the Hamiltonian $H_{\rm int} = -\vec{\mu}\cdot\vec{E}(t)$, where $\vec{E}(t) = \frac{1}{2}\hat{\epsilon}E_0(t)[\exp(-i\omega\, t - i\phi(t)) + \exp(i\omega\, t + i\phi(t))]$ is the electric field of the pulse and $\vec{\mu}$ is the electric dipole moment operator. Femtosecond pulse shaping systems, which are readily available from a variety of commercial sources [101], provide independent control over the temporal (or equivalently spectral) characteristics of the amplitude $E_0(t)$ and phase $\phi(t)$ of the laser pulse. This ability to finely tune the optical field provides a flexible tool for manipulating the quantum control Hamiltonian $H_{\rm int}$. In this work, we focus on a typical 4-f pulse shaper configuration [81], in which the pulse characteristics are manipulated in the spectral domain using a mask $M(\omega)$ placed in the Fourier plane. The Fourier transform of an ultrafast pulse exiting the pulse shaping system is given by

$$\tilde{E}_{\rm out}(\omega) = \tilde{E}_{\rm in}(\omega)\, M(\omega) \tag{4.1}$$

where $\tilde{E}_{\rm in}(\omega)$ is the Fourier transform of the transform-limited (TL) input pulse, for which $\phi = 0$ and $E_0(t) = |E_0|\mathrm{sech}(1.76t/\tau)$, with $\tau = 130\,\mathrm{fs}$. The mask function $M(\omega)$ is imposed using a spatial light modulator (SLM) and has the general form:

$$M(\omega) = A_M(\omega)\exp\left[i\Phi_M(\omega)\right]. \tag{4.2}$$

Dual mask SLMs provide independent control of $A_M(\omega)$ and $\Phi_M(\omega)$. In this work, we apply the phase-only and amplitude-only shaping protocols developed in Ref. [83] to the C-ROT operation on spin-polarized exciton qubits, as depicted in Fig. 4.1(a). Circularly-polarized selection rules (and degenerate $|01\rangle$ and $|10\rangle$ single exciton states) occur in cylindrically-symmetric quantum dots. The corresponding level scheme for excitons and biexcitons in elongated quantum dots exhibiting linearly-polarized optical selection rules and a nonzero exchange splitting δ between the single exciton states (typically $\sim$100 μeV) was considered in Ref. [83]. The exciton dipole moment, the ground state exciton energy, and the biexciton binding energy were chosen to reflect typical values measured in experiments [102, 103]. The amplitude-only shaping mask is given by

$$\begin{aligned} A_M(\omega) = \Bigg| \exp\left[-\left(\frac{\omega-\omega_b}{\Delta\omega_1/\left(2\ln 2\right)^{1/2}}\right)^2\right] \\ - A_0\exp\left[-\left(\frac{\omega-\omega_a}{\Delta\omega_2/\left(2\ln 2\right)^{1/2}}\right)^2\right]\Bigg| \end{aligned} \tag{4.3}$$

where $E_a = \hbar\omega_a$ and $E_b = \hbar\omega_b$ are the transition energies from $|00\rangle$ to $|10\rangle$ and from $|01\rangle$ to $|11\rangle$, $\Delta\omega_1$ and $\Delta\omega_2$ are the Gaussian function bandwidths and A_0 is an amplitude factor. In this case, $\Phi_M(\omega)$ from Eq. 4.2 is set to zero for simplicity. The phase-only shaping mask is given by

$$\Phi_M(\omega) = \alpha\cos\left[\gamma\left(\omega-\omega_b\right)-\varphi\right]. \tag{4.4}$$

The fidelity of the C-ROT operation was maximized by varying $\Delta\omega_1$, $\Delta\omega_2$, A_0 (amplitude shaping scheme) or α, γ, and φ (phase shaping scheme) as well as the pulse area $\Theta = (\mu\cdot\hat{\epsilon}/\hbar)\int_{-\infty}^{+\infty}E_0(t)\,dt$. The constraints on the free parameters are the same as in Ref. [83] except that the initial TL pulse duration is taken to be 130 fs (corresponding to the full-width-at-half-maximum (FWHM) of the experimental pulses) and Θ was allowed to vary

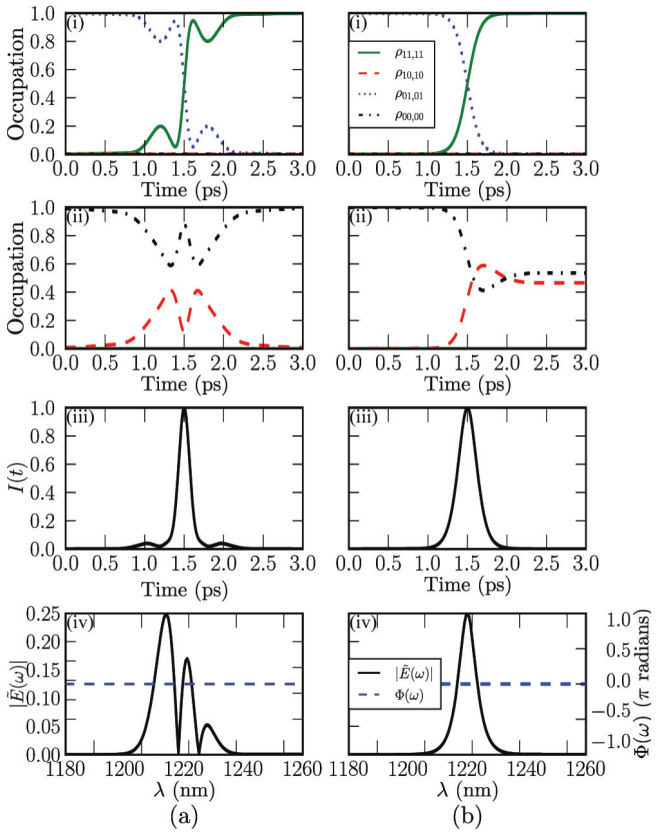

Figure 4.2: Occupation dynamics and pulse characteristics for: (a) the optimum amplitude-shaped control pulse and (b) the TL pulse with equivalent gate time (Δ_b = 2.5 meV). Panels (i) and (ii) indicate the state dynamics for initial occupation in $|01\rangle$ and $|00\rangle$, respectively. Only transitions coupled to the laser field are shown. Panels (iii) and (iv) show the temporal and spectral characteristics of the optical pulses.

up to 8π radians, reflecting experimentally accessible values [104]. The chosen constraints ensure that $A_M(\omega)$ and $\Phi_M(\omega)$ are sufficiently slowly varying to be implemented with high accuracy on a standard 128 pixel SLM. Only the fidelity associated with the C-ROT gate is considered here: a fidelity of unity tied to quantum state initialization is assumed. The quantum state dynamics are calculated using the rotating-wave approximation. Details of the numerical optimization routine are provided in Ref. [83].

The results of simulations of the C-ROT gate are shown in Fig. 4.2(a) and Fig. 4.3(a) for the optimum amplitude-shaped and phase-shaped pulses, respectively. In each case, the gate performance is compared to that for an unshaped (TL) pulse with an equivalent gate time [105]. The shaped pulses substantially outperform the unshaped pulses for both phase and amplitude shaping protocols, leading to the intended final system state for initial

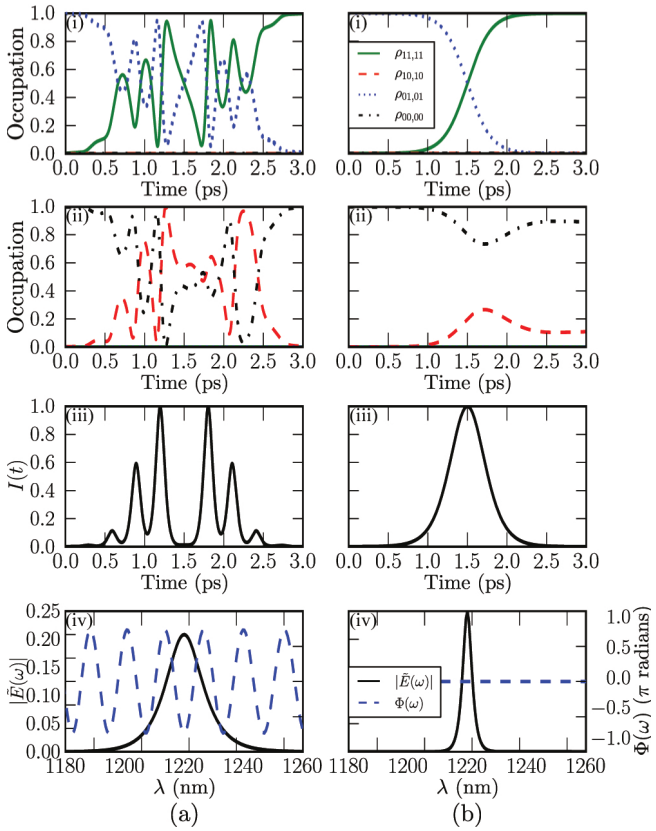

Figure 4.3: Occupation dynamics and pulse characteristics for: (a) the optimum phase-shaped control pulse and (b) the TL pulse with equivalent gate time ($\Delta_b = 2.5$ meV). Panels (i) and (ii) indicate the state dynamics for initial occupation in $|01\rangle$ and $|00\rangle$, respectively. Only transitions coupled to the laser field are shown. Panels (iii) and (iv) show the temporal and spectral characteristics of the optical pulses.

conditions corresponding to unity occupation of each of the four basis states. In contrast, for the TL pulses there is an undesired change in the system state at the end of the pulse when the system is initially in $|00\rangle$ or $|10\rangle$. The shaped pulses therefore provide a much higher gate fidelity, corresponding to 0.999995 (amplitude-shaped pulse) and 0.999998 (phase-shaped pulse). The fidelities for the unshaped pulses are much lower (0.767445 and 0.944764 for the results in Fig. 4.2(b) and Fig. 4.3(b), respectively). The inclusion of relaxation using measured recombination and dephasing times in similar quantum dots [37] reduces our calculated fidelities by ≤ 0.004, reflecting a key advantage of the subpicosecond gate times considered here. The poor performance of the TL pulses is due to the lack of spectral selectivity between the $|00\rangle$ to $|10\rangle$ and $|01\rangle$ to $|11\rangle$ optical transitions, which are both strongly driven (in phase) by separate spectral components

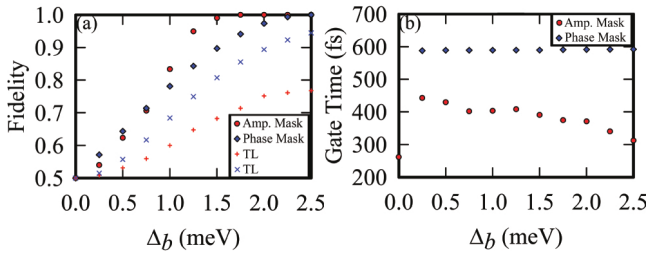

Figure 4.4: (a) Gate fidelity of optimal phase-shaped (diamond), amplitude-shaped (circle), and TL pulses with equivalent gate times for both phase ($\times$) and amplitude ($+$) cases as a function of biexciton binding energy. (b) Gate time of optimized phase-shaped (diamond) and amplitude-shaped (circle) pulses as a function of biexciton binding energy.

within the bandwidth of the optical pulse. In contrast, engineering the control Hamiltonian using pulse shaping allows one to tailor the evolution of the quantum state of the system. In this case, transient dynamics can occur during the laser pulse, but the desired system state is attained at the end of the quantum operation.

Figure 4.4(a) shows the variation of gate fidelity with biexciton binding energy (Δ_b). The fidelity increases with Δ_b in all cases, reflecting the relaxed constraints on the C-ROT performance due to the increasing energy difference between the $|00\rangle$ to $|10\rangle$ and $|01\rangle$ to $|11\rangle$ optical transitions. The fidelities saturate close to unity for both shaping schemes for $\Delta_b > 2.5$ meV, although the amplitude-shaped pulses provide higher fidelities for Δ_b between 1.0 meV and 2.0 meV. The gate times for the optimized pulses are shown in Fig. 4.4(b). The operation times for the phase shaping protocol are up to 50 % longer

Table 4.1: Optimum pulse parameters, including operation gate time (GT), obtained for the amplitude shaping protocol for a range of biexciton binding energies.

Δ_b (meV)	F	$\hbar\Delta\omega_1$ (meV)	$\hbar\Delta\omega_2$ (meV)	A_0	Θ (π rad)	GT (fs)
0.00	0.500	9.921	12.463	0.387	1.531	261.7
0.25	0.539	6.188	6.426	0.902	7.930	442.6
0.50	0.623	6.083	6.877	0.915	8.000	429.5
0.75	0.706	6.083	7.158	0.921	8.000	401.8
1.00	0.833	6.083	7.550	0.947	8.000	403.2
1.25	0.949	6.083	7.928	0.937	8.000	407.9
1.50	0.990	6.083	8.118	0.941	8.000	390.5
1.75	0.999	6.408	8.830	0.939	7.995	374.6
2.00	1.000	6.086	9.209	0.908	6.231	370.9
2.25	1.000	6.741	10.555	0.904	6.185	340.0
2.50	1.000	7.475	12.068	0.903	6.410	312.3

Table 4.2: Optimum pulse parameters, including operation gate time (GT), obtained for the phase shaping protocol for a range of biexciton binding energies.

Δ_b (meV)	F	α (π rad)	γ (fs)	φ (π rad)	Θ (π rad)	GT (fs)
0.00	0.500	1.000	303.8	1.000	3.471	773.5
0.25	0.571	0.737	304.3	-0.109	4.227	588.1
0.50	0.643	0.737	304.3	-0.100	4.233	589.1
0.75	0.714	0.736	304.3	-0.087	4.241	589.2
1.00	0.781	0.736	304.3	-0.075	4.242	589.4
1.25	0.843	0.735	304.3	-0.062	4.228	589.6
1.50	0.897	0.734	304.3	-0.050	4.223	589.6
1.75	0.941	0.734	304.3	0.962	4.219	590.7
2.00	0.974	0.734	304.3	-0.025	4.209	591.2
2.25	0.994	0.734	304.3	0.987	4.198	591.8
2.50	1.000	0.734	303.3	-1.000	4.185	592.0

than the gate times for the amplitude-shaped pulses, reflecting the complex shape of the temporal envelope associated with the simple phase-shaping mask function used here. Summaries of the optimized amplitude and phase mask parameters are given in Table 4.1 and Table 4.2, respectively.

4.4 Experimental Implementation of Optimized Pulse Shapes

4.4.1 Quantum Control Apparatus

Previous work in quantum control has involved optical sources and experiments in the visible or near-infrared spectral region [65, 66, 67, 68, 69, 70, 71]. As a result, the majority of development efforts for pulse shaping systems and pulse characterization equipment have been focused on this wavelength range. Self-assembled In(Ga)As quantum dots offer considerable flexibility for quantum computing applications due to the ability to fabricate ordered quantum dot arrays and composite microstructures [17, 106]. The ground state optical transition in these quantum dots typically occurs in the range 0.8-1.1 eV [31, 102, 103, 107]. The implementation of optically-controlled quantum gates on exciton or spin states in these quantum dots therefore necessitates the development of a quantum control apparatus and suitable characterization tools operating in the infrared. A schematic diagram of the portion of the quantum control apparatus used for implementing

the amplitude and phase shaping protocols and characterizing the resulting pulse shapes is shown in Fig. 4.1(b). The optical source is an optical parametric oscillator (OPO) that is synchronously-pumped by a mode-locked Ti:Sapphire oscillator. The center wavelength of the OPO pulses was tuned to the $|01\rangle$ to $|11\rangle$ transition. The ground state optical transition ($|00\rangle$ to $|10\rangle$) occurs at 1215 nm [102]. The biexciton binding energy was allowed to vary, as in the theoretical calculations. The programmable pulse shaping system utilizes a 128 pixel dual-mask SLM in the Fourier plane to apply amplitude or phase masks to the incident pulses. The shaped pulses were characterized using both interferometric and noncollinear autocorrelation measurements using the same apparatus, as shown in Fig. 4.1(b). The second harmonic signals were generated in a β-barium borate (BBO) crystal and detected by a photomultiplier tube. In order to implement MIIPS, the photomultiplier was replaced by an optical fiber input and fed into a spectrometer. The second harmonic spectrum simultaneously provides feedback to the pulse shaper and measurement of the real-time MIIPS trace.

4.4.2 Dispersion Compensation

The output of a typical ultrafast laser system is not an ideal transform-limited pulse, even for a standard mode-locked femtosecond oscillator. When laser accessories such as optical parametric oscillators and regenerative amplifiers are used, the phase distortions become even larger. In addition, as a laser pulse travels through an experimental setup, dispersive optics further distort the pulse phase. The ability to apply the desired pulse shape precisely at the QD sample position, accounting for phase distortions accumulated from transit through the apparatus, is imperative. This requires an accurate measurement of the pulse phase so that appropriate dispersion compensation may be introduced. We employ a pulse shaping system equipped with MIIPS [86, 87]. As MIIPS is a single beam technique, and is insensitive to the optical mode, it is readily implemented at the QD sample position after all dispersive optics in the apparatus, representing a significant advantage over other pulse characterization techniques for this type of application [108, 109]. In order to implement MIIPS, the QD sample at the laser focus is replaced by a nonlinear crystal and the second harmonic (SH) spectrum is measured using an optical fiber connected to a spectrometer (Fig. 4.1(b)). As described in Ref. [86], a sinusoidal reference phase function is imposed on the input pulses using the SLM and the SH spectrum is measured as a function of the phase argument (δ). Maxima in the resulting two-dimension plot of SH wavelength

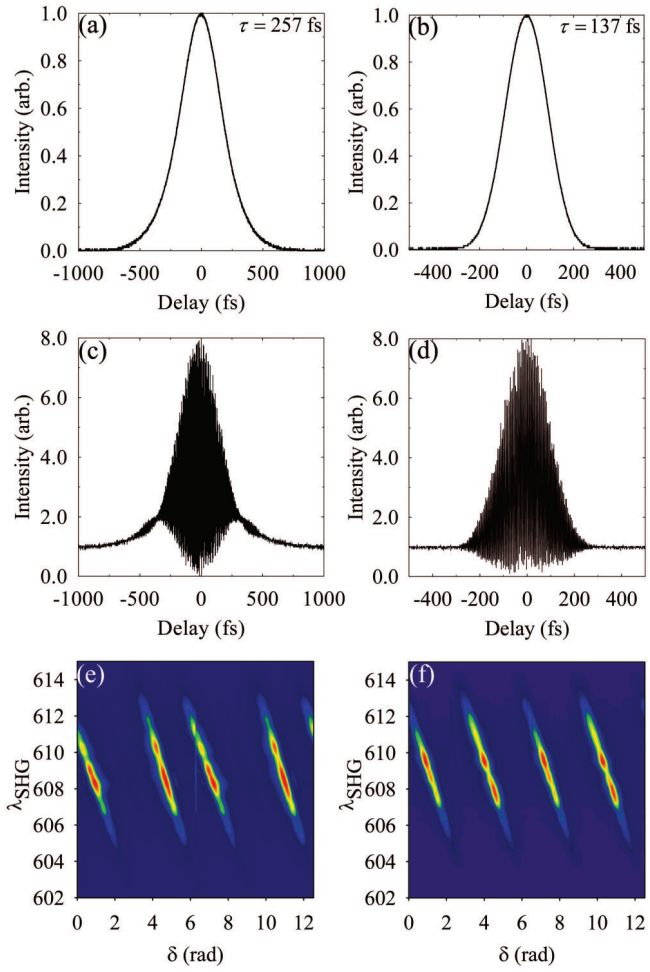

Figure 4.5: Results of pulse characterization before ((a), (c),and (e)) and after ((b), (d), and (f)) the introduction of dispersion compensation using MIIPS. (a) and (b) show the results of noncollinear autocorrelation measurements; (c) and (d) show results of interferometric autocorrelation measurements; and (e) and (f) show the measured MIIPS traces.

versus δ provide a measure of the second derivative of the pulse phase $\phi''(\omega)$. Integration then provides $\phi(\omega)$, which can be compensated using the SLM to obtain TL pulses. For completeness, the pulses in this work were also characterized using interferometric and zero-background autocorrelation techniques.

The results of pulse characterization before and after dispersion compensation are shown in Fig. 4.5. The FWHM of the zero-background autocorrelation trace before compensation is 398 fs, corresponding to a pulse duration, assuming a hyperbolic secant shape, of 257 fs. After dispersion compensation, the pulse duration is reduced to 137 fs, indicating the removal of a substantial amount of phase distortion. (Note the difference in the range of the time delay axes on the left and right sides of Fig. 4.5.) The raised wings in the

lower envelope of the interferometric autocorrelation in Fig. 4.5(c) is a characteristic signature of linear chirp (second-order phase distortion), indicating that this type of phase distortion dominates in the pulses prior to compensation. The observation of a clean TL interferometric autocorrelation in Fig. 4.5(d) indicates that these second-order phase distortions have been removed. The superior sensitivity to pulse chirp of the interferometric autocorrelation over the noncollinear autocorrelation comes at the expense of an increased complexity of optical alignment. The associated MIIPS traces are shown in Fig. 4.5(e) (before compensation) and Fig. 4.5(f) (after compensation). The results in Fig. 4.5(f) indicate evenly spaced (by π) parallel diagonal lines, as expected for a TL pulse [86]. The second-order phase distortion in the pulses prior to compensation is indicated in Fig. 4.5(e) by the appearance of unequal spacing between the lines. A small difference in the relative angle of the lines is also apparent in Fig. 4.5(e), reflecting a small amount of third-order phase distortion. In contrast, no residual phase distortion is apparent in the MIIPS trace for the compensated pulses (Fig. 4.5(f)). The dramatic difference between the pulse characterization results shown on the left and right sides of Fig. 4.5 emphasizes the essential role played by dispersion compensation in the implementation of optimized pulse shapes for quantum control experiments.

4.4.3 Shaped Pulse Characterization

The spectral and temporal characteristics of the shaped pulses are shown in Fig. 4.6 for the optimum pulse parameters corresponding to a biexciton binding energy of 2.5 meV (see Table I and Table II). It is evident from Fig. 4.6(a) that the amplitude mask leads to a large overall reduction in the total pulse area, representing an inefficient use of laser resources in the application of quantum control. In contrast, for the phase-shaping protocol, no loss of pulse area occurs in the ideal case. The characteristics of the shaped pulses in the temporal domain are presented in Fig. 4.6(c)-(h). For each shaping protocol, the measured noncollinear and interferometric autocorrelations are shown together with corresponding calculated autocorrelation traces. These calculations were obtained by numerically imposing the shaping masks onto the experimental laser spectrum assuming the input pulses have zero initial phase at all wavelengths [110]. The application of the amplitude mask introduces temporal structure on the pulse that is manifested in the autocorrelation traces through the appearance of weak shoulders. The phase-shaped pulse exhibits a complex temporal profile, leading to an autocorrelation trace with an oscillatory

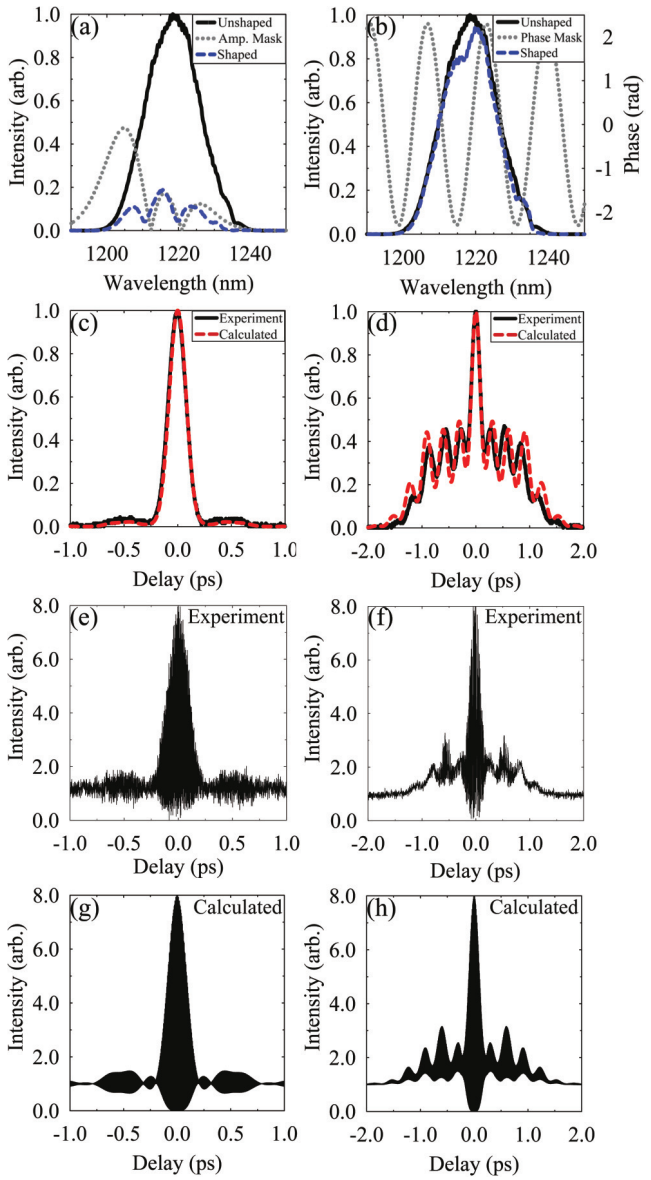

Figure 4.6: Shaped pulse characteristics for the optimized control pulses (Δ_b = 2.5 meV). Results for the amplitude-shaped pulses are shown on the left ((a), (c), (e), and (g)) and the phase-shaped pulses ares shown on the right ((b), (d), (f), and (h)). (a),(b): measured laser spectrum before and after application of the shaping mask; (c),(d): measured and calculated zero-background autocorrelations of shaped pulses; (e),(f): measured interferometric autocorrelations of the shaped pulses; (g),(h): calculated interferometric autocorrelations of the shaped pulses.

structure, as seen in Fig. 4.6(d) and Fig. 4.6(f).

Measurements of the pulse autocorrelation and spectrum provide an accurate real-time characterization tool for verifying the proper application of the shaping protocols during

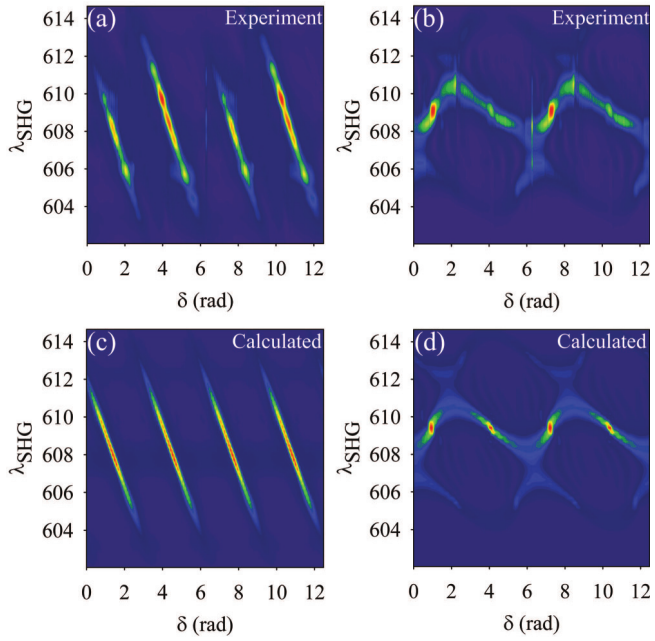

Figure 4.7: Measured MIIPS traces of (a) amplitude-shaped and (b) phase-shaped control pulses. Calculated MIIPS trace of (c) amplitude-shaped and (d) phase-shaped control pulses (Δ_b = 2.5 meV).

quantum control experiments. The need for stable spatial and temporal overlap of the two beams in the autocorrelator at the BBO crystal nevertheless makes this approach highly sensitive to drifts in the optical system. In addition, duplication of much of the optical setup is required in order to create an equivalent focus to the sample position at the location in the setup where the autocorrelator is placed. This equivalent focus is needed to accurately reproduce the dispersion effects of all optical elements in the setup. Measurements of the shaped pulse characteristics using MIIPS were also performed to gauge the sensitivity of this technique to the mask parameters. The MIIPS traces corresponding to the shaped pulses in Fig. 4.6 are shown in Fig. 4.7. Calculated MIIPS traces are also shown, for comparison. The observation of equally-spaced parallel lines in the MIIPS trace for the amplitude-shaped pulse in Fig. 4.7(a) verifies that the spectral phase profile is constant. This information is apparent from the MIIPS trace without the need for additional analysis, unlike the autocorrelation traces in Fig. 4.6(c) and Fig. 4.6(e). The severe restriction in the transmitted optical power through the shaper as a result of the imposed amplitude mask limits the signal-to-noise ratio. It is clear from the measured results in Fig. 4.7(b) that the phase mask leads to a dramatic change in the measured MIIPS trace when compared to the corresponding TL result in Fig. 4.5(f). The appearance of a cross hatch pattern is reflective

of the nonlinearity of the sinusoidal phase mask utilized for the phase shaping protocol. The calculated MIIPS traces in Fig. 4.7(c) and Fig. 4.7(d) provide good agreement with the measured MIIPS data.

The sensitivity of the MIIPS trace to the mask parameters for the phase-shaping protocol is illustrated in Fig. 4.8, where the measured MIIPS results are shown as a function of Δ_b. These traces all show a cross hatch pattern, however the locations on the trace where

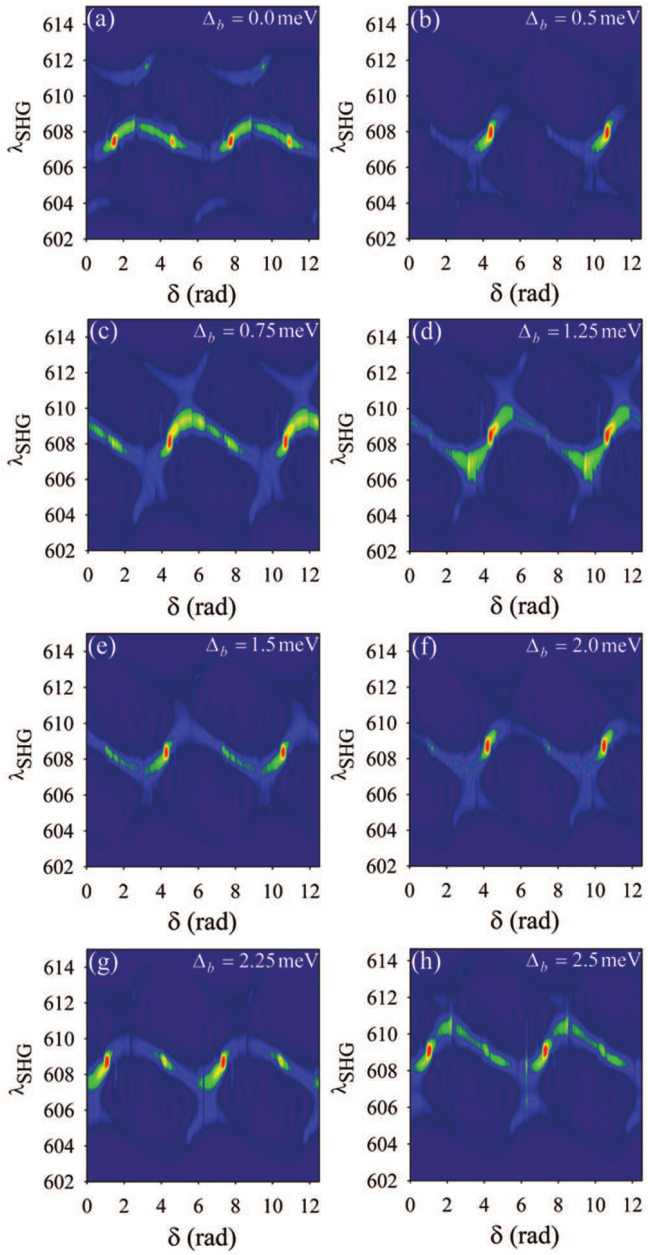

Figure 4.8: Measured MIIPS traces of phase-shaped control pulses for various values of Δ_b. The mask parameters at each Δ_b are listed in Table II.

the intensity is a maximum varies for different values of Δ_b. It is clear from the pulse parameters in Table II that the optimum values of α and γ are approximately constant for all Δ_b. The variations in the visual features in the MIIPS traces in Fig. 4.8 are therefore tied to variations in φ. In order to gain more insight into the dependence of the features in the MIIPS trace on the mask parameters, we performed numerical simulations for a wide range of values of α, γ and φ. These simulations show that α and γ have similar effect on the trace. As the magnitude of either α or γ is increased from zero, the trace evolves from parallel lines (TL case) to a cross hatch pattern. Further increasing the magnitude then leads to dissociation into modulated horizontal lines. This dependence may be seen by comparing the MIIPS traces in Fig. 4.8(a) and Fig. 4.8(e), which have different values of α. As φ is varied from $-\pi$ to π, the cross hatch pattern shifts diagonally to the lower right in the MIIPS trace, and the relative intensity of alternating cross points reverses twice. Variations in φ also lead to changes in the asymmetry of the bright regions, as evident in the MIIPS results in Fig. 4.8. The high sensitivity of the MIIPS trace to the mask parameters for the phase-shaping protocol makes it an excellent real-time diagnostic tool in quantum control experiments on semiconductor quantum dots.

4.5 Experimental Limits on Quantum Gate Performance

The pulse characterization results in Sec. 4.4.2 and 4.4.3 have allowed the authors to quantify the experimental limits on the fidelity of the C-ROT gate considered here. As other quantum processes (such as adiabatic rapid passage) are likely to be less sensitive than the C-ROT to sources of noise, the calculated gate errors obtained from our detected uncertainties represent a worst-case scenario for quantum control. There are three dominant sources of error: (i) an uncertainty in the implementation of the desired pulse shape; (ii) pulse to pulse intensity fluctuations; and (iii) fluctuations in the center wavelength. (We note that some degree of spatial chirp is occasionally detected in the experimental MIIPS traces (e.g. Fig. 4.7), however this does not represent a fundamental limitation unlike the other effects listed above [111]). Numerical simulations of the C-ROT gate were performed to determine the gate error associated with each of the above effects. The resulting changes in the gate fidelity are shown in Table 4.3. For these simulations, the error associated with (i) was estimated from the measured accuracy of dispersion compensation, as this takes

into account both the uncertainty in the calibration of the SLM and the measurement of the pulse phase prior to compensation. Using the MIIPS compensation approach (with a total of six iterations), a typical value for the ratio between the measured pulse duration τ (after compensation but before shaping) and the theoretical pulse duration τ_{TL} (based on the measured pulse bandwidth) is 1.002 indicating a small deviation from the transform-limit. The uncertainty in the imposed phase and amplitude mask was then modeled by including an unintended residual chirp in the phase profile [112] and an associated percentage change in the amplitude mask. Fluctuations in the pulse to pulse intensity reflect the stability of the OPO laser source used in this work, and are $<0.5\%$. Due to the active feedback of the cavity length, the center wavelength typically fluctuates over the range ± 0.2 nm.

It should be noted that the implementation of dispersion compensation (using MIIPS or other approaches) requires an accurate measurement of the pulse characteristics at the sample position, or at an equivalent focus. In this work, we envision quantum hardware incorporating one or more quantum dots in a lateral microcavity [20, 93], possibly extendable to an array of such cavities coupled by optical waveguides [26]. Our estimated uncertainties in the pulse shape implementation are appropriate for optical excitation parallel to the growth direction in such a configuration provided that an anti-reflection coated wafer is employed. The use of a structure incorporating a vertical microcavity would require a separate analysis of the sources of error taking into account pulse propagation effects. We note that the quantum dot selection rules do not represent a significant source of error as we have shown that the shaping protocols are effective in both cases of cylindrically symmetric and elongated quantum dots.

The results in Table 4.3 indicate that the C-ROT fidelity is more sensitive to sources of error for the phase mask than for the amplitude mask. This is likely due to the fact that the total pulse area is an adjustable parameter in the optimization routine, and for the optimum phase mask, the pulse area induces multiple Rabi rotations. It may be possible to reduce these sensitivities through use of a different mask function for the phase profile, however our analysis was limited in this work to the mask function in Eq. 4.4. The influences of experimental error are in all cases $\sim 1\%$ or less, comparable to the effects of decoherence, as discussed in Sec. 4.3 and in Ref [83]. These results reinforce the feasibility of high-fidelity quantum operations in semiconductor quantum dots.

Table 4.3: Calculated change in fidelity for the C-ROT gate associated with different sources of error determined from the measured pulse characteristics. The deviation from the ideal pulse shape is estimated using the ratio τ/τ_{TL}=1.002, which describes the accuracy of the applied dispersion compensation. Peak to peak pulse fluctuations (0.5%) and wavelength instabilities ($\pm$0.2 nm) reflect the characteristics of the OPO used in our experiments and may not represent fundamental limits.

Source of Error	Amplitude Mask	Phase Mask
Pulse Shape Inaccuracy	0.0034	0.0096
Peak to Peak Intensity Fluctuations	0.00002	0.0002
Wavelength Instability	0.0008	0.011

4.6 Conclusions

The application of pulse shaping protocols in infrared quantum control experiments on semiconductor quantum dots is investigated. Numerically-optimized pulse shapes for C-ROT operations on exciton qubits are implemented in a 4-f pulse shaper geometry using an apparatus operating at $\sim$1 eV, matching the optical transitions of In(Ga)As self-assembled quantum dots. Our pulse characterization results show that accurate dispersion compensation is essential to achieve the desired pulse shapes at the quantum dot sample, and that MIIPS provides a sensitive real-time diagnostic tool in these experiments. Our findings are used to evaluate reductions in fidelity associated with imperfections in the pulse shaping system and other noise sources, indicating that these effects lead to only $\sim$1% change, comparable to the effects of decoherence. These results indicate that high fidelity operations in semiconductor quantum dots are readily achievable with a gate time below 1 ps with the implementation of pulse shaping techniques, laying the foundation for the application of these techniques to a variety of other quantum processes.

4.7 Acknowledgments

This research is supported by the Canadian Foundation for Innovation, the Natural Sciences and Engineering Research Council of Canada, the Canada Research Chairs Program, Rockwell Collins, and Lockheed Martin Corporation.

CHAPTER 5

SIMULTANEOUS DETERMINISTIC CONTROL OF TWO SOLID STATE QUBITS USING ENGINEERED OPTICAL PULSES

Authors: Angela Gamouras[1], Reuble Mathew[1], Sabine Freisem[2], Dennis, G. Deppe[2] and Kimberley C. Hall[1]

[1]Department of Physics and Atmospheric Science, Dalhousie University, Halifax, Nova Scotia B3H4R2, Canada
[2]The College of Optics and Photonics, University of Central Florida, Orlando, Florida 32816-2700, USA

Reprinted with permission from Nano Letters, DOI: 10.1021/nl4018176, Angela Gamouras, Reuble Mathew, Sabine Freisem, Dennis G. Deppe and Kimberley C. Hall, "Simultaneous Deterministic Control of Two Solid State Qubits Using Engineered Optical Pulses". Angela Gamouras developed the techniques, performed the experiments and data analysis. Reuble Mathew carried out the theoretical analysis and numerical modeling. Sabine Freisem and Dennis G. Deppe developed and grew the sample. Kimberley C. Hall conceived and designed the experiments. Angela Gamouras and Kimberley C. Hall wrote the manuscript with input from all authors.

5.1 Abstract

In optimal quantum control (OQC) [9, 113, 114], a target quantum state of matter is achieved by tailoring the phase and amplitude of the control Hamiltonian through femtosecond pulse shaping techniques and powerful adaptive feedback algorithms [72, 73, 74, 115, 116, 117]. Motivated by recent applications of OQC in quantum information science as an approach to optimizing quantum gates in atomic and molecular systems [4, 63, 64], here we report the experimental implementation of OQC in a solid state system consisting of distinguishable semiconductor quantum dots. We demonstrate simultaneous high-fidelity π and 2π single qubit gates in two different quantum dots using a single engineered infrared femtosecond pulse. These experiments enhance the scalability of semiconductor-based quantum hardware and lay the foundation for applications of pulse shaping to optimize quantum gates in other solid state systems.

5.2 Manuscript

Optical pulse shaping provides a versatile approach to tailoring the Hamiltonian governing the interaction of light with matter. For a quantum system containing dipole-allowed optical resonances, this Hamiltonian is given by $H_{\rm int} = -\vec{\mu} \cdot \vec{E}(t)$, where $\vec{E}(t) = \frac{1}{2}\hat{\epsilon}E_0(t)[\exp(-i\omega_0 t - i\phi(t)) + \exp(i\omega_0 t + i\phi(t))]$ is the electric field of the pulse and $\vec{\mu}$ is the electric dipole moment operator. The central objective of optimal quantum control (OQC) [9, 113, 114] is to manipulate the time-dependence of the phase $\phi(t)$ and/or amplitude $E_0(t)$ to achieve a desired final state of the system at the end of the laser pulse. This approach is now used routinely in the control of a variety of physical processes (e.g., chemical reactions [115, 116], photosynthesis [117], and nonlinear optics [72, 73, 74]).

Quantum information science provides a natural arena for applications of OQC. Indeed in recent ground-breaking experiments, pulse shaping has been invoked to optimize a single qubit π-gate [63] and a two-qubit Mølmer-Sørensen entanglement gate [64] in trapped atoms, as well as a multiple-input AND gate in molecular qubits [4]. As solid state quantum computing platforms offer a strong potential for scalability together with ease of integration with classical computing hardware, the application of OQC to optimizing quantum gates in such systems is highly desirable.

Here we elucidate the utility of OQC for optimizing elementary quantum gates for solid state implementations of quantum computing by applying this approach to the simultaneous control of two solid state qubits. The solid state system considered here consists of excitons in individual semiconductor quantum dots [21, 89, 93, 94]. The two quantum states forming the quantum bit (or qubit) correspond to the presence or absence of an exciton in each quantum dot. Because of the self-assembly process used to grow the quantum dots, there is an intrinsic variability in the quantum dot size and concomitant variations in the degree of quantum confinement. As a result, qubits in different quantum dots are easily distinguishable by the optical transition energies of the associated excitons. As a test case for OQC in this system, we select two quantum dots, referred to as QD1 and QD2 (see Fig. 5.1(b)) and impose a gate pulse that simultaneously induces a π (2π) rotation

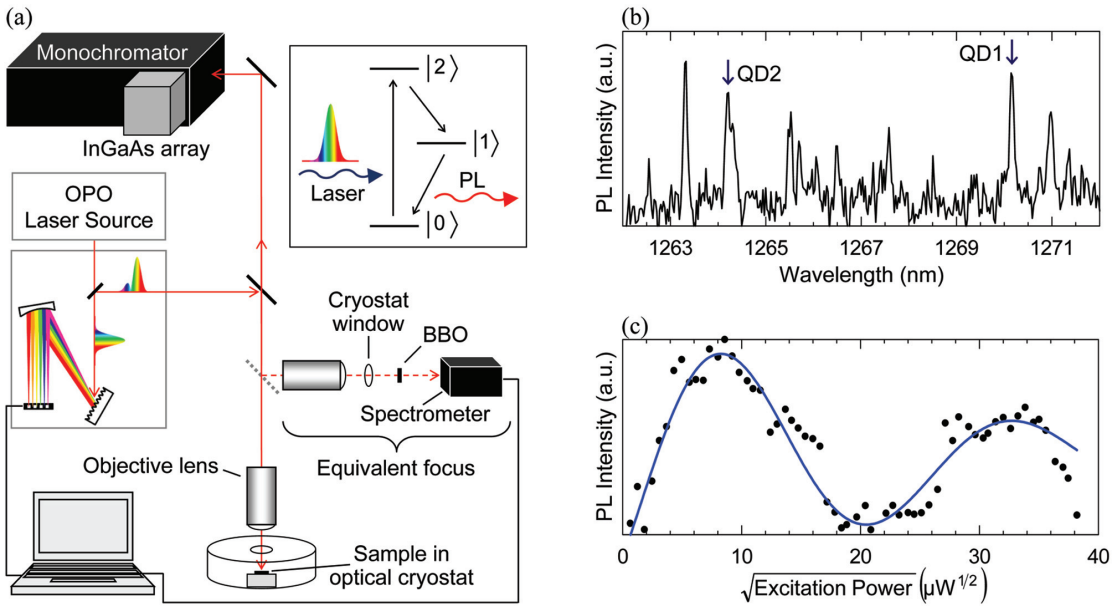

Figure 5.1: (a) Schematic diagram of the quantum control apparatus. Inset: Optical control is carried out on the p-shell transition ($|0\rangle$ to $|2\rangle$) and final quantum state readout is obtained from the time-averaged photoluminescence (PL) from the s-shell transition ($|0\rangle$ to $|1\rangle$). (b) Results of microphotoluminescence measurements showing the exciton peaks for two quantum dots selected for OQC (labeled QD1 and QD2). Peaks associated with the s-shell transitions of other QDs within the aperture are also visible. (Note: the noise floor is limited by the dark current in the InGaAs array detector.) The transition energies of the p-shell for each quantum dot were measured using photoluminescence excitation (E_{QD1} = 1.0715 eV; E_{QD2} = 1.0746 eV). (c) Results of Rabi rotation measurements on QD1. The dipole moment for each quantum dot was determined from the period of Rabi oscillations (μ_{QD1} = 29 Debye; μ_{QD2} = 24 Debye).

on the qubit in QD2 (QD1) using a single broad-bandwidth shaped femtosecond pulse. The fidelity of the gate is maximized by optimizing the pulse shape. With an eye toward future utilization of photonic infrastructure in solid state quantum hardware for enhanced scalability, the gate was designed for (and implemented experimentally on) InAs quantum dots with optical transitions near the telecommunications band at 1.3 μm with all-optical quantum state control and readout. We also apply our results to quantify limitations in gate fidelity associated with instabilities in the optical source and pulse shaping system, experimental uncertainties in the measured parameters governing the excitonic transitions in the quantum dots, and decoherence.

We utilize a phase-only shaping scheme implemented in the frequency domain using a 4-f pulse shaper [81], as shown in Fig. 5.1(a) (see Supplementary Information). In this case, the Fourier transforms of the input laser pulse ($\tilde{E}_{\rm in}(\omega)$) and the shaped pulse ($\tilde{E}_{\rm out}(\omega)$) are related by $\tilde{E}_{\rm out}(\omega) = \tilde{E}_{\rm in}(\omega)\exp[i\Phi_M(\omega)]$, where the phase of the input pulse is constant and the control phase $\Phi_M(\omega)$ is applied using a spatial light modulator in the Fourier plane. In OQC, a particular functional form is chosen for the control phase $\Phi_M(\omega)$ and the resulting parameters in the function (representing the elements of a vector) are systematically varied to optimize some experimentally observable quantity (the target quantity itself or other measured output that is indicative of the target final quantum state). In this work, the quantity subject to optimization is the fidelity of the quantum gate, given by $F = {\rm Tr}[\rho_{\rm ph}\rho_{\rm id}]$, where $\rho_{\rm ph}$ is the physical density matrix at the end of the laser pulse and $\rho_{\rm id}$ is the ideal density matrix. The time evolution of the p-shell exciton transitions under excitation by the shaped control pulse is calculated using the optical Bloch equations in the rotating wave-approximation [83, 84] using the experimentally measured transition energies and dipole moments for each quantum dot. The control phase function used here is $\Phi_M(\omega) = \alpha\cos[\gamma(\omega-\omega_0)-\varphi]$, where the adjustable parameters used to optimize the fidelity via a constrained optimization algorithm (see Supplementary Information) are α, γ, φ and the pulse area. In the experiments, the final quantum state is read out by detecting the s-shell photoluminescence from each quantum dot (see Fig. 5.1(a) inset).

The optimum control phase $\Phi_M(\omega)$ is shown in Fig. 5.2(a), together with the measured spectrum of the laser pulses. The amplitude of $\Phi_M(\omega)$ is comparable to the phase distortions associated with the laser source and dispersion introduced by the optical elements in the experimental apparatus, highlighting the need for accurate dispersion compensation

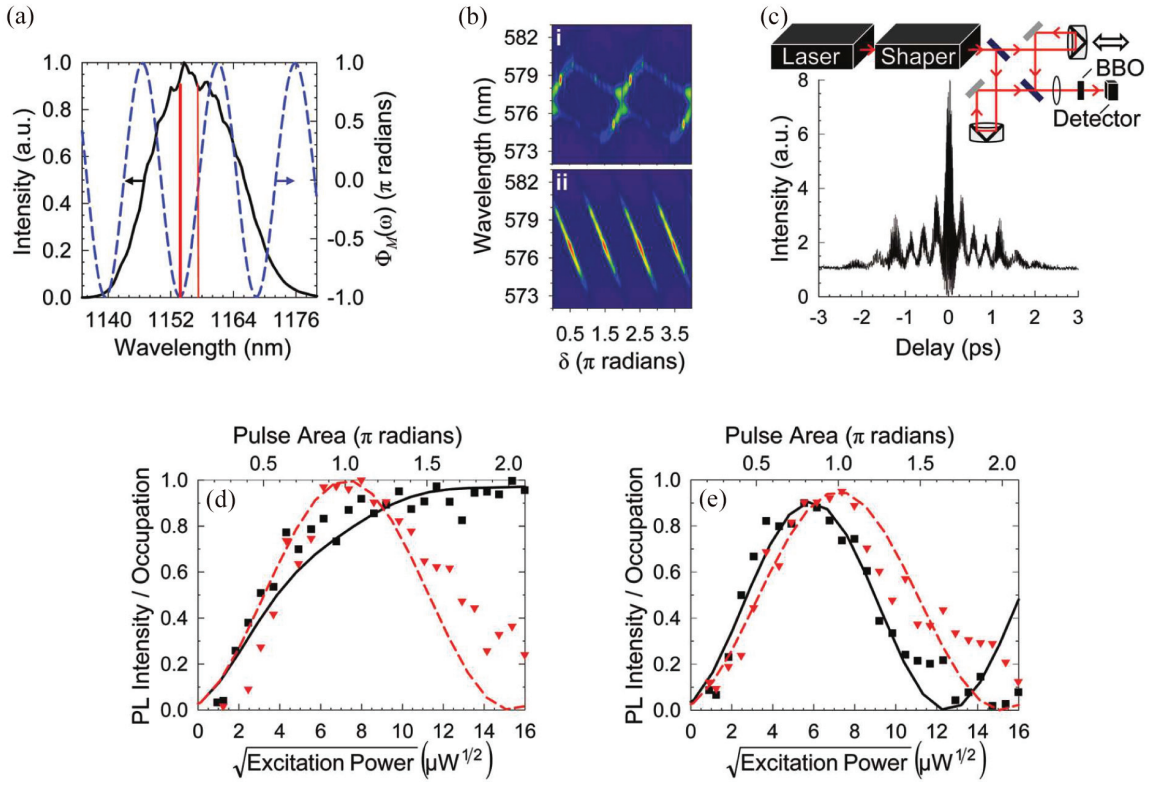

Figure 5.2: (a) Control phase $\Phi_M(\omega)$ determined using OQC (α = 0.9960π, γ = 307.1 fs, φ = -0.5751π) (dashed curve); laser pulse spectrum (solid curve). The thick (thin) vertical lines indicate the spectral positions of the exciton transition in QD2 (QD1). (b) Measured second harmonic spectrum MIIPS traces illustrating the experimental pulse characteristics for (i) the applied control phase in (a); and (ii) dispersion compensation only. The cross-hatch signature in the MIIPS trace for the shaped pulse is characteristic of the cosine phase function used for OQC in this work. (c) Interferometric autocorrelation of the shaped control pulse using the applied phase in (a). Inset: Schematic diagram of the autocorrelation apparatus. BBO: Beta barium borate nonlinear crystal. (d), (e) Measured dependence of the s-shell photoluminescence intensity on pulse area (triangles: QD1; squares: QD2), together with the calculated exciton occupations (red dashed curve: QD1; black solid curve: QD2) for the shaped control pulse (d) and the unshaped pulse (e). The maximum pulse area is the theoretical optimum control pulse area determined using OQC ($\Theta = 2.042\pi$). The PL intensities are scaled to match the maximum PL observed in resonant Rabi oscillations on each quantum dot within experimental uncertainty.

(see Supplementary Information). The dispersion compensation phase was determined using multiphoton intrapulse interference phase scan (MIIPS) [86, 87] (Fig. 5.2(b)) resulting in an unshaped pulse with a duration within 1% of the corresponding transform-limited value. This compensation phase was added to the calculated phase to obtain the experimental shaped control pulse. $\Phi_M(\omega)$ increases the duration of the dispersion-compensated

pulses from 130 fs to a few picoseconds, as seen in the interferometric autocorrelation in Fig. 5.2(c).

The results of experimental execution of the quantum gate using the shaped control pulse are shown in Fig. 5.2(d). The photoluminescence intensity from the s-shell of each quantum dot is plotted together with the calculated exciton occupations as a function of pulse area. The shaped control pulse executes a π (2π) rotation on the qubit in QD2 (QD1) with high fidelity, in agreement with the theoretical simulations. In contrast, for excitation using the unshaped pulse (Fig. 5.2(e)), the excitons in both quantum dots undergo a simple Rabi oscillation at a rate determined by their individual dipole moments. The calculated dynamics for both shaped and unshaped control pulses are shown in a Bloch sphere representation in Fig. 5.3(a). Pulse shaping increases the fidelity of the quantum gate from 0.294 to 0.968. The ability to achieve simultaneous deterministic control of multiple qubits in different quantum dots (with different dipole moments and optical transition energies) using a single broadband optical pulse is enabled by femtosecond pulse shaping. These results highlight the efficacy of OQC for optimizing the performance of quantum gates in solid state systems.

The adjustable parameters α, γ, and φ determine the amplitude of $\Phi_M(\omega)$ as well as the energetic locations of critical points (Fig. 5.2(a)). For the optimum phase in Fig. 5.2(a), $\Phi_M(\omega)$ exhibits a minimum at the transition energy of QD2, where the magnitude of the second derivative ($\Phi''_M(\omega)$) is maximum. In contrast, the transition energy of QD1 is close to the point where $\Phi''_M(\omega) = 0$. This suggests that the shaped control pulse induces adiabatic passage on the exciton in QD2, resulting in a π rotation, while the exciton in QD1 undergoes an evolution that resembles a simple Rabi oscillation (reaching 2π by the end of the control pulse). This interpretation was verified by shifting $\Phi_M(\omega)$ in energy by -2 meV, placing QD1 near the extremum of the new control phase function. The quantum state evolution using this shifted control phase is shown in Fig. 5.3(b), indicating a reversal of the roles played by QD1 and QD2 in the gate. Adiabatic passage has been demonstrated in atomic systems [67], and also recently in single semiconductor quantum dots [30, 51]. In Refs. [30] and [51], a simple grating stretcher was used to create a linear pulse chirp (constant value of $\Phi''_M(\omega)$). The simultaneous control of excitons in multiple distinguishable quantum dots requires the implementation of OQC (in which general pulse shape optimization is employed), as we demonstrate here.

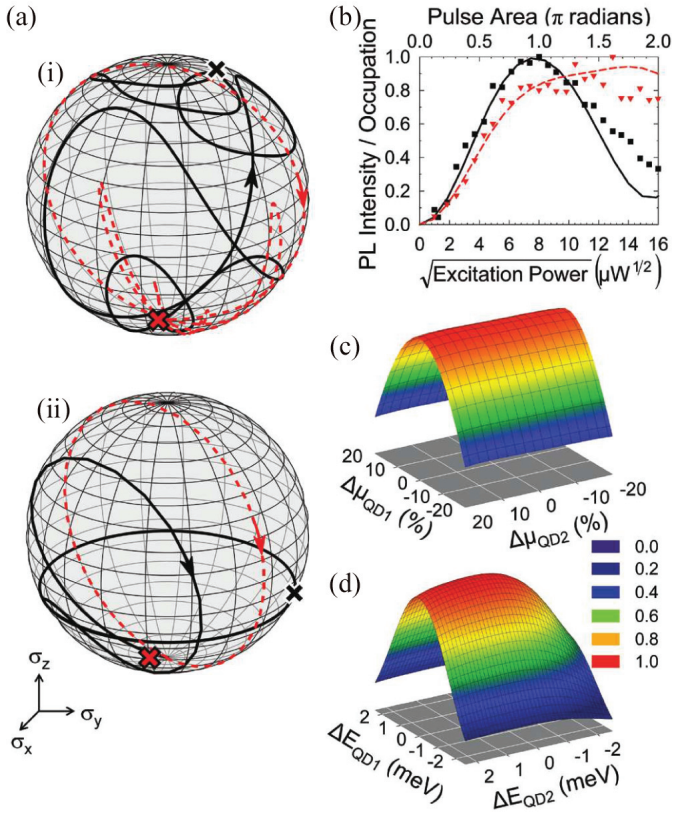

Figure 5.3: (a) Calculated quantum state dynamics for the exciton in QD1 (red dashed curve) and QD2 (black solid curve) in a Bloch vector ($\vec{\sigma}$) representation for excitation with: (i) the shaped control pulse and (ii) an unshaped pulse (see Supplementary Movies S1, S2). The pulse area is 2.041π, corresponding to the maximum gate fidelity for the shaped control pulse. The tip of the Bloch vector at the end of the optical pulse is indicated by a cross, for clarity. (b) Measured pulse area dependence of the s-shell photoluminescence (PL) intensity (triangles: QD1; squares: QD2), together with the calculated exciton occupation (red dashed curve: QD1; black solid curve: QD2) for a control pulse obtained by translating the optimum control phase in Fig. 5.2(a) by -2 meV, placing QD1 close to the minimum of the cosine phase function [118]. (c), (d) Calculated gate fidelity using the shaped control pulse for deviations in the electronic structure parameters of the quantum dots relative to the measured values. The experimental uncertainties are $\pm 5\%$ for the dipole moments (c) and ± 0.25 meV for the quantum dot transition energies (d), however the results are shown over a broader range. The insensitivity of the gate fidelity to the dipole moment and transition energy of QD2 is consistent with the robustness of adiabatic passage. The fidelity drops as the transition energy of QD2 approaches QD1 since in this limit QD1 and QD2 can no longer be resolved.

For quantum computing applications, it is imperative that unintended quantum state evolution associated with imperfections in the gate be minimized. We have estimated the gate

error associated with our measured experimental uncertainties by incorporating these uncertainties into our numerical simulations of the quantum state dynamics (see Supplementary Information). Limitations in gate accuracy arise from: (i) pulse to pulse fluctuations in the laser source (intensity or wavelength); (ii) deviations from an ideal pulse shape associated with imperfect dispersion compensation; and (iii) experimental uncertainty in the electronic structure parameters of the quantum dots. We calculate associated reductions in fidelity of ΔF = 0.01, 0.006, and 0.01 for each of these contributions, respectively. The reduction in fidelity due to laser fluctuations is dominated by the wavelength stability of the OPO laser source. The error associated with the electronic structure parameters is dominated by the uncertainties for QD1 (Fig. 5.3(c), (d)), reflecting the robustness of adiabatic passage carried out on QD2. Inclusion of measured decoherence (T_2) and energy relaxation (T_1) times for similar quantum dots [37, 119] reduces the fidelity by a comparable amount to these gate errors (ΔF = 0.005) (see Supporting Information). The small influence of decoherence during the control pulse is due to the ultrafast time scale of the gate relative to T_2 [83, 84]. These small gate errors in conjunction with the implementation of strategies for decoherence mitigation [27, 100, 120, 121, 122] are promising for the development of solid state quantum computing hardware.

The achievement we report here of deterministic control of qubits in two uncoupled QDs within the micrometer-scale control laser focal spot using OQC will aid in the development of scalable solid state quantum computing hardware. We envision local quantum simulators containing a small number of quantum dots in a single optical microcavity, such as a whispering gallery mode structure incorporating lateral optical confinement with QDs controlled by tailored femtosecond pulses incident from the top. Such a simulator could exploit complex instruction sets to manipulate multiple qubits in parallel using suitably shaped control pulses [4, 9] and may utilize local microcavity modes for entanglement [20]. These small quantum simulators could be integrated into a larger computing platform in which long-range entanglement between qubits in different simulators is achieved using optical waveguide modes [26]. The number of quantum dots in the local simulators could reach 10-20 with the use of more general phase functions in the OQC optimization scheme and readily available high-resolution spatial light modulators. Together with recent advances in the ability to manipulate single exciton and spin qubits in semiconductor QDs [30, 43, 51, 52, 54, 96, 123] as well as realization of entanglement between qubits and

single photons [124, 125], the experimental demonstration we report here of high-fidelity deterministic control of qubits in spatially distant, uncoupled QDs represents an important step in achieving scalability for such a semiconductor-based quantum computing platform. The achievement in this work of all-optical excitation and quantum state readout on QDs with optical transitions near the telecommunications band at 1.3 μm further enhances this potential for scalability by facilitating future utilization of photonic infrastructure. In addition to laying the groundwork for implementation of OQC involving other quantum gates, our results open the door to applications of femtosecond pulse shaping to decoherence mitigation in solid state quantum hardware [121, 122].

5.2.1 Acknowledgements

This research is supported by the Natural Sciences and Engineering Research Council of Canada and Lockheed Martin Corporation.

5.3 Supplementary Information

5.3.1 Materials and Methods

5.3.1.1 Experimental Techniques

The optical source used in this work is a wavelength tunable 76 MHz optical parametric oscillator laser system producing optical pulses around 1.2 μm. The self-assembled InAs/GaAs quantum dot wafer was mounted on an attocube nanopositioning stage inside a helium flow microscopy cryostat at 10 K, as shown in Fig. 5.4. A high numerical aperture microscope objective (NA 0.7, 100$\times$) designed for infrared wavelengths was used for both laser excitation and collection of the emitted photoluminescence. The photoluminescence spectrum was detected using a 0.75 m monochromator with 30 μeV spectral resolution and a liquid nitrogen-cooled InGaAs array detector.

An ideal *unshaped* control laser pulse has a constant phase, leading to the shortest possible temporal duration considering its frequency bandwidth. Such a pulse is referred to as a transform-limited (TL) pulse. The typical output from ultrafast oscillator laser systems is generally not an ideal TL pulse, but can exhibit significant linear and higher order phase structure (*i.e.* the pulse phase has an unintended frequency dependence, called *chirp*). In addition, the optical pulse can accumulate phase structure by propagating through various optical components in the experimental apparatus. The associated unintended

phase structure must be characterized and compensated for prior to application of the optimum shaping mask. This process is called dispersion compensation, and is carried out in this work using multiphoton intrapulse interference phase scan (MIIPS) [86]. The pulse shaping system used in these experiments consists of an infrared 4f pulse shaper incorporating a computer controlled dual mask 128 pixel spatial light modulator (SLM). Feedback to the pulse shaping system for dispersion compensation using MIIPS was provided by the second harmonic spectrum, in which a BBO nonlinear crystal was placed at an equivalent focus to the sample position. Application of the dispersion compensation phase mask determined using MIIPS resulted in an optimized unshaped pulse with a duration of 130 fs, within 1 % of the TL value (*i.e.* $\tau/\tau_{\mathrm{TL}} \leq 1.01$, where τ = 130 fs and τ_{TL} is the ideal pulse duration dictated by the measured pulse bandwidth). This dispersion compensation phase mask was added to the calculated optimum phase mask for the phase control experiments. Figure 5.5 shows calculated MIIPS traces for the TL as well as the shaped optical pulses. The equally spaced parallel lines in Fig. 5.5(a) are characteristic of a TL optical pulse, while the cross-hatched pattern in Fig. 5.5(b) is a signature of the cosine phase function used here. The measured interferometric autocorrelation for the dispersion compensated pulse is shown in Fig. 5.5(c), together with the corresponding calculated autocorrelation in Fig. 5.5(d). Calculated MIIPS and autocorrelation plots for both TL and shaped pulses are in agreement with the experimentally measured traces shown in

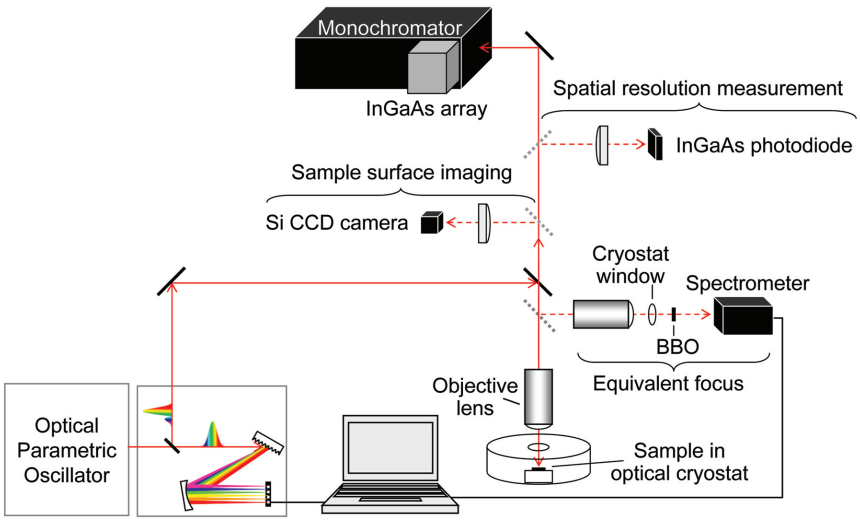

Figure 5.4: Diagram of quantum control apparatus showing alignment configurations for laser spot size measurement and imaging of quantum dot sample surface.

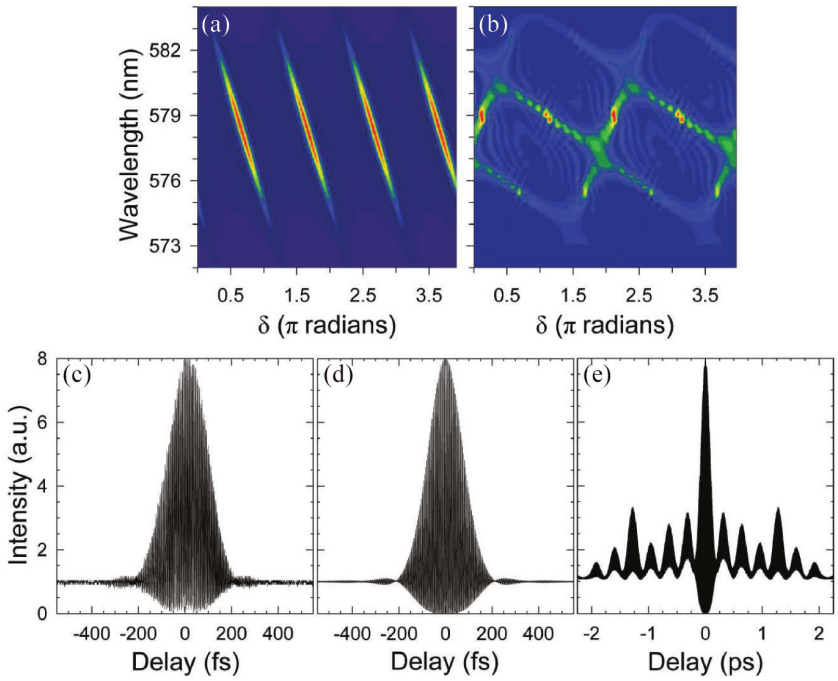

Figure 5.5: Calculated MIIPS traces of (a) the transform-limited pulse and (b) the phase shaped control pulse. (c) Measured interferometric autocorrelation of the dispersion-compensated pulse. Calculated autocorrelation traces of (d) the transform-limited pulse and (e) the phase shaped control pulse.

Fig. 5.5(b) and Fig. 5.2 in the main text.

The Gaussian beam spot size of the focused excitation laser at the sample, required for calculation of the electric dipole moments of the selected quantum dots, was determined using a knife-edge type measurement. The focused laser beam was reflected off a laterally translating metallic step edge on the masked quantum dot sample within the microscopy cryostat. The resulting change in reflectivity was measured using an InGaAs photodiode. The collected reflectivity data was differentiated and fit to a Gaussian function to extract the laser spot size.

5.3.1.2 Sample

The InAs/GaAs quantum dot structure was grown by molecular beam epitaxy under conditions optimized for a sparse quantum dot ensemble with the ground state optical transition of the quantum dots near 1.3 μm. The single quantum dot layer was deposited on top of 200 nm of GaAs under indium-rich conditions. The quantum dots were overgrown with $In_{0.2}Ga_{0.8}As$ at a low growth temperature to reduce intermixing, followed by 65 nm of GaAs. AlGaAs carrier blocking layers were deposited above and below the GaAs

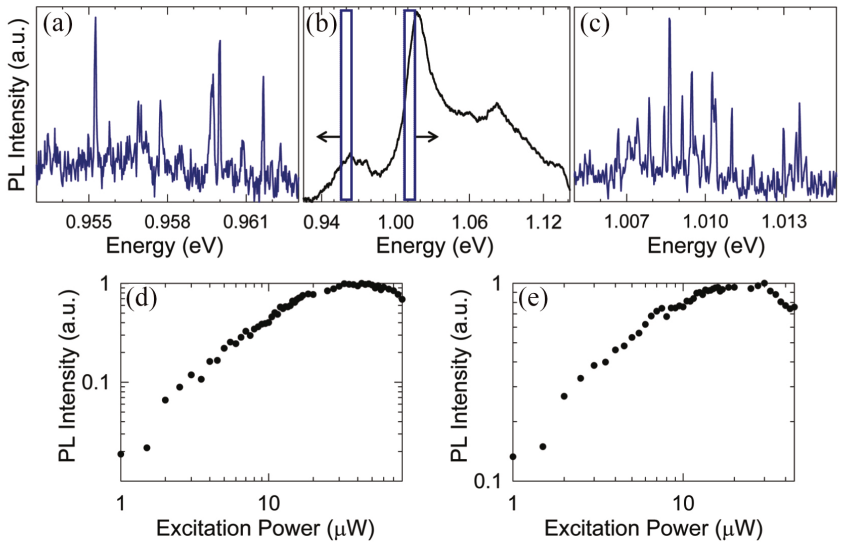

Figure 5.6: Photoluminescence spectra from the InAs/GaAs QD structure at 10 K. (a) Microphotoluminescence from the lower-energy QD subset. (b) Ensemble PL from the unmasked QD structure. The rectangles indicate the energy ranges of microphotoluminescence in (a) and (c). (c) Microphotoluminescence from the higher-energy QD subset. (d)((e)) Power dependence of the s-shell emission observed in μPL for QD1 (QD2).

layers. The photoluminescence for this structure is shown in Fig. 5.6. From corresponding photoluminescence excitation experiments, we determined that the peaks in Fig. 5.6(b) at 0.965 eV (1285 nm) and 1.017 eV (1220 nm) are due to ground state emission from two distinct subsets of quantum dots within the ensemble. The separation between the ground state and excited state transitions in these subsets are 95 meV and 75 meV, averaged over the ensemble, respectively. As a result, the small peak at 1.083 eV (1145 nm) in Fig. 5.6(b) is attributed to the excited state transition in the higher-energy subset of quantum dots. The lower-energy quantum dot subset has an estimated areal density of 6×10^9 cm^{-2}, an average quantum dot height of 9 nm and a lateral size of 20 nm from cross-sectional transmission electron microscopy and atomic force microscopy on similar structures. To facilitate spectral isolation of individual quantum dots, a metallic mask containing an array of apertures of varying sizes (0.1 μm to 1.0 μm) was deposited onto the sample surface. Microphotoluminescence measurements, using 830 nm continuous wave laser excitation, show single quantum dot peaks in both subsets of the ensemble (Fig. 5.6). The experiments reported here were carried out on quantum dots within a 0.4 μm aperture in the lower-energy subset. The power-dependence of the s-shell μPL for QD1 (QD2) is shown in Fig. 5.6(d) (Fig. 5.6(e)). The saturation of the s-shell emission for high pump

powers has been observed in similar QDs [126].

5.3.2 Description of Model

The theoretical model treats QD1 and QD2 as independent two-level systems, each consisting of a vacuum state $|g\rangle$ and p-shell exciton state $|e\rangle$ with their respective transition energies $\hbar\omega_{eg}$. The quantum states are manipulated using the electric field of a laser pulse given by,

$$\vec{E}(t) = \frac{1}{2}\hat{\epsilon}E_0(t)[\exp(-i\omega_0 t - i\phi(t)) + \exp(i\omega_0 t + i\phi(t))], \tag{5.1}$$

where ω_0 is the center frequency of the laser pulse, $\phi(t)$ is the temporal phase, and $E_0(t)$ is the electric field envelope. In the calculation, the envelope is taken to be in the form:

$$E_0(t) = |E_0|\mathrm{sech}(1.76t/\tau), \tag{5.2}$$

where τ is the pulse width. For a transform-limited pulse, $\phi(t) = \phi_0$ is constant. The interaction of the electric field with each quantum dot is calculated using the Liouville equation for the density matrix

$$\dot{\rho} = \frac{i}{\hbar}[\rho, H_0 + H_{\mathrm{int}}], \tag{5.3}$$

where H_0 is the unperturbed Hamiltonian and $H_{\mathrm{int}} = -\vec{\mu}\cdot\vec{E}(t)$ is the interaction Hamiltonian with dipole moment operator $\vec{\mu}$. The resulting optical Bloch equations in the rotating wave approximation, with change of variables $\rho_{ij} \rightarrow \tilde{\rho}_{ij}$ to remove fast variations in the coherences, are given by

$$\dot{\tilde{\rho}}_{ee} = (-i/2)\left[\Omega_R\tilde{\rho}_{ge} - \tilde{\rho}_{eg}\Omega_R^*\right] - \Gamma_{ee}\tilde{\rho}_{ee}, \tag{5.4a}$$

$$\dot{\tilde{\rho}}_{eg} = (-i/2)\left[2\Delta\tilde{\rho}_{eg} - \Omega_R(2\tilde{\rho}_{ee} - 1)\right] - \Gamma_{eg}\tilde{\rho}_{eg}, \tag{5.4b}$$

where $\Omega_R = -\mu_{eg}E_0(t)/\hbar$ is the complex Rabi frequency, $\Delta \equiv \omega_{eg} - \omega$ is the laser detuning, ρ_{ee} is the population in state $|e\rangle$, and ρ_{eg} is the coherence between states $|e\rangle$ and $|g\rangle$. Γ_{ee} and Γ_{eg} are the constant population decay rate and constant dephasing rate, respectively. The density matrix for the combined system is the direct product of the density matrices for the two quantum dots ($\rho = \rho_1 \otimes \rho_2$) and the fidelity of the operation is defined as

$$F = \mathrm{Tr}[\rho_{\mathrm{ph}}\rho_{\mathrm{id}}], \tag{5.5}$$

where ρ_{ph} is the physical density matrix for a given laser pulse and ρ_{id} is the ideal density matrix for the quantum gate.

We engineer the quantum state evolution of QD1 and QD2 by manipulating $E(t)$, and hence H_{int}, using a 4-f pulse shaper, which provides independent control over the frequency-dependent amplitude and phase of the pulse. The effect of the SLM in the pulse shaper may be modeled as a linear filter with a frequency response $M(\omega)$ given by

$$M(\omega) = A_M(\omega) \exp\left[i\Phi_M(\omega)\right], \tag{5.6}$$

where $A_M(\omega)$ and $\Phi_M(\omega)$ are user-defined amplitude and phase functions. The Fourier transform of the laser pulse after the shaper, $\tilde{E}_{\mathrm{out}}$, is related to the input pulse, $\tilde{E}_{\mathrm{in}}$, by

$$\tilde{E}_{\mathrm{out}}(\omega) = \tilde{E}_{\mathrm{in}}(\omega) M(\omega). \tag{5.7}$$

The use of MIIPS for dispersion compensation allows us to assume a transform-limited input pulse $\tilde{E}_{\mathrm{in}}(\omega)$. For the purposes of this study we set $A_M(\omega) = 1$ and use phase-only control, which serves to conserve pulse power. The functional form of $\Phi_M(\omega)$ was chosen to be

$$\Phi_M(\omega) = \alpha \cos[\gamma(\omega - \omega_0) - \varphi], \tag{5.8}$$

where α is the amplitude, γ is the spectral frequency, and φ is the phase shift. The fidelity $F = f(\alpha, \gamma, \varphi, \Theta)$ of the operation is optimized as a function of α, γ, φ and the pulse area ($\Theta = (\vec{\mu} \cdot \hat{\epsilon}/\hbar) \int_{-\infty}^{+\infty} E_0(t)\, dt$).

During optimization, the parameters are subject to the following constraints

$$0 \leq \alpha \leq \pi, \tag{5.9a}$$

$$0 \leq \gamma \leq 315\,\mathrm{fs}, \tag{5.9b}$$

$$-\pi \leq \varphi \leq \pi, \tag{5.9c}$$

$$\pi/2 \leq \Theta \leq 5\pi/2. \tag{5.9d}$$

The constraints on α and γ serve to restrict the gradient in the phase to approximately $\pi/10$ radians per pixel, a conservative restriction for the 128-pixel SLM used in this work, while the constraint on Θ limits the optimized pulse shapes to relatively low pulse areas.

To optimize the fidelity of the quantum gate, we choose a mask function defined by

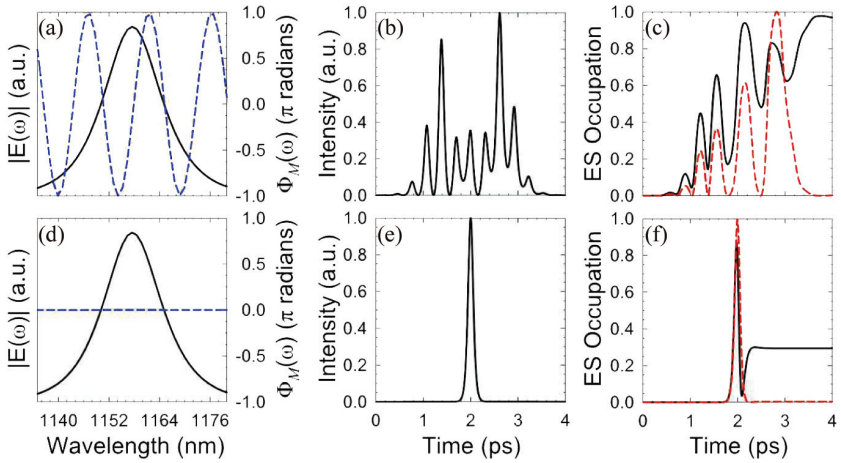

Figure 5.7: Pulse characteristics and population dynamics for a shaped pulse ((a), (b), (c)) and a transform-limited pulse ((d), (e), (f)). (a) and (d) show the amplitude (solid black curve) and phase (dashed blue curve). (b) and (e) show the temporal electric field intensity. (c) and (f) show the population dynamics of the p-shell exciton state (ES) for QD1 (red dashed curve) and QD2 (black solid curve).

a vector $q_i = \{\alpha_i, \gamma_i, \varphi_i, \Theta_i\}$ within the parameter space defined by Eq. 5.9, apply the mask to a TL pulse (with the experimentally measured pulse width of 130 fs), and calculate the electric field which dictates the time dependence of the interaction Hamiltonian. We then integrate the Bloch equations (Eq. 5.4) to determine the state dynamics and the fidelity F_i (Eq. 5.5). The vector q_i is driven towards a local optimum in fidelity F_{opt} with associated vector $q_{opt} = \{\alpha_{opt}, \gamma_{opt}, \varphi_{opt}, \Theta_{opt}\}$ using the constrained optimization by linear approximations (COBYLA) algorithm [127]. We find that repeating this procedure with 500 initial vectors q_i, selected using a quasi-random Sobol' sequence [128], provides sufficient coverage of the parameter space to find a q_{opt} vector with high fidelity ($F > 0.95$).

Shown in Fig. 5.7 is a comparison of the pulse characteristics and quantum state dynamics for a TL pulse (Fig. 5.7(d), (e), (f)) and a shaped pulse (Fig. 5.7(a), (b), (c)) corresponding to the highest gate fidelity found by the optimization algorithm. (The quantum gate is the same as that described in the main text, *i.e.*, a π rotation for QD2 and 2π rotation for QD1.) The shaped pulse is defined by the vector $q = \{0.9960\pi, 307.1\,\text{fs}, -0.5751\pi, 2.042\pi\}$. The first column of panels in Fig. 5.7 shows the spectral amplitude and phase, and the second column displays the electric field intensity as a function of time for both pulses. The third column of panels presents the resulting occupation dynamics of the p-shell exciton state $|e\rangle$ as a function of time for QD2 and QD1. The pulse area of the TL pulse is chosen

to match that of the shaped pulse (*i.e.*, $\Theta = 2.042\pi$). The shaped pulse executes the gate with a fidelity of 0.968 compared to 0.294 for the TL pulse.

5.3.3 Experimental Limitations on Gate Fidelity

Practical limits on the performance of the quantum gate considered in this work were assessed by calculating the gate fidelity including sources of experimental error. This allows us to gauge the sensitivity of quantum gates more generally for the physical implementation of exciton qubits in self-assembled quantum dots. The laser source exhibits fluctuations in pulse to pulse intensity ($\pm$0.5 %) and in centre pulse wavelength ($\pm$0.2 nm). The associated reductions in fidelity are 0.005 and 0.01, respectively. The wavelength instability arises from active feedback in the optical parametric oscillator laser source used in this work. The accuracy of the applied pulse shape is limited by the quality of dispersion compensation, which is indicated by the ratio $\tau/\tau_{\rm TL}$, which is typically 1.002 in our experiments. Taking a more conservative value of $\tau/\tau_{\rm TL}$ = 1.01 and including the associated residual phase distortions in the theoretical calculations by adding a corresponding amount of linear chirp, we obtain ΔF = 0.005. For experimental uncertainties in the quantum dot electronic structure parameters (p-shell transition energy, dipole moment), the reduction in fidelity was largest when including deviations from the measured values for QD1, reflecting the robustness of adiabatic passage on QD2. For QD1, the $\pm$0.25 meV uncertainty in the transition energy (from photoluminescence excitation measurements) and $\pm$5% for the dipole moment (from Rabi oscillations), each result in a reduction in fidelity of 0.01. For schemes involving optical control of the s-shell transition (using *e.g.* quantum state readout via a resonance fluorescence configuration [129] or detection of the nonlinear optical response [55]), the uncertainty in the transition energy would be smaller, limited only by the $\sim$ 50-100 μeV linewidth of the s-shell due to spectral wandering [37]. The relevant experimental error in the dipole moment for design of the gate pulse is the measurement error for the laser power required for a Rabi oscillation. Decay and decoherence are incorporated into the calculations within the relaxation time approximation [83]. For the s-shell transition, four-wave mixing experiments on similar InAs QDs indicated a radiatively-limited decoherence time of 1 ns at low temperature [119]. For the p-shell transition, T_2 is several tens of picoseconds, limited by energy relaxation to the s-shell [130]. Due to the short time scale of the control pulse relative to these relaxation times, the influence of decoherence on gate fidelity is small. For quantum computing applications,

optical control of the s-shell is preferred due to the much longer lifetime of the qubit *after the control pulse is over*. The reduction in fidelity due to decoherence and relaxation using typical values of T_1 and T_2 for the s-shell in these quantum dots [37, 119] is 0.005, similar to the calculated gate errors associated with other uncertainties, as described above. These small errors are promising for the prospect of realising practical quantum computing hardware based on self-assembled quantum dots.

CHAPTER 6

ENERGY-SELECTIVE QUBIT ENCODING IN INAS/INP QUANTUM DOT ENSEMBLES USING A ONE-DIMENSIONAL OPTICAL MICROCAVITY

Authors: Angela Gamouras[1], Mathew Britton[1], Mohanad M. Khairy[1], Reuble Mathew[1], Dan Dalacu[2], Philip Poole[2], Daniel Poitras[2], Robin L. Williams[2] and Kimberley C. Hall[1]

[1]Department of Physics and Atmospheric Science, Dalhousie University, Halifax, Nova Scotia B3H4R2, Canada

[2]Institute for Microstructural Sciences, National Research Council of Canada, Ottawa, Canada, K1A 0R6

Submitted to Applied Physics Letters on August 22, 2013. Angela Gamouras developed the pump-probe techniques, performed the majority of the pump-probe, CWPL and transmission measurements and analyzed the pump-probe, CWPL and transmission data. Mathew Britton performed selected pump-probe and CWPL measurements and analyzed CWPL data under the guidance of Angela Gamouras. Mathew Britton also wrote a MAPLE code to understand changes in the cavity mode wavelength due to index of refraction effects. Mohanad M. Khairy developed the CWPL and transmission measurement techniques. Reuble Mathew wrote the pump-probe data analysis code and assisted with experiments.

Dan Dalacu, Philip Poole, Daniel Poitras and Robin L. Williams developed and grew the sample. Kimberley C. Hall conceived and designed the experiments. Angela Gamouras and Kimberley C. Hall wrote the manuscript with input from all authors.

6.1 Abstract

We demonstrate the selective optical excitation and detection of subsets of quantum dots within an InAs/InP ensemble using a SiO_2/Ta_2O_5-based optical microcavity. The low variance of the exciton transition energy and dipole moment tied to the narrow linewidth of the microcavity mode is expected to facilitate effective qubit encoding and manipulation in a quantum dot ensemble with ease of quantum state readout relative to qubits encoded in single quantum dots.

6.2 Manuscript

Semiconductor quantum dots (QDs) are promising for the prospect of developing a scalable quantum computing platform that would exploit rapidly advancing semiconductor and photonic device fabrication technology and facilitate integration with classical computing hardware. This strong potential has stimulated rapid progress in the control of fundamental charge (exciton) and spin states in individual semiconductor QDs using coherent optical techniques [40, 42, 43, 44, 45, 51, 52, 54, 55, 131, 132, 123]. In these experiments, a variety of strategies have been developed to overcome the formidable technical challenge associated with the low optical response of an individual quantum dot. Quantum state readout via detection of photoluminescence (PL) from single QDs [43, 45] requires highly-sensitive low-light detectors, a constraint that has hindered progress on QDs with emission compatible with telecommunication infrastructure. Photocurrent detection methods [44] eliminate this difficulty at the expense of a fast carrier tunnel rate, which can limit the qubit coherence decay time. A phase-sensitive homodyne detection technique has recently been developed that permits transmission-based measurements on single self-assembled QDs [133], but the difficulty associated with the low optical signal relative to background noise sources remains.

Encoding qubits in ensembles of QDs would greatly simplify quantum state readout, facilitating the transition from fundamental optical control experiments to applications. A

variety of coherent phenomena have been observed in QD ensembles, including quantum beats between spin-polarized excitons [56, 134], the generation of Raman spin coherence through optical pumping of trion transitions [135], spin mode-locking involving electrons [60] and holes [136, 137] and resonant pumping of a dynamic nuclear spin polarization [138]. Coherent qubit operations have also been demonstrated in ensembles involving both excitons [57, 58, 139, 140] and spin-polarized electrons [29, 61] in recent years. In these experiments, inhomogeneity in the electronic structure parameters of the QDs (transition energy, dipole moment) was found to limit the fidelity of the control process. Here we investigate the efficacy of a one-dimensional optical microcavity for reducing the deleterious effects associated with inhomogeneity for qubit encoding and optical manipulation in QD ensembles. Microcavities play a central role in many solid state quantum computing proposals because they provide a means of establishing long-range entanglement between qubits [20, 26], and are central to the development of efficient single photon sources [141]. We present differential transmission measurements on an ensemble of InAs/InP QDs within an optical microcavity based on SiO_2/Ta_2O_5 Bragg reflectors. Our results demonstrate that the angle dependent transmission resonance of the microcavity permits separate excitation and detection of distinct subsets of QDs with strongly diminished variances in exciton transition energy and dipole moment. Our findings suggest that high-fidelity optical quantum gates on ensemble-encoded exciton (or spin) qubits would be feasible in this system, with greatly simplified quantum state readout relative to qubits encoded in single QDs.

The optical microcavity investigated here was fabricated using the methods described in Ref. [31]. It contains an ensemble of InAs/InP QDs within a λ cavity formed from an InP spacer layer and two SiO_2/Ta_2O_5 Bragg stacks. The Bragg stacks contain 8 periods of SiO_2/Ta_2O_5, and have a stop band 200 meV wide centered on the microcavity resonance at normal incidence. A schematic diagram of the layer structure is shown in the inset of Fig. 6.1(a). The QD ensemble was grown using chemical beam epitaxy and has an estimated areal density of 2 μm^{-2}. Results of transmission and continuous-wave PL measurements on this structure are shown in Fig. 6.1(a)-(c). For PL experiments, an 838 nm laser diode was used to inject electron-hole pairs into the InP barriers and the resulting PL from the InAs QDs was resolved with a 0.75 m monochromator and InGaAs array detector. For transmission experiments, the optical source was a tunable optical

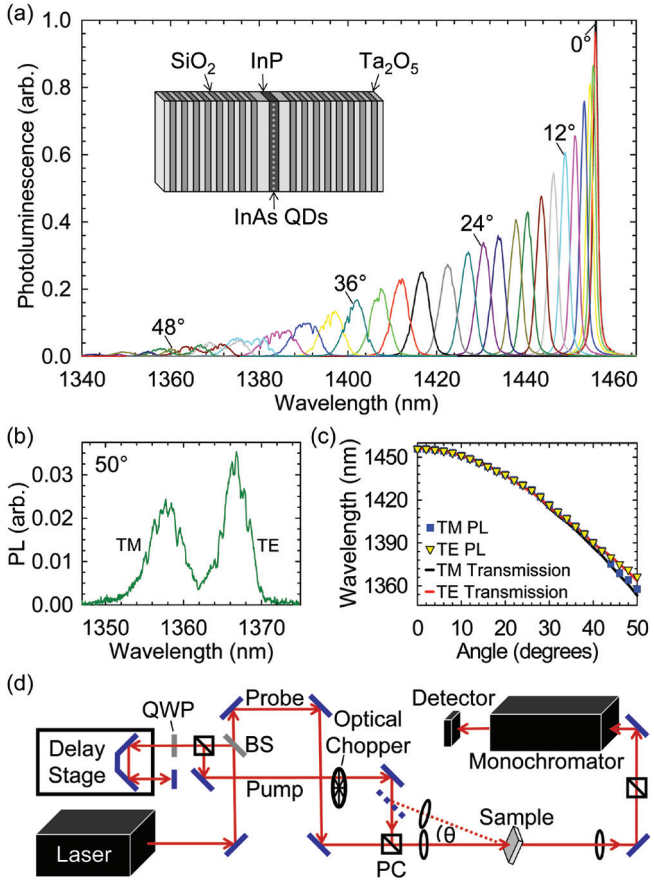

Figure 6.1: (a) QD photoluminescence as a function of detection angle relative to the sample normal. The rapid decay of the PL emission strength is due to the reduced spontaneous emission rate for large angles in a 1D λ microcavity [32]. Inset: Schematic diagram of the sample structure. (b) PL emission with resolved polarization modes at a detection angle of 50 degrees. (c) Angle-resolved peak cavity transmission (curves) and PL (symbols) with TE (triangles) and TM (squares) mode dispersion. (d) Schematic diagram of the differential transmission experimental appartus. A polarizing beam splitter cube (PC) and quarter-wave plate (QWP) change the pump beam polarization from TM to TE. Another PC is placed before the monochromator to block the pump beam and transmit the TM polarized probe.

parametric oscillator and a single channel InGaAs photodetector was used in conjunction with the same monochromator to measure the transmitted spectrum. The microcavity mode at normal incidence is centered at 851 meV, with a linewidth from transmission measurements of 550 μeV. The linewidths of the PL peaks are $\sim$200 μeV wider than the measured transmission spectra due the finite angular resolution of the PL apparatus. The TE mode shifts by 65 meV between 0 degrees and 50 degrees, as seen in Fig. 6.1(c). The

PL splitting between TE and TM modes is clearly resolved at large angles, equal to 6 meV at 50 degrees.

Due to the high finesse of the microcavity, optical pulses tuned to the ground state optical transition of the QD ensemble will only excite QDs for which the exciton transition energy is in resonance with the microcavity mode. The microcavity therefore provides a means to selectively address a subset of QDs with a substantially-reduced variance in the exciton transition energy (determined by the microcavity mode linewidth rather than the inhomogeneous width of the ground state transition for the full ensemble (50 meV)). Here we verify this selectivity by performing pump-probe differential transmission experiments with pump and probe beams that are either collinear (exciting and detecting the same QD subset) or non-collinear (exciting and detecting different subsets). The apparatus used for these experiments is shown schematically in Fig. 6.1(d). The optical source was a 250 kHz optical parametric amplifier producing 130 fs pulses (70 nm bandwidth) tuned to the cavity mode. A rotary stage was used to control the angle of the probe beam relative to the sample normal, and the angle between the pump and probe beams was either 0 degrees (collinear geometry) or 12 degrees (non-collinear geometry). The differential transmission signal was spectrally resolved using a 0.25 m monochromator and detected using a single channel InGaAs photodiode and lock-in techniques. All experiments were carried out with the sample at room temperature.

Results of differential transmission measurements for collinear pump and probe beams at normal incidence are shown in Fig. 6.2(a). The contour plot indicates the pump-induced change in transmission ($\Delta T \equiv T - T_0$) as a function of the time delay between the pump and probe pulses and the probe detection wavelength, where T_0 (T) is the transmission of the probe pulse in the absence (presence) of the pump pulse. The overlaid plots indicate T_0 (dashed curve) and T at 10 ps delay (solid curve). The dominant influence of the pump pulse is an increase in the transmission of approximately 10% at the peak of the microcavity mode. We attribute this to state filling of excitons in QDs resonant with the microcavity mode, consistent with the slow decay of the bleaching signal (Fig. 6.2(b)). The microcavity mode is also red shifted (tied to a transient increase in the index of refraction) by an amount that is barely detectable within the spectral resolution of the pump-probe apparatus. These general features are reproduced in the collinear differential transmission results for angles of incidence of 4 and 12 degrees (Fig. 6.2(c),(d)). The state-filling signal

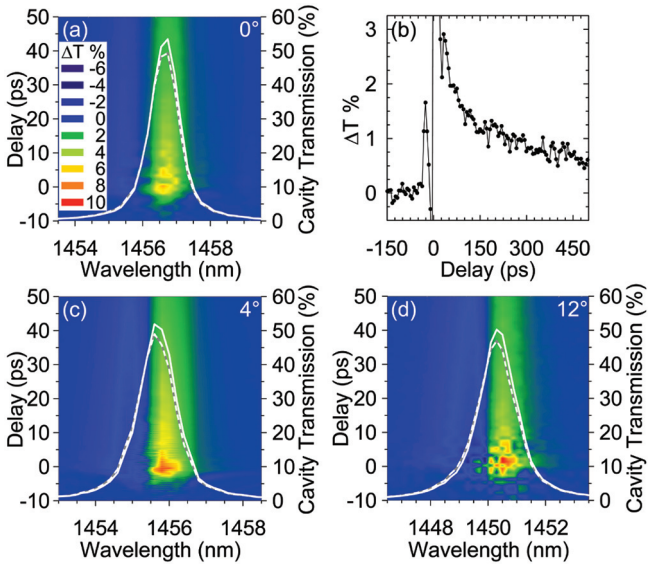

Figure 6.2: (a) Results of spectrally-resolved collinear differential transmission experiments at normal incidence, showing ΔT versus probe detection wavelength and probe pulse delay. Overlay: T_0 (dashed curve); T at a probe pulse delay of 10 ps (solid curve). The average power in the pump beam is 7 mW, corresponding to a pulse fluence of 400 μJ/cm^{-2}. Power-dependent experiments (data not shown) indicate that ΔT is proportional to the average pump beam power, verifying that the experiments are carried out within the χ^3 regime. (b) Differential transmission signal at normal incidence, averaged over the linewidth of the microcavity mode. (c)((d)) Same as (a), but with incident angles of 4 (12) degrees. The absolute magnitude of the differential transmission response for different incident angles reflects conditions of equal absorbed power taking into account measured variations of transmissivity and reflectivity with incident angle.

tracks the wavelength shifts of the microcavity mode with angle, reflecting pump excitation of QDs with increasing exciton resonance energies.

Differential transmission measurements were also performed with the pump pulse at normal incidence and the probe pulse at 12 degrees. In this configuration, the pump and probe beams are addressing QDs with exciton transition energies approximately 4 meV apart, much larger than the 550 μeV width of the microcavity mode. The results of these experiments are shown in Fig. 6.3(a). The large state filling signal in Fig. 6.2(d) for collinear excitation conditions is suppressed in the non-collinear results in Fig. 6.3(a), demonstrating the angle-selectivity of excitation and detection via the microcavity mode.

The shift in the mode observed in the collinear excitation geometry persists in the non-collinear results of Fig. 6.3(a), although with a smaller magnitude. This shift decays on

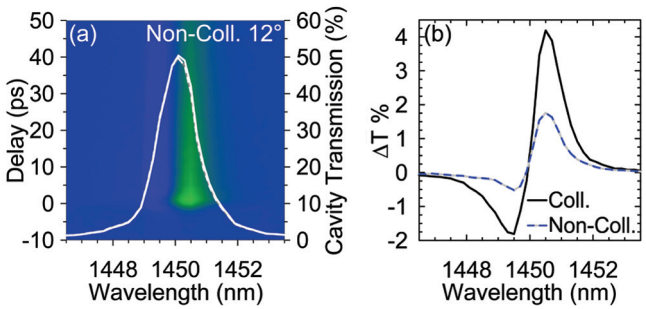

Figure 6.3: (a) Results of pump-probe differential transmission experiments in the non-collinear excitation geometry. The contour scale and line plots are the same as in Fig. 6.2. (b) ΔT at 10 ps for the collinear (Fig. 6.2(d)) and non-collinear pump-probe geometries. In both cases, the probe beam is incident at 12 degrees.

the same time scale as the bleaching response for collinear excitation and is therefore tied to excited QDs within the structure. For an isolated optical resonance, a nonlinear index of refraction extends over a larger energy range than the corresponding nonlinear bleaching signal, a feature that is useful for non-destructive quantum state readout [41]. Together with the relatively low spectral resolution of the pump-probe apparatus, this suggests that the residual shift detected in the mode centered at 855 meV in Fig. 6.3(a) may be tied to a transient refractive index response associated with the resonantly excited quantum dots at 851 meV. The mode shift dominates the nonlinear response in the non-collinear case (Fig. 6.3(b)), but a small bleaching component persists (6$\times$ smaller than in Fig. 6.2(d)). This suggests that a small fraction of the QDs centered at 855 meV may have been excited indirectly, possibly through carrier escape and recapture into other quantum dots assisted by wetting layer transitions [142, 143]. One could diminish these effects by working at lower temperatures.

The reduced variance of the exciton transition energy (or the trion transition energy for a similar structure containing charged QDs [40, 52, 54, 61]) enabled by the microcavity mode improves the prospect of high fidelity optical control for a qubit stored in the quantum dot ensemble. For excitons, ultrafast single qubit gates are carried out using Rabi rotations [42, 43, 44, 45, 57], together with phase control via the optical Stark effect [131, 132]. For single carrier spin qubits, full control is possible using stimulated Raman transitions [29, 40, 54, 61, 144], for which the pulse center frequency and area must be carefully selected to ensure that optical control is unitary within the single-spin subspace.

Inhomogeneities in the resonance energy and dipole moment of the associated optical transition (exciton or trion) have been shown to limit the fidelity of optical control using the above approaches in QD ensembles [29, 57, 144]. Since the microcavity will lead to a substantial reduction in the variance of both the exciton transition energy and dipole moment (as they are both tied to variations in the quantum dot size [144, 145]), these deleterious effects of inhomogeneity on the fidelity of optical control will be reduced considerably. We note that controlled detuning of the optical gate pulse relative to the exciton transition could be achieved for qubits encoded using the structure considered here by exploiting the angle dependence of the microcavity mode energy.

Mode-locking of spin precession using periodic laser excitation [60, 136, 137, 146] provides an alternative approach to mitigating inhomogeneity for qubit storage in an ensemble of quantum dots. The mode-locking process reduces the influence of variations in the g-factor and the effective magnetic field associated with the nuclei, leading to a dramatic enhancement of the ensemble spin dephasing time [60]. The fidelity of optical control of such spin qubits is nevertheless limited by inhomogeneities in the transition energy and dipole moment [29], in contrast to the approach considered here.

In summary, we have applied pump-probe differential transmission experiments to investigate the utility of a one-dimensional optical microcavity for reducing the deleterious effects of inhomogeneity on the storage and manipulation of qubits in ensembles of semiconductor QDs. Our results indicate that the microcavity mode enables the selective excitation and detection of subsets of QDs that could be used for qubit encoding. The substantial reduction in the variance of the dipole moments and transition energies for the selected subset will further the objective of high-fidelity optical quantum gates on ensembles while drastically reducing the technical challenge associated with quantum state readout relative to qubits encoded in individual quantum dots. The angle-dependent resonance energy of the microcavity mode would in principle permit storage of several qubits in different quantum dot subsets, the number of which being determined by the details of the implementation. The expected improvement in fidelity of single-qubit gates enabled by the microcavity mode would also facilitate the implementation of decoherence mitigation [27, 99, 100] for ensemble qubits in the structure considered here.

6.2.1 Acknowledgments

This research is supported by the Natural Sciences and Engineering Research Council of Canada and Lockheed Martin Corporation.

CHAPTER 7

CONCLUSIONS AND OUTLOOK

The three research projects that constitute this thesis work have made substantial advances in the control of fundamental quantum excitations in semiconductor QDs using ultrafast optical techniques. The development of the necessary experimental apparatus and techniques for implementing coherent optical control using engineered optical pulses at telecommunications wavelengths has built upon the past success of femtosecond pulse shaping in atomic and molecular systems and laid the foundation for the extension of such techniques to solid state systems. The application of these newly developed methods to the first experimental realization of optimal quantum control in semiconductor QDs and the first demonstration of parallel qubit gates on distant QDs are important stepping stones on the path to achieving a functional quantum simulator based on this promising system. The exploration of alternative means of encoding qubits using fundamental quantum states in ensembles of QDs compliments the single QD experiments in this thesis work and provides a direction for simplifying quantum state read-out. All of these advances will further the long-term objective of realizing a scalable semiconductor-based solid state quantum computing platform.

In the first component of this work, a quantum control apparatus designed to operate in the infrared was constructed and tested. As a test case for this apparatus, ultrafast pulses engineered to carry out a C-ROT operation on two excitons in a single QD were generated and characterized using MIIPS and autocorrelation techniques. Phase-only and amplitude-only shaping masks, designed for high-fidelity C-ROT operations on single InAs QDs were applied to TL pulses using the SLM within the pulse shaper. The phase-shaped pulses conserved optical pulse power at the expense of increasing the pulse duration from

130 fs to approximately 2 ps. The amplitude shaping scheme resulted in shorter pulse durations compared to the phase shaped pulses; however, the amplitude masks applied by the SLM resulted in low optical power at the pulse shaper output. These first experiments demonstrated the high accuracy of pulse shapes implemented by this new apparatus despite the incorporation of diffraction-limited focusing and a sample in a cryogenic environment, illustrating its applicability for quantum control experiments on solid state qubits.

A natural step forward from the first part of this thesis work was to implement optimized pulse shapes in quantum control experiments on individual semiconductor QDs. The versatility of femtosecond pulse shaping protocols was showcased in the execution of parallel single qubit gates on exciton qubits in two distant, uncoupled InAs QDs. The InAs QDs used in these experiments have ground state emission wavelengths of 1.3 μm at 10 K, and were spatially and spectrally isolated from the QD ensemble. Phase-only pulse shaping, using a cosine phase mask function, yielded high fidelity optimal quantum control of both QDs simultaneously, performing concurrent π and 2π rotations. By shifting the cosine phase mask by an amount approximately equal to the energy separation between the exciton transitions in each QD, the reverse operation was achieved, solidifying an interpretation based on combined Rabi rotations and adiabatic rapid passage as the mechanism for control. By implementing a high resolution shaping system (*e.g.*, using a 640 pixel SLM and appropriate diffraction grating), one could extend this approach to control numerous uncoupled QDs within the laser focal spot. For this first demonstration of pulse shaping for optimal quantum control in semiconductor QDs, a simple cosine function was used. In future work, one could incorporate more complex functions into the control scheme for more flexibility in optimizing quantum gates.

In all single QD investigations, execution of high signal-to-noise measurements is a challenge due to the small optical signal generated by an individual QD. This can be overcome by using ensembles of QDs in optical experiments as the larger optical signal greatly facilitates quantum state read-out. When working with QD ensembles, the inhomogeneous size distribution within the population of QDs must be addressed. This size distribution, inherent to the self-assembled growth of semiconductor QDs, leads to variations in transition energy, dipole moment, and g-factor for different QDs within the ensemble, which severely restricts the fidelity of optical gates on ensemble qubits. In an effort to mitigate these challenges, in the third project of this thesis, a planar microcavity,

containing an ensemble of InAs/InP QDs was studied. The transmission wavelength of one-dimensional microcavities varies with the angle of the light incident on the cavity. Angle-resolved PL and differential-transmission measurements revealed that energetic subsets of QDs within the ensemble can be selectively addressed using angle-dependent excitation. The dramatic reduction in the variance of the exciton transition energy and dipole moment enabled by the microcavity will improve the prospect of achieving high fidelity optically-mediated gates in this system. These results also suggest that the angle dependent resonance of the microcavity could be used for off-resonant gates using the Stark effect, and that multiple qubits could be encoded in distinct QD subsets.

This thesis work has laid the foundation for the application of optimal quantum control to optimizing other optical quantum gates in semiconductor QDs. For example, the progress made here involving parallel single qubit gates could be extended to a two-qubit C-ROT gate and could form a starting point for developing a small quantum simulator using complex instruction set quantum computing. In addition, the control of exciton states in semiconductor QDs was the focus of this thesis work due to the relative simplicity of optical control in this case. However, the general approach developed here could be extended next to spin based qubits. In particular, hole spins have received considerable attention recently due to the lower influence of hyperfine coupling to the lattice nuclei, which leads to longer coherence lifetimes. The possible use of hole spin qubits for storage and exciton qubits for computation would marry the benefits of the long spin lifetime in the former case and the ease of optical control in the latter case. The optimized approach developed here for single qubit gates involving excitons would find natural application in such a hybrid computing platform in the realization of dynamical decoupling approaches for extending the exciton coherence lifetime during the idle stages of a computation. The utility of dynamical decoupling for exciton qubits had been highlighted in several recent theoretical works, but has not yet been experimentally demonstrated. Optimal quantum control for parallel qubit gates, as demonstrated here, could ultimately be realized in optical microcavity structures, in which one could exploit the microcavity modes for long-range entanglement between qubits.

Among the various physical platforms being pursued for the development of a scalable quantum computer, N-V centers in diamond provide an attractive solid state alternative to

the approach considered in this thesis work. Although semiconductor QDs offer considerable advantages over N-V centers, such as the compatibility with existing computing technology and the exploitation of semiconductor and photonic device fabrication capabilities, the breathtaking pace of advances in optical control of qubits in QDs in recent years has been paralleled by advances in the optical control of qubits in diamond. The successful realization of either (or both) of these technologies would have wide-ranging implications for society. The next decade will undoubtedly witness great strides in the fundamental understanding and control of quantum systems.

BIBLIOGRAPHY

[1] P. W. Shor. Algorithms for quantum computation: Discrete logarithms and factoring. In *Annual Symposium on Foundations of Computer Science*, volume 35, pages 124–134. Citeseer, 1994.

[2] L. K. Grover. Quantum mechanics helps in searching for a needle in a stack. *Phys. Rev. Lett.*, 79(2):325–328, Jul 1997.

[3] L. M. K. Vandersypen, M. Steffen, G. Breyta, C. S. Yannoni, M. H. Sherwood, and I. L. Chuang. Experimental realization of Shor's quantum factoring algorithm using nuclear magnetic resonance. *Nature*, 414:883–887, 2001.

[4] Z. Amitay, R. Kosloff, and S. R. Leone. Experimental coherent computation of a multiple-input AND gate using pure molecular superpositions. *Chem. Phys. Lett.*, 359:8–14, 2002.

[5] P. Bianucci, A. Muller, C. K. Shih, Q. Q. Wang, Q. K. Xue, and C. Piermarocchi. Experimental realization of the one qubit Deutsch-Jozsa algorithm in a quantum dot. *Phys. Rev. B*, 69:161303, Apr 2004.

[6] David P. DiVincenzo. The physical implementation of quantum computation. *Fortschritte der Physik*, 48(9-11):771–783, 2000.

[7] David P. DiVincenzo. Two-bit gates are universal for quantum computation. *Phys. Rev. A*, 51:1015–1022, Feb 1995.

[8] M. A. Nielsen and I. L. Chuang. *Quantum Computation and Quantum Information*. Cambridge University Press, Cambridge, 2000.

[9] G. D. Sanders, K. W. Kim, and W. C. Holton. Quantum computing with complex instruction sets. *Phys. Rev. A*, 59:1098–1101, 1999.

[10] Y. Masumoto and T. Takagahara. *Semiconductor Quantum Dots*. Springer-Verlag, Berlin, 2002.

[11] Pallab Bhattacharya, David Klotzkin, O. Qasaimeh, Weidong Zhou, S. Krishna, and Donghai Zhu. High-speed modulation and switching characteristics of In(Ga)As-Al(Ga)As self-organized quantum-dot lasers. *Selected Topics in Quantum Electronics, IEEE Journal of*, 6(3):426–438, 2000.

[12] D. Sridharan and E. Waks. All-optical switch using quantum-dot saturable absorbers in a DBR microcavity. *Quantum Electronics, IEEE Journal of*, 47(1):31–39, 2011.

[13] Andrew M. Smith, Hongwei Duan, Aaron M. Mohs, and Shuming Nie. Bioconjugated quantum dots for in vivo molecular and cellular imaging. *Advanced Drug Delivery Reviews*, 60(11):1226 – 1240, 2008.

[14] P. Y. Yu and M. Cardona. *Fundamentals of Semiconductors*. Springer, Berlin, 2005.

[15] D. Gammon, E. S. Snow, B. V. Shanabrook, D. S. Katzer, and D. Park. Fine structure splitting in the optical spectra of single GaAs quantum dots. *Phys. Rev. Lett.*, 76:3005–3008, Apr 1996.

[16] J. R. Guest, T. H. Stievater, Xiaoqin Li, Jun Cheng, D. G. Steel, D. Gammon, D. S. Katzer, D. Park, C. Ell, A. Thränhardt, G. Khitrova, and H. M. Gibbs. Measurement of optical absorption by a single quantum dot exciton. *Phys. Rev. B*, 65:241310, Jun 2002.

[17] H. Heidemeyer, U. Denker, C. Müller, and O. G. Schmidt. Morphology response to strain field interferences in stacks of highly ordered quantum dot arrays. *Phys. Rev. Lett.*, 91:196103, Nov 2003.

[18] Y. B. Bolkhovityanov and O. P. Pchelyakov. GaAs epitaxy on Si substrates: modern status of research and engineering. *Phys.-Usp.*, 51:437, 2008.

[19] D. Loss and D. P. DiVincenzo. Quantum computation with quantum dots. *Phys. Rev. A*, 57(1):120–126, Jan 1998.

[20] A. Imamoğlu, D. D. Awschalom, G. Burkard, D. P. DiVincenzo, D. Loss, M. Sherwin, and A. Small. Quantum information processing using quantum dot spins and cavity QED. *Phys. Rev. Lett.*, 83(20):4204–4207, Nov 1999.

[21] F. Troiani, U. Hohenester, and E. Molinari. Exploiting exciton-exciton interactions in semiconductor quantum dots for quantum-information processing. *Phys. Rev. B*, 62(4):R2263–R2266, Jul 2000.

[22] P. Chen, C. Piermarocchi, and L. J. Sham. Control of exciton dynamics in nanodots for quantum operations. *Phys. Rev. Lett.*, 87(6):067401, Jul 2001.

[23] C. Piermarocchi, P. Chen, L. J. Sham, and D. G. Steel. Optical RKKY interaction between charged semiconductor quantum dots. *Phys. Rev. Lett.*, 89(16):167402, Sep 2002.

[24] P. Chen, C. Piermarocchi, L. J. Sham, D. Gammon, and D. G. Steel. Theory of quantum optical control of a single spin in a quantum dot. *Phys. Rev. B*, 69(7):075320, Feb 2004.

[25] S. E. Economou, L. J. Sham, Y. Wu, and D. G. Steel. Proposal for optical U(1) rotations of electron spin trapped in a quantum dot. *Phys. Rev. B*, 74(20):205415, Nov 2006.

[26] S. M. Clark, K.-M. C. Fu, T. D. Ladd, and Y. Yamamoto. Quantum computers based on electron spins controlled by ultrafast off-resonant single optical pulses. *Phys. Rev. Lett.*, 99(4):040501, Jul 2007.

[27] T. E. Hodgson, L. Viola, and I. D'Amico. Decoherence-protected storage of exciton qubits through ultrafast multipulse control. *Phys. Rev. B*, 78:165311, Oct 2008.

[28] X. Li, Y. Wu, D. Steel, D. Gammon, T. H. Stievater, D. S. Katzer, D. Park, C. Piermarocchi, and L. J. Sham. An all-optical quantum gate in a semiconductor quantum dot. *Science*, 301(5634):809–811, 2003.

[29] A. Greilich, Sophia E. Economou, S. Spatzek, D. R. Yakovlev, D. Reuter, A. D. Wieck, T. L. Reinecke, and M. Bayer. Ultrafast optical rotations of electron spins in quantum dots. *Nat. Phys.*, 5(4):262–266, 2009.

[30] C.-M. Simon, T. Belhadj, B. Chatel, T. Amand, P. Renucci, A. Lemaitre, O. Krebs, P. A. Dalgarno, R. J. Warburton, X. Marie, and B. Urbaszek. Robust quantum dot exciton generation via adiabatic passage with frequency-swept optical pulses. *Phys. Rev. Lett.*, 106:166801, Apr 2011.

[31] D. Dalacu, D. Poitras, J. Lefebvre, P. J. Poole, G. C. Aers, and R. L. Williams. InAs/InP quantum dots in $\mathrm{Si_2/Ta_2O_5}$ - based microcavities. *Applied Physics Letters*, 82(26):4803–4805, 2003.

[32] C.C. Lin, D.G. Deppe, and C. Lei. Role of waveguide light emission in planar microcavities. *Quantum Electronics, IEEE Journal of*, 30(10):2304–2313, 1994.

[33] Q. Deng and D. Deppe. Spontaneous lifetime in a dielectrically-apertured Fabry-Perot microcavity. *Opt. Express*, 2(4):157–162, Feb 1998.

[34] K. Hennessy, A. Badolato, M. Winger, D. Gerace, M. Atature, S. Gulde, S. Falt, E. L. Hu, and A. Imamoğlu. Quantum nature of a strongly coupled single quantum dot-cavity system. *Nature*, 445:896–899, 2007.

[35] D. K. Armani, T. J. Kippenberg, S. M. Spillane, and K. J. Vahala. Ultra-high-Q toroid microcavity on a chip. *Nature*, 421:925–925, 2003.

[36] J. Preskill. Fault-tolerant quantum computation. *Introduction to quantum computation and information*, pages 213–269, 1998.

[37] P. Borri, W. Langbein, S. Schneider, U. Woggon, R. L. Sellin, D. Ouyang, and D. Bimberg. Ultralong dephasing time in InGaAs quantum dots. *Phys. Rev. Lett.*, 87(15):157401, Sep 2001.

[38] M. Kroutvar, Y. Ducommun, D. Heiss, M. Bichler, D. Schuh, G. Abstreiter, and J. J. Finley. Optically programmable electron spin memory using semiconductor quantum dots. *Nature*, 432(7013):81–84, 2004.

[39] N. H. Bonadeo, J. Erland, D. Gammon, D. Park, D. S. Katzer, and D. G. Steel. Coherent optical control of the quantum state of a single quantum dot. *Science*, 282(5393):1473–1476, 1998.

[40] J. Berezovsky, M. H. Mikkelsen, N. G. Stoltz, L. A. Coldren, and D. D. Awschalom. Picosecond coherent optical manipulation of a single electron spin in a quantum dot. *Science*, 320(5874):349–352, 2008.

[41] M. H. Mikkelsen, J. Berezovsky, N. G. Stoltz, L. A. Coldren, and D. D. Awschalom. Optically detected coherent spin dynamics of a single electron in a quantum dot. *Nat. Phys.*, 3(11):770–773, 2007.

[42] T. H. Stievater, X. Li, D. G. Steel, D. Gammon, D. S. Katzer, D. Park, C. Piermarocchi, and L. J. Sham. Rabi oscillations of excitons in single quantum dots. *Phys. Rev. Lett.*, 87(13):133603, Sep 2001.

[43] H. Kamada, H. Gotoh, J. Temmyo, T. Takagahara, and H. Ando. Exciton Rabi oscillation in a single quantum dot. *Phys. Rev. Lett.*, 87:246401, Nov 2001.

[44] A. Zrenner, E. Beham, S. Stufler, F. Findeis, M. Bichler, and Abstreiter G. Coherent properties of a two-level system based on a quantum-dot photodiode. *Nature*, 418(6898):612, 2002.

[45] H. Htoon, T. Takagahara, D. Kulik, O. Baklenov, A. L. Holmes, and C. K. Shih. Interplay of Rabi oscillations and quantum interference in semiconductor quantum dots. *Phys. Rev. Lett.*, 88:087401, Feb 2002.

[46] Q. Q. Wang, A. Muller, P. Bianucci, E. Rossi, Q. K. Xue, T. Takagahara, C. Piermarocchi, A. H. MacDonald, and C. K. Shih. Decoherence processes during optical manipulation of excitonic qubits in semiconductor quantum dots. *Phys. Rev. B*, 72:035306, Jul 2005.

[47] Q. Q. Wang, A. Muller, M. T. Cheng, H. J. Zhou, P. Bianucci, and C. K. Shih. Coherent control of a V-type three-level system in a single quantum dot. *Phys. Rev. Lett.*, 95(18):187404, Oct 2005.

[48] T. F. Boggess, L. Zhang, D. G. Deppe, D. L. Huffaker, and C. Cao. Spectral engineering of carrier dynamics in In(Ga)As self-assembled quantum dots. *Applied Physics Letters*, 78(3):276–278, 2001.

[49] T. Flissikowski, A. Betke, I. A. Akimov, and F. Henneberger. Two-photon coherent control of a single quantum dot. *Phys. Rev. Lett.*, 92:227401, Jun 2004.

[50] S. Stufler, P. Machnikowski, P. Ester, M. Bichler, V. M. Axt, T. Kuhn, and A. Zrenner. Two-photon Rabi oscillations in a single $\mathrm{In}_x\mathrm{Ga}_{1-x}\mathrm{As}/\mathrm{GaAs}$ quantum dot. *Phys. Rev. B*, 73:125304, Mar 2006.

[51] Y. Wu, I. M. Piper, M. Ediger, P. Brereton, E. R. Schmidgall, P. R. Eastham, M. Hugues, M. Hopkinson, and R. T. Phillips. Population inversion in a single InGaAs quantum dot using the method of adiabatic rapid passage. *Phys. Rev. Lett.*, 106:067401, Feb 2011.

[52] B. D. Gerardot, D. Brunner, P. A. Dalgarno, P. Ohberg, S. Seidl, M. Kroner, K. Karrai, N. G. Stoltz, P. M. Petroff, and R. J. Warburton. Optical pumping of a single hole spin in a quantum dot. *Nature*, 451(7177):441, 2008.

[53] Mete Atatüre, Jan Dreiser, Antonio Badolato, Alexander Hgele, Khaled Karrai, and Atac Imamoğlu. Quantum-dot spin-state preparation with near-unity fidelity. *Science*, 312(5773):551–553, 2006.

[54] D. Press, T. D. Ladd, B. Zhang, and Y. Yamamoto. Complete quantum control of a single quantum dot spin using ultrafast optical pulses. *Nature*, 456(7219):218, 2008.

[55] Erik D. Kim, Katherine Truex, Xiaodong Xu, Bo Sun, D. G. Steel, A. S. Bracker, D. Gammon, and L. J. Sham. Fast spin rotations by optically controlled geometric phases in a charge-tunable InAs quantum dot. *Phys. Rev. Lett.*, 104:167401, Apr 2010.

[56] A. S. Lenihan, M. V. Gurudev Dutt, D. G. Steel, S. Ghosh, and P. K. Bhattacharya. Raman coherence beats from entangled polarization eigenstates in InAs quantum dots. *Phys. Rev. Lett.*, 88(22):223601, May 2002.

[57] P. Borri, W. Langbein, S. Schneider, U. Woggon, R. L. Sellin, D. Ouyang, and D. Bimberg. Rabi oscillations in the excitonic ground-state transition of InGaAs quantum dots. *Phys. Rev. B*, 66:081306, Aug 2002.

[58] Mamiko Kujiraoka, Junko Ishi-Hayase, Kouichi Akahane, Naokatsu Yamamoto, Kazuhiro Ema, and Masahide Sasaki. Optical rabi oscillations in a quantum dot ensemble. *Applied Physics Express*, 3(9):092801, 2010.

[59] A. Greilich, R. Oulton, E. A. Zhukov, I. A. Yugova, D. R. Yakovlev, M. Bayer, A. Shabaev, Al. L. Efros, I. A. Merkulov, V. Stavarache, D. Reuter, and A. Wieck. Optical control of spin coherence in singly charged (In,Ga)As/GaAs quantum dots. *Phys. Rev. Lett.*, 96(22):227401, Jun 2006.

[60] A. Greilich, D. R. Yakovlev, A. Shabaev, Al. L. Efros, I. A. Yugova, R. Oulton, V. Stavarache, D. Reuter, A. Wieck, and M. Bayer. Mode locking of electron spin coherences in singly charged quantum dots. *Science*, 313(5785):341–345, 2006.

[61] Yanwen Wu, Erik D. Kim, Xiaodong Xu, Jun Cheng, D. G. Steel, A. S. Bracker, D. Gammon, Sophia E. Economou, and L. J. Sham. Selective optical control of electron spin coherence in singly charged GaAs-$Al_{0.3}Ga_{0.7}As$ quantum dots. *Phys. Rev. Lett.*, 99:097402, Aug 2007.

[62] A. Greilich, S. Spatzek, I. A. Yugova, I. A. Akimov, D. R. Yakovlev, Al. L. Efros, D. Reuter, A. D. Wieck, and M. Bayer. Collective single-mode precession of electron spins in an ensemble of singly charged (In,Ga)As/GaAs quantum dots. *Phys. Rev. B*, 79:201305, May 2009.

[63] W. C. Campbell, J. Mizrahi, Q. Quraishi, C. Senko, D. Hayes, D. Hucul, D.N. Matsukevich, P. Maunz, and Monroe C. Ultrafast gates for single atomic qubits. *Phys. Rev. Lett.*, 105:090502, 2010.

[64] G. Kirchmair, J. Benhelm, F. Zaehringer, R. Gerritsma, C. F. Roos, and R. Blatt. Deterministic entanglement of ions in thermal states of motion. *New Journal of Physics*, 11:023002, 2009.

[65] Doron M. and Yaron S. Coherent quantum control of two-photon transitions by a femtosecond laser pulse. *Nature*, 396(6708):239, 1998.

[66] S. Zhdanovich, E. A. Shapiro, M. Shapiro, J. W. Hepburn, and V. Milner. Population transfer between two quantum states by piecewise chirping of femtosecond pulses: Theory and experiment. *Phys. Rev. Lett.*, 100:103004, Mar 2008.

[67] B. Broers, H. B. van Linden van den Heuvell, and L. D. Noordam. Efficient population transfer in a three-level ladder system by frequency-swept ultrashort laser pulses. *Phys. Rev. Lett.*, 69:2062–2065, Oct 1992.

[68] B. Chatel, J. Degert, S. Stock, and B. Girard. Competition between sequential and direct paths in a two-photon transition. *Phys. Rev. A*, 68:041402, Oct 2003.

[69] J. S. Melinger, Suketu R. Gandhi, A. Hariharan, D. Goswami, and W. S. Warren. Adiabatic population transfer with frequency-swept laser pulses. *The Journal of Chemical Physics*, 101(8):6439–6454, 1994.

[70] P. Brumer and M. Shapiro. Laser control of molecular processes. *Annual Review of Physical Chemistry*, 43(1):257–282, 1992. PMID: 18397166.

[71] H. Rabitz, R. de Vivie-Riedle, M. Motzkus, and K. Kompa. Whither the future of controlling quantum phenomena? *Science*, 288(5467):824–828, 2000.

[72] R. Bartels, S. Backus, E. Zeek, L. Misoguti, G. Vdovin, I. P. Christov, M. M. Murnane, and H. C. Kapteyn. Shaped-pulse optimization of coherent emission of high-harmonic soft x-rays. *Nature*, 406:164–166, 2000.

[73] D. Pestov, R. K. Murawski, G. O. Ariunbold, X. Wang, M. Zhi, A. V. Sokolov, V. A. Sautenkov, Y. V. Rostovtsev, A. Dogariu, Y. Huang, and M. O. Scully. Optimizing the laser-pulse configuration for coherent Raman spectroscopy. *Science*, 316:265–268, 2007.

[74] T. Rickes, J. P. Marangos, and T. Halfmann. Enhancement of third-harmonic generation by Stark-chirped rapid adiabatic passage. *Opt. Comm.*, 227:133–142, 2003.

[75] O. Madelung. *Semiconductors: Data Handbook*. Springer Verlag, 2004.

[76] P.M. Koenraad, D.M. Bruls, J.H. Davies, S.P.A. Gill, Fei Long, M. Hopkinson, M. Skolnick, and J.H. Wolter. Composition profiling at the atomic scale in III-V nanostructures by cross-sectional STM. *Physica E: Low-dimensional Systems and Nanostructures*, 17(0):526 – 532, 2003. Proceedings of the International Conference on Superlattices, Nano-structures and Nano-devices ICSNN 2002.

[77] F. Meier and B. P. Zakharchenya. Optical orientation, Modern problems in condensed matter sciences, Vol. 8, 1984.

[78] P. W. Milonni and J. H. Eberly. *Lasers*. New York: Wiley-Interscience Publication, 1988.

[79] R. S. Kolodka, A. J. Ramsay, J. Skiba-Szymanska, P. W. Fry, H. Y. Liu, A. M. Fox, and M. S. Skolnick. Inversion recovery of single quantum-dot exciton based qubit. *Phys. Rev. B*, 75:193306, May 2007.

[80] Y. Wu, X. Li, L. M. Duan, D. G. Steel, and D. Gammon. Density matrix tomography through sequential coherent optical rotations of an exciton qubit in a single quantum dot. *Phys. Rev. Lett.*, 96:087402, Feb 2006.

[81] A. M. Weiner. Femtosecond pulse shaping using spatial light modulators. *Review of Scientific Instruments*, 71(5):1929–1960, 2000.

[82] Andrew M. Weiner. *Ultrafast Optics*. John Wiley & Sons, Inc., 2008.

[83] R. Mathew, C. E. Pryor, M. E. Flatté, and K. C. Hall. Optimal quantum control for conditional rotation of exciton qubits in semiconductor quantum dots. *Phys. Rev. B*, 84:205322, Nov 2011.

[84] A. Gamouras, R. Mathew, and K. C. Hall. Optically engineered ultrafast pulses for controlled rotations of exciton qubits in semiconductor quantum dots. *J. Appl. Phys.*, 112:014313, 2012.

[85] Frank L. Pedrotti, Leno S. Pedrotti, and Leno M. Pedrotti. *Introduction to Optics, Third Ed.* Pearson Prentice Hall, 2007.

[86] V. V. Lozovoy, I. Pastirk, and M. Dantus. Multiphoton intrapulse interference. IV. ultrashort laserpulse spectral phase characterization and compensation. *Opt. Lett.*, 29(7):775–777, Apr 2004.

[87] B. Xu, J. M. Gunn, J. M. Dela Cruz, V. V. Lozovoy, and M. Dantus. Quantitative investigation of the multiphoton intrapulse interference phase scan method for simultaneous phase measurement and compensation of femtosecond laser pulses. *J. Opt. Soc. Am. B*, 23(4):750–759, Apr 2006.

[88] W. Kaiser. *Ultrashort Laser Pulses*. Springer-Verlag, Berlin, 1988.

[89] E. Biolatti, R. C. Iotti, P. Zanardi, and F. Rossi. Quantum information processing with semiconductor macroatoms. *Phys. Rev. Lett.*, 85:5647–5650, Dec 2000.

[90] J. H. Reina, L. Quiroga, and N. F. Johnson. Quantum entanglement and information processing via excitons in optically driven quantum dots. *Phys. Rev. A*, 62:012305, Jun 2000.

[91] C. Piermarocchi, P. Chen, Y. S. Dale, and L. J. Sham. Theory of fast quantum control of exciton dynamics in semiconductor quantum dots. *Phys. Rev. B*, 65:075307, Jan 2002.

[92] F. Troiani, E. Molinari, and U. Hohenester. High-finesse optical quantum gates for electron spins in artificial molecules. *Phys. Rev. Lett.*, 90:206802, May 2003.

[93] T. A. Brun and H. Wang. Coupling nanocrystals to a high-Q silica microsphere: Entanglement in quantum dots via photon exchange. *Phys. Rev. A*, 61:032307, Feb 2000.

[94] L. Quiroga and N. F. Johnson. Entangled Bell and Greenberger-Horne-Zeilinger states of excitons in coupled quantum dots. *Phys. Rev. Lett.*, 83:2270–2273, Sep 1999.

[95] S. J. Boyle, A. J. Ramsay, F. Bello, H. Y. Liu, M. Hopkinson, A. M. Fox, and M. S. Skolnick. Two-qubit conditional quantum-logic operation in a single self-assembled quantum dot. *Phys. Rev. B*, 78:075301, Aug 2008.

[96] G. Chen, N. H. Bonadeo, D. G. Steel, D. Gammon, D. S. Katzer, D. Park, and L. J. Sham. Optically induced entanglement of excitons in a single quantum dot. *Science*, 289(5486):1906–1909, 2000.

[97] G. Chen, T. H. Stievater, E. T. Batteh, X. Li, D. G. Steel, D. Gammon, D. S. Katzer, D. Park, and L. J. Sham. Biexciton quantum coherence in a single quantum dot. *Phys. Rev. Lett.*, 88:117901, Mar 2002.

[98] H. Y. Hui and R. B. Liu. Proposal for geometric generation of a biexciton in a quantum dot using a chirped pulse. *Phys. Rev. B*, 78:155315, Oct 2008.

[99] P. Karbach, S. Pasini, and G. S. Uhrig. Numerical analysis of optimized coherent control pulses. *Phys. Rev. A*, 78:022315, Aug 2008.

[100] V. M. Axt, P. Machnikowski, and T. Kuhn. Reducing decoherence of the confined exciton state in a quantum dot by pulse-sequence control. *Phys. Rev. B*, 71:155305, Apr 2005.

[101] Commercial pulse shaper systems are available, for example, from Coherent Inc., Biophotonic Solutions Inc., and Fastlite. The system used in this work was custom designed and fabricated for the infrared spectral region by BioPhotonic Solutions Inc.

[102] K. L. Silverman, R. P. Mirin, S. T. Cundiff, and A. G. Norman. Direct measurement of polarization resolved transition dipole moment in InGaAs/GaAs quantum dots. *Applied Physics Letters*, 82(25):4552–4554, 2003.

[103] C. Dal Savio, K. Pierz, G. Ade, H.-U. Danzebrink, E.O. Göbel, and A. Hangleiter. Optical study of single InAs on $\mathrm{In_{0.12}Ga_{0.88}}$ as self-assembled quantum dots: biexciton binding energy dependence on the dots size. *Applied Physics B*, 84(1-2):317–322, 2006.

[104] A. J. Ramsay, T. M. Godden, S. J. Boyle, E. M. Gauger, A. Nazir, B. W. Lovett, A. M. Fox, and M. S. Skolnick. Phonon-induced Rabi-frequency renormalization of optically driven single $\mathrm{InGaAs/GaAs}$ quantum dots. *Phys. Rev. Lett.*, 105:177402, Oct 2010.

[105] The gate time for a given excitation pulse was determined by normalizing the intensity profile and determining the width of a normalized square pulse with the same total area.

[106] E. Peter, P. Senellart, D. Martrou, A. Lemaître, J. Hours, J. M. Gérard, and J. Bloch. Exciton-photon strong-coupling regime for a single quantum dot embedded in a microcavity. *Phys. Rev. Lett.*, 95:067401, Aug 2005.

[107] T. Yang, O. Shchekin, J. D. O'Brien, and D. G. Deppe. Room temperature, continuous-wave lasing near 1300 nm in microdisks with quantum dot active regions. *Electronics Letters*, 39(23):1657–8–, 2003.

[108] R. Trebino, K. W. DeLong, D. N. Fittinghoff, J. N. Sweetser, M. A. Krumbügel, B. A. Richman, and D. J. Kane. Measuring ultrashort laser pulses in the time-frequency domain using frequency-resolved optical gating. *Review of Scientific Instruments*, 68(9):3277–3295, 1997.

[109] C. Iaconis and I. A. Walmsley. Spectral phase interferometry for direct electric-field reconstruction of ultrashort optical pulses. *Opt. Lett.*, 23(10):792–794, May 1998.

[110] Calculations of autocorrelation and MIIPS traces were done by importing the measured laser spectrum into a commercial pulse shaping program, femtoPulse Master, purchased from Biophotonic Solutions Inc.

[111] Spatial chirp may be manifested in MIIPS as a difference in the amplitude of the signal for $\delta = 0$ to π and $\delta = \pi$ to $2\ \pi$, as seen for example in Fig. 4.7. These effects are likely tied to the sensitivity of the OPO mode profile to tuning, and were only observed occasionally.

[112] A. E. Siegman. *Lasers*. Sausalito: University Science Books, 1986.

[113] V. Ramakrishna and H. Rabitz. Relation between quantum computing and quantum controllability. *Phys. Rev. A*, 54:1715–1716, 1996.

[114] W. S. Zhu, J. Botina, and H. Rabitz. Rapidly convergent iteration methods for quantum-optimal control of population. *J. Chem. Phys.*, 108:1953–1963, 1998.

[115] R. J. Levis, G. M. Menkir, and H. Rabitz. Selective bond dissociation and rearrangement with optimally tailored, strong-field laser pulses. *Science*, 292:709–713, 2001.

[116] A. Assion, T. Baumert, M. Bergt, T. Brixner, B. Kiefer, V. Seyfried, M. Strehle, and G. Gerber. Control of chemical reactions by feedback-optimized phase-shaped femtosecond laser pulses. *Science*, 282:919–922, 1998.

[117] J. L. Herek, W. Wohlleben, R. J. Cogdell, D. Zeidler, and M. Motzkus. Quantum control of energy flow in light harvesting. *Nature*, 417:533–535, 2002.

[118] The reduced fidelity for control using the shifted mask in Fig. 5.3b relative to that in Fig. 5.2d is attributed to an approximate offset of 0.8 meV between the exciton in QD1 and the point where $\Phi''_M(\omega)$= 0.

[119] W. Langbein, P. Borri, U. Woggon, V. Stavarache, D. Reuter, and A. D. Wieck. Radiatively limited dephasing in InAs quantum dots. *Phys. Rev. B*, 70(3):033301, Jul 2004.

[120] T. van der Sar, Z. H. Wang, M. S. Blok, H. Bernien, T. H. Taminiau, D. M. Toyli, D. A. Lidar, D. D. Awschalom, Hanson R., and V. V. Dobrovitski. Decoherence-protected quantum gates for a hybrid solid state spin register. *Nature*, 484:82–86, 2012.

[121] M. P. A. Branderhorst, P. Londero, P. Wasylczyk, C. Brif, R. L. Kosut, H. Rabitz, and I. A. Walmsley. Coherent control of decoherence. *Science*, 320:638–643, 2008.

[122] D. Hayes, S. M. Clark, S. Debnath, D. Hucul, I. V. Inlek, K. W. Lee, Q. Quraishi, and C. Monroe. Coherent error suppression in multiqubit entangling gates. *Phys. Rev. Lett.*, 109:020503, Jul 2012.

[123] E. Poem, O. Kenneth, Y. Kodriano, Y. Benny, S. Khatsevich, J. E. Avron, and D. Gershoni. Optically induced rotation of an exciton spin in a semiconductor quantum dot. *Phys. Rev. Lett.*, 107:087401, Aug 2011.

[124] Kristiaan De Greve, Leo Yu, Peter L. McMahon, Jason S. Pelc, Chandra M. Natarajan, Na Young Kim, Eisuke Abe, Sebastian Maier, Christian Schneider, Martin Kamp, Sven Hofling, Robert H. Hadfield, Alfred Forchel, M. M. Fejer, and Yoshihisa Yamamoto. Quantum-dot spin-photon entanglement via frequency downconversion to telecom wavelength. *Nature*, 491:421–425, 2012.

[125] W. B. Gao, P. Fallahi, , E. Togan, J. Miguel-Sanchez, and A. Imamoğlu. Observation of entanglement between a quantum dot spin and a single photon. *Nature*, 491:426–430, 2012.

[126] H. Kamada, H. Ando, J. Temmyo, and T. Tamamura. Excited-state optical transitions of excitons and biexcitons in a single $In_xGa_{1-x}As$ quantum disk. *Phys. Rev. B*, 58:16243–16251, Dec 1998.

[127] I. M. Sobol. On the distribution of points in a cube and the approximate evaluation of integrals. *Computational mathematics and mathematical physics*, 7(4):86+, 1967.

[128] M. J. D. Powell. A direct search optimization method that models the objective and constraint functions by linear interpolation. In *Advances in optimization and numerical analysis: proceedings of the Sixth Workshop on Optimization and Numerical Analysis, Oaxaca, Mexico*, page 51. Kluwer Academic Pub, 1994.

[129] A. Muller, E. B. Flagg, P. Bianucci, X. Y. Wang, D. G. Deppe, W. Ma, J. Zhang, G. J. Salamo, M. Xiao, and C. K. Shih. Resonance fluorescence from a coherently driven semiconductor quantum dot in a cavity. *Phys. Rev. Lett.*, 99:187402, Nov 2007.

[130] H. Htoon, D. Kulik, O. Baklenov, A. L. Holmes, T. Takagahara, and C. K. Shih. Carrier relaxation and quantum decoherence of excited states in self-assembled quantum dots. *Phys. Rev. B*, 63:241303, Jun 2001.

[131] Thomas Unold, Kerstin Mueller, Christoph Lienau, Thomas Elsaesser, and Andreas D. Wieck. Optical Stark effect in a quantum dot: Ultrafast control of single exciton polarizations. *Phys. Rev. Lett.*, 92:157401, Apr 2004.

[132] S. Michaelis de Vasconcellos, S. Gordon, M. Bichler, M. Bichler, T. Meier, and A. Zrenner. Coherent control of a single exciton qubit by optoelectronic manipulation. *Nature Photonics*, 4:545–548, 2010.

[133] Erik D. Kim, Katherine Truex, Yanwen Wu, A. Amo, Xiaodong Xu, D. G. Steel, A. S. Bracker, D. Gammon, and L. J. Sham. Picosecond optical spectroscopy of a single negatively charged self-assembled InAs quantum dot. *Applied Physics Letters*, 97(11):113110, 2010.

[134] I. A. Yugova, I. Ya. Gerlovin, V. G. Davydov, I. V. Ignatiev, I. E. Kozin, H. W. Ren, M. Sugisaki, S. Sugou, and Y. Masumoto. Fine structure and spin quantum beats in inp quantum dots in a magnetic field. *Phys. Rev. B*, 66:235312, Dec 2002.

[135] M. V. Gurudev Dutt, Jun Cheng, Bo Li, Xiaodong Xu, Xiaoqin Li, P. R. Berman, D. G. Steel, A. S. Bracker, D. Gammon, Sophia E. Economou, Ren-Bao Liu, and L. J. Sham. Stimulated and spontaneous optical generation of electron spin coherence in charged GaAs quantum dots. *Phys. Rev. Lett.*, 94:227403, Jun 2005.

[136] S. Varwig, A. Schwan, D. Barmscheid, C. Müller, A. Greilich, I. A. Yugova, D. R. Yakovlev, D. Reuter, A. D. Wieck, and M. Bayer. Hole spin precession in a (In,Ga)As quantum dot ensemble: From resonant spin amplification to spin mode locking. *Phys. Rev. B*, 86:075321, Aug 2012.

[137] F. Fras, B. Eble, F. Bernardot, C. Testelin, M. Chamarro, A. Miard, and A. Lemaitre. Optical pumping and reversal of hole spin in inas/gaas quantum dots. *Applied Physics Letters*, 100(1):012104, 2012.

[138] R. V. Cherbunin, K. Flisinski, I. Ya. Gerlovin, I. V. Ignatiev, M. S. Kuznetsova, M. Yu. Petrov, D. R. Yakovlev, D. Reuter, A. D. Wieck, and M. Bayer. Resonant nuclear spin pumping in (In,Ga)As quantum dots. *Phys. Rev. B*, 84:041304, Jul 2011.

[139] Y. Mitsumori, A. Hasegawa, M. Sasaki, H. Maruki, and F. Minami. Local field effect on rabi oscillations of excitons localized to quantum islands in a single quantum well. *Phys. Rev. B*, 71:233305, Jun 2005.

[140] Thomas Moldaschl, Thomas Müller, Sebastian Golka, Wolfgang Parz, Gottfried Strasser, and Karl Unterrainer. Coherent control of ground state excitons in the nonlinear regime within an ensemble of self-assembled InAs quantum dots. *physica status solidi (c)*, 6(4):876–878, 2009.

[141] S. Reitzenstein. Semiconductor quantum dot - microcavities for quantum optics in solid state. *Selected Topics in Quantum Electronics, IEEE Journal of*, 18(6):1733–1746, 2012.

[142] T. B. Norris, K. Kim, J. Urayama, Z. K. Wu, J. Singh, and P. K. Bhattacharya. Density and temperature dependence of carrier dynamics in self-organized InGaAs quantum dots. *Journal of Physics D: Applied Physics*, 38(13):2077, 2005.

[143] We note that a weak background continuum absorption associated with the wetting layer may be present, but would result in a negligible nonlinear (state filling) signal in comparison to the resonantly pumped quantum dots.

[144] C. E. Pryor and M. E. Flatte. Predicted ultrafast single-qubit operations in semiconductor quantum dots. *Applied Physics Letters*, 88(23):233108, 2006.

[145] Y. C. Zhang, A. Pancholi, and V. G. Stoleru. Size-dependent radiative lifetime in vertically stacked (In,Ga)As quantum dot structures. *Applied Physics Letters*, 90(18):183104, 2007.

[146] A. Greilich, A. Shabaev, D. R. Yakovlev, Al. L. Efros, I. A. Yugova, D. Reuter, A. D. Wieck, and M. Bayer. Nuclei-induced frequency focusing of electron spin coherence. *Science*, 317(5846):1896–1899, 2007.

APPENDIX A

COPYRIGHT PERMISSION

AMERICAN INSTITUTE OF PHYSICS LICENSE TERMS AND CONDITIONS
All payments must be made in full to CCC. For payment instructions, please see information listed at the bottom of this form.

License Number	3143781111335
Order Date	May 07, 2013
Publisher	American Institute of Physics
Publication	Journal of Applied Physics
Article Title	Optically engineered ultrafast pulses for controlled rotations of exciton qubits in semiconductor quantum dots
Author	Angela Gamouras, Reuble Mathew, Kimberley C. Hall
Online Publication Date	Jul 6, 2012
Volume number	112
Issue number	1
Type of Use	Thesis/Dissertation
Requestor type	Author (original article)
Format	Print and electronic
Portion	Excerpt ($\geq$ 800 words)
Will you be translating?	No
Title of your thesis/dissertation	Control of Charge Dynamics in Semiconductor Quantum Dots Using Ultrafast Optical Pulses

Expected completion date	Aug 2013
Estimated size (number of pages)	130
Total	0.00 USD

Terms and Conditions

American Institute of Physics – Terms and Conditions: Permissions Uses

American Institute of Physics (”AIP”) hereby grants to you the non-exclusive right and license to use and/or distribute the Material according to the use specified in your order, on a one-time basis, for the specified term, with a maximum distribution equal to the number that you have ordered. Any links or other content accompanying the Material are not the subject of this license.

1. You agree to include the following copyright and permission notice with the reproduction of the Material:”Reprinted with permission from [FULL CITATION]. Copyright [PUBLICATION YEAR], American Institute of Physics.” For an article, the copyright and permission notice must be printed on the first page of the article or book chapter. For photographs, covers, or tables, the copyright and permission notice may appear with the Material, in a footnote, or in the reference list.

2. If you have licensed reuse of a figure, photograph, cover, or table, it is your responsibility to ensure that the material is original to AIP and does not contain the copyright of another entity, and that the copyright notice of the figure, photograph, cover, or table does not indicate that it was reprinted by AIP, with permission, from another source. Under no circumstances does AIP, purport or intend to grant permission to reuse material to which it does not hold copyright.

3. You may not alter or modify the Material in any manner. You may translate the Material into another language only if you have licensed translation rights. You may not use the Material for promotional purposes. AIP reserves all rights not specifically granted herein.

4. The foregoing license shall not take effect unless and until AIP or its agent, Copyright Clearance Center, receives the Payment in accordance with Copyright Clearance Center Billing and Payment Terms and Conditions, which are incorporated herein by reference.

5. AIP or the Copyright Clearance Center may, within two business days of granting this license, revoke the license for any reason whatsoever, with a full refund payable to you. Should you violate the terms of this license at any time, AIP, American Institute of Physics, or Copyright Clearance Center may revoke the license with no refund to you. Notice of such revocation will be made using the contact information provided by you. Failure to receive such notice will not nullify the revocation.

6. AIP makes no representations or warranties with respect to the Material. You agree to indemnify and hold harmless AIP, American Institute of Physics, and their officers, directors, employees or agents from and against any and all claims arising out of your use of the Material other than as specifically authorized herein.

7. The permission granted herein is personal to you and is not transferable or assignable without the prior written permission of AIP. This license may not be amended except in a writing signed by the party to be charged.

8. If purchase orders, acknowledgments or check endorsements are issued on any forms containing terms and conditions which are inconsistent with these provisions, such inconsistent terms and conditions shall be of no force and effect. This document, including the CCC Billing and Payment Terms and Conditions, shall be the entire agreement between the parties relating to the subject matter hereof.

This Agreement shall be governed by and construed in accordance with the laws of the State of New York. Both parties hereby submit to the jurisdiction of the courts of New York County for purposes of resolving any disputes that may arise hereunder.

If you would like to pay for this license now, please remit this license along with your payment made payable to "COPYRIGHT CLEARANCE CENTER" otherwise you will be invoiced within 48 hours of the license date. Payment should be in the form of a check or money order referencing your account number and this invoice number 501016268. Once you receive your invoice for this order, you may pay your invoice by credit card. Please follow instructions provided at that time.

APPENDIX B

MULTIMEDIA DESCRIPTIONS

Included with this thesis are two video .mov files. These movie files were included in the publication Nano Letters, DOI: 10.1021/nl4018176, Angela Gamouras, Reuble Mathew, Sabine Freisem, Dennis G. Deppe and Kimberley C. Hall, "Simultaneous Deterministic Control of Two Solid State Qubits Using Engineered Optical Pulses". Copyright 2013 American Chemical Society. The captions for each supplementary movie are included below.

B.1 Movie S1

Duration: 15 s. First reference on page 87.
Dynamics of the pesudo spin vector on the Bloch sphere for the exciton states in QD1 (red circles) and QD2 (black squares) under control by a shaped pulse. The orientation of the Bloch sphere is identical to that in Fig. 3(a) in the main text. The time dependence of the electric field is shown in Fig. S4(b).

B.2 Movie S2

Duration: 15 s. First reference on page 87.
Dynamics of the pesudo spin vector on the Bloch sphere for the exciton states in QD1 (red circles) and QD2 (black squares) under control by an unshaped pulse. The orientation of the Bloch sphere is identical to that in Fig. 3(a) in the main text. The time dependence of the electric field is shown in Fig. S4(e).